Probably one photon

Der Naturwissenschaftlichen Fakultät
der Universität Paderborn
zur
Erlangung des Doktorgrades Dr. rer. nat.
vorgelegt von

Marcello Massaro

2020

SUMMARY

The most fundamental resource in quantum optics is undeniably the photon. Over the years, the growth of the field has pushed the demand for better, more performant, and tailored single photon sources that cater to the diverse needs of quantum optics experiments.

This work is centered on spontaneous parametric downconversion (SPDC) sources. To stress their maturity as practical devices, we use a SPDC source to verify that optical metasurfaces can be successfully employed in a hybrid quantum photonic system with good performance. We then devise and experimentally apply a technique that improves the generation rate of spectrally-filtered sources, without compromising state's fidelity.

We then explore the concept of source multiplexing (MUX) to overcome the probabilistic nature of SPDC sources. We detail the interplay between the type of chosen MUX scheme and the role of losses, stressing how important high quality components are. In order to implement such MUX schemes, we design and test electro-optic modulators (EOM) to be used in a time MUX setup. Although the design did not perform sufficiently well, it provides valuable data to improve our EOMs design and fabrication in general. Finally, we develop a new MUX scheme based on engineered time-frequency correlations in SPDC sources and fast EOMs, and report on the characterization of its most important building blocks. This scheme, being a compromise between speed and compactness, represents a step forward towards the implementation of a more general purpose MUX source.

ZUSAMMENFASSUNG

Die grundlegendste Ressource in der Quantenoptik ist unbestreitbar das Photon. Im Laufe der Jahre hat das Wachstum auf diesem Gebiet die Nachfrage nach besseren, leistungsfähigeren und maßgeschneiderten Einzelphotonenquellen erhöht, die den unterschiedlichen Anforderungen quantenoptischer Experimente gerecht werden.

Diese Arbeit konzentriert sich auf Quellen mit spontaner Parametrischer Fluoreszenz (SPDC). Um ihre Reife als praktische Geräte zu betonen, wird eine SPDC-Quelle verwendet, um zu verifizieren, dass optische Metaflächen in einem hybriden quantenphotonischen System mit guter Leistung erfolgreich eingesetzt werden können. Weiterhin wird eine experimentelle Technik entwickelt und angewendet, die die Erzeugungsrate von spektral gefilterten Quellen verbessert, ohne die Zustandstreue zu beeinträchtigen.

Das Konzept des *Source-Multiplexing* (MUX) wird untersucht, um die probabilistische Natur der SPDC-Quellen zu überwinden. Im Detail wird auf das Zusammenspiel zwischen der Art des gewählten MUX-Schemas und der Rolle von Verlusten eingegangen und betont, wie wichtig qualitativ hochwertige Komponenten sind. Um solche MUX-Schemata zu implementieren, werden elektro-optische Modulatoren (EOM) entworfen und getestet, die in einem Zeit-MUX-Aufbau verwendet werden. Obwohl das Design nicht ausreichend gut funktioniert hat, liefert es wertvolle Daten zur Verbesserung des Designs und der Herstellung unserer EOMs im Allgemeinen. Schließlich wurde ein neues MUX-Schema entwickelt, das auf konstruierten Zeit-Frequenz-Korrelationen und in SPDC-Quellen und schnellen EOMs basiert, und über die Charakterisierung seiner wichtigsten Bauelemente berichtet. Dieses Schema, das einen Kompromiss zwischen Geschwindigkeit und Kompaktheit darstellt, stellt einen Schritt vorwärts auf dem Weg zur Implementierung einer MUX-Quelle für allgemeinere Zwecke dar.

Introduction

You talk to someone and they are trying to explain to you some idea they have. Something along the lines of «Suppose we have a single photon…» or «Imagine that we have a photon here…». The idea is intriguing, challenging, and you want to implement it, see what comes out of it (or write an entire grant's proposal based on it, depending on the idea) and you start jotting down a sketch of the possible experiment. And there lies, the first box of your schematic: "photon source". That's usually the case: there is this black box that creates a photon for you when you want it. Not only that, it creates a photon with well-defined properties that match the requirements of your experiment.

Producing photons is not hard, really. Flip a switch in a room to turn on the lights and you'll be inundated with millions of them every second. Most of the times though, especially in quantum optics, having *some* photons is not enough. You want them to be *just* in the right state. This is where problems usually arise: we always want to have a well defined state, a "useful" state, which we can manipulate at will and whose properties can be modified with analytical precision.

The key here is the fact that we want to manipulate *one* photon. Not two, not some, but rather just one. This is where things get complicated or, depending on whom you ask, interesting. A photon has multiple characteristics that one may be interested in and it turns out that having complete control on all of them is challenging.

Interest into single-photon sources has seen a steady increase in the last decade. The reason for this is that photons are the best quantum information carriers one can think of: they are virtually unaffected by external noise, they do not interact with each other, they travel very quickly (which is an euphemism) and can be manipulated with ease [1]. Not only as information carriers, but also as computing platform [2, 3], single-photons have achieved a leading role in most areas of quantum information technology.

As we said though, the requirements of these sources become more and more stringent. Many platforms are being explored in order to deterministically produce indistinguishable photons, from quantum dots [4–7], to color centers in diamonds [8–10], to the focus of this work: spontaneous parametric downconversion (SPDC) sources in non-linear crystals [11–16].

We start in chapter 1 by studying the underlying mechanism by which an SPDC source works. This requires us to have both a classical and quantum picture of this process. We will explain how the material's polarization can give rise to a plethora of effects and how to tailor these to our needs. Next we will "go quantum" and introduce a necessary formalism (Schmidt's decomposition and the broadband creation operators) to abandon a continuous description of these processes and instead use a discrete one, which is much easier to handle and which will give us important insights that we will use later on.

Having an understanding of *what* SPDC is, we will put it into context in a real world experiment, underlying the fact that what we have just described is a mature tool in the quantum

toolbox that scientists need for their experiments. This will be described in chapter 2, in which we show how an SPDC source can be integrated with other technologies, in this case optical metasurfaces.

Adequate for some tasks, these sources are not without problems [17], although some of these can be mitigated as we underline in chapter 3. Here, we will show how we can filter a correlated source, to increase its purity, while at the same time not sacrificing single-photon generation rate as much.

This is of course a stop-gap measure, and in chapter 4 we will introduce the concept of source multiplexing [18]. This technique can indeed solve the biggest problem of SPDC based sources, which is their probabilistic nature [19]. In this chapter we first explore this problem, and later on analyze various multiplexing schemes, showing that these can come arbitrarily close to a "true" deterministic single-photon source.

In almost all these schemes, one of the main components is an electro-optic modulator. These devices allow real-time reconfiguration of an optical setup and are paramount in multiplexing schemes. In chapter 5 we will briefly touch on two important types of modulators and describe their working principle: the directional coupler and the integrated polarization converter.

Finally, in chapter 6, we will introduce a new type of multiplexing scheme, which makes use of both of the components detailed in the previous chapters: an SPDC source and an electro-optic modulator. We will show the concept of the scheme and the characterization of its most important building blocks, which all work as intended, leaving only a fast mode selective detection scheme as a last piece to fully implement the scheme.

Contents

Part I.

Single sources of single photons

1. SPLITTING PHOTONS: OPTICAL NONLINEARITIES IN LITHIUM NIOBATE AS SINGLE-PHOTON SOURCES

Many different options [4, 6, 20, 21] are available when you want to produce single photons, and the quality of such types of sources improves every year. One such option is the use the optical nonlinearities present in some crystals. We will focus mainly on such type of sources and how they can be used for single-photons applications. One of the most used nonlinear crystals is lithium niobate ($LiNbO_3$), which has a fairly high (in the order of $10\,\mathrm{pm\,V^{-1}}$) nonlinear susceptibility, high transparency in a range of optical wavelengths commonly used in the telecom industry, and other interesting and useful effects, like the electro-optic effect [22].

1.1. NONLINEAR OPTICAL MATERIALS AND PROCESSES

Light in a vacuum is not very interesting. Photons do not interact with each other (one of the main reasons why light is used as information carrier) and thus they just wander aimlessly until they come in contact with *matter*.

1.1.1. NONLINEAR TERMS OF THE POLARIZATION DENSITY

If you go back to the day in which your physics professor introduced this interaction to your class you may remember the following (or at least similar) reasoning. In a dielectric medium (as opposed to conductors), electrons are bound to their atoms and an electromagnetic field traversing this medium will displace these electrons from their equilibrium "position"[1]. At this point, the electrons will start oscillating and by this point in your studies you were told that a moving charge is a *source* for an EM field.

This charge displacement, where dipoles are formed in some volume of interest, is called *polarization density*. Just as a side note, the way polarization density is usually defined is not unique [23]: since the "volume of interest" is arbitrary, two different quantities for the polarization density can be constructed and both would be correct. The thing that is important here is that the physical quantities that we measure everyday do not depend on the *value* of the polarization density, but rather on its *changes* [23].

Assume now that the medium we are studying is homogeneous and isotropic[2] and that it does not have an inherent polarization (like water). This polarization density then, «to a first

[1] The quotation marks are for the savvy reader who knows that «an electron has a certain *probability* of occupying a given volume».

[2] Which means that we don't care neither *where* we are in the medium nor which *direction* we are considering for any effect we want to study.

approximation» [3], is a linear function of the external electric field, i.e.:

$$\vec{P} = \varepsilon_o \chi \vec{E} \tag{1.1}$$

where ε_0 is the permittivity of vacuum and χ is the *electric susceptibility*. The latter is in general a tensor, but we will simplify our lives with some assumptions (isotropy of the medium, in this case) and will treat it as a scalar, at which point (1.1) can be studied in its scalar form, by considering only one of its components.

Considering the relationship between an external field and the polarization density as a linear one, is an intuitive choice: in a simple Lorentz model with a weak driving force (i.e. field), Hooke's law applies and the displacement of the charges is linear with the force applied [24]. But that means that we are disregarding higher order effects.

Every physics student is familiar with the phrase «these are higher order effects which we will disregard», or something along those lines. At that moment the focus of the lecture is clearly on more basic or fundamental concepts whose understanding does not benefit from the inclusion of such details. This makes perfect sense when you are introducing a concept to a new audience. This work, however, is *centered* on these details, so we will take from where we left off during our introductory classes and expand a bit.

The linearity in (1.1) is justified because we are assuming a weak field. However, if we are using a high-intensity field (say, a laser), this is not necessarily the case anymore and we must take into account higher order effects. We can then rewrite the polarization density as a generic function of the field. Now we can analyze this function by slowly incrementing the field strength, going from a weaker field to stronger one, but still not really comparable to the internal crystalline/atomic field strength. If you were smelling Taylor expansion since the last few sentences, you were right. We carry on this expansion then

$$P(E) = \sum_{n=1}^{\infty} \frac{1}{n!} a_n E^n \approx a_1 E + \frac{1}{2} a_2 E^2, \tag{1.2}$$

where we consider this equation on a component-by-component basis and we stop at the first nonlinear term. Notice that $a_0 = 0$ because for a material without inherent polarization, as is the one we are considering right now, $P = 0 \Leftrightarrow E = 0$, thus we start the summation from 1.

The other coefficients are quantities related to the medium itself. It's easy to identify $a_1 = \varepsilon_0 \chi$, which is our linear susceptibility. The second coefficient, a_2, can be written as $2\varepsilon_0 \chi^{(2)}$, where $\chi^{(2)}$ is the *second-order nonlinear susceptibility*[4]. If in general we redefine

$$a_n = n! \varepsilon_0 \chi^{(n)} \tag{1.3}$$

we have the much clearer equation

$$P(E) = \varepsilon_0 \left(\chi E + \chi^{(2)} E^2 + \cdots \right) \tag{1.4}$$

[3] And it's a good one most of the times.

[4] The notation for this Taylor expansion depends on taste, depending on how much the author likes to foreshadow concepts that can be introduced later on.

We will focus only on the *nonlinear* part of (1.4), so it's useful to define

$$P_{\text{nl}} = \varepsilon_0 \chi^{(2)} E^2 \tag{1.5}$$

where we have dropped the contributions from terms higher than the second order.

Even if we are interested in second-order nonlinear effects, can we safely disregard higher-order terms in (1.5)? That depends on the material being used. As an example, $LiNbO_3$ presents the following second and third order susceptibilities [25]:

$$\chi^{(2)} \approx 3 \times 10^{-11}\,\text{m V}^{-1}$$
$$\chi^{(3)} \approx 2 \times 10^{-21}\,\text{m}^2\,\text{V}^{-2}$$

We can estimate what typical field strengths we will encounter in the lab. Assume that on average the power levels used in our experiments don't really exceed 10×10^{-3} W. We can relate power to electric field strength if we recall that the latter is tied to the intensity, i.e. power per unit area. A typical spot size is in the order of 2 mm, but that can be shrunk down to a few microns easily. Let's assume that we can shrink down the spot size of a laser beam to a diameter of 7 µm. The *intensity* of an electric field is the power per unit area, i.e.

$$I = \frac{P}{\pi r^2} = \frac{10 \times 10^{-3}\,\text{W}}{\pi 1.225 \times 10^{-11}\,\text{m}^2} \approx 2.6 \times 10^8\,\text{W m}^{-2} \tag{1.6}$$

The intensity of a propagating monochromatic electromagnetic wave is tied to its field strength [24]

$$I = \frac{cn\varepsilon_o}{2} |E|^2 \Rightarrow E = \sqrt{\frac{2I}{cn\varepsilon_0}} \tag{1.7}$$

where c is the speed of light in vacuum, n the refractive index of the medium and ε_0 the permittivity of vacuum. Considering that in $LiNbO_3$ $n \approx 2$ we have that $E \approx 3 \times 10^5\,\text{V m}^{-1}$. The contribution from such a field in the third term of (1.4) is 6 orders of magnitude weaker than that in the second term. Disregarding the orders higher than the second is thus a very good approximation.

If we keep the approximation that the medium where our field propagates is non-magnetic, homogeneous, non-dispersive and isotropic, then the various susceptibilities are still scalars. This is usually not the case, especially in this work, where we will take advantage of materials which are definitely anisotropic (so-called *birefringent* materials). In general, the susceptibility of order n is a function of time and space (for dispersive and inhomogeneous media) and is a tensor of rank $n+1$.

If we consider more than just the linear term in (1.4), it can be shown from Maxwell's equations and boring vector identities, that the standard equation of nonlinear optics [26]

$$\nabla^2 \vec{E} + \frac{n^2}{c^2} \frac{\partial^2 \vec{E}}{\partial t^2} = -\frac{1}{\varepsilon_0 c^2} \frac{\partial^2 \vec{P}_{\text{NL}}}{\partial t^2} \tag{1.8}$$

indicates that the nonlinear part of the polarization density is a source for an electromagnetic field.

Let's give some substance to this last sentence, by considering linearly polarized plane wave fields traveling along some direction z with the form $\mathscr{E}(\omega,t) = \mathrm{Re}\left\{E(\omega)e^{-i\omega t}\right\} = \frac{1}{2}\left(E(\omega)e^{-i\omega t} + \text{c.c.}\right)$, where "c.c." stands for complex conjugate (we have absorbed the space-dependent term in the field's phase in the complex amplitude $E(\omega)$), and suppose that a superposition of two such fields, with frequencies ω_1, ω_2 propagates inside a medium with a non-zero $\chi^{(2)}$. We have then, substituting in (1.5),

$$P_{\mathrm{NL}}(E) = \frac{\varepsilon_0 \chi^{(2)}}{4}\left(E(\omega_1)e^{-i\omega_1 t} + E(\omega_2)e^{-i\omega_2 t} + \text{c.c.}\right)^2 \tag{1.9}$$

which, when expanded, shows interesting frequency dependencies:

$$\begin{aligned} P_{\mathrm{NL}}(E) = \frac{\varepsilon_0 \chi^{(2)}}{4} \big(&2E(\omega_1)E^*(\omega_1) + 2E(\omega_2)E^*(\omega_2) + \\ &+ 2E(\omega_1)E(\omega_2)e^{-i(\omega_1+\omega_2)t} + \\ &+ 2E(\omega_1)E(\omega_2)e^{-i(\omega_1-\omega_2)t} + \\ &+ E^2(\omega_1)e^{-i2\omega_1 t} + E^2(\omega_2)e^{-i2\omega_2 t}\big) \end{aligned} \tag{1.10}$$

Equation (1.10) has many frequency components, each of which, according to (1.8), is a source for an EM field at different frequencies. We can see that up to three different frequencies can be coupled by the nonlinearity of the material, thus the processes here highlighted are usually called *three-wave mixing* in the literature. In the most uninspired way, each of these new fields have an associated name in the literature.

Optical rectification (OR) This is the first two terms of (1.10) and describes a *static* field. This means that even though we are using an oscillating field to drive the dipoles in the material, one of the net effects is the presence of a static electric field, no matter the frequencies of the driving fields. This can be used with pulsed light to generate THz radiation [27].

Sum-frequency generation (SFG) The second term presents an overall frequency which is the *sum* of the driving fields' frequencies. This proves to be a great tool in optics and photonics, making it possible to access optical frequencies which cannot be produce by conventional lasers. A particular case of SFG, when $\omega_1 = \omega_2$, is called *second harmonic generation* (or SHG) and it's the most common way to produce green (532 nm) light from a Nd:YAG 1064 nm laser.

Difference-frequency generation (DFG) Analogously to SFG, the third term produces a wave with a frequency which is the *difference* of the input fields. This also has multiple uses is photonics, in particular in the development of optical parametric amplifiers and oscillators (OPA and OPO, respectively).

Before going further, let us generalize our definition of nonlinear polarization density. Depending on the material, a field with a well defined polarization can stimulate the generation of

a field in a *different* polarization. This means that in general, polarization density and incoming fields are related by the following equation

$$P_i(\omega_n+\omega_m)=\frac{\varepsilon_0}{4}\sum_{j,k}\sum_{(mn)}\chi^{(2)}_{ijk}(\omega_n+\omega_m;\omega_n,\omega_m)E_j(\omega_n,t)E_k(\omega_m,t) \tag{1.11}$$

which is one cartesian component of the polarization density field at frequency $\omega_n+\omega_m$. The sum over (nm) is carried over all possible permutations of the mentioned two indices, extended to both positive and negative values. This paints a pretty grim picture for those who would like to brave the calculation of the complete $\chi^{(2)}$. Each Latin index can independently assume three distinct values, and for each distinct triplet of indices, there are twelve possible permutations of the frequency components. This leads us to 324 *complex* numbers if we want to completely describe the interaction [26]. However, all the processes that are treated in this work will involve optical frequencies which are significantly smaller than the resonant frequencies of the material in which they take place. In this case, the $\chi^{(2)}_{ijk}$ are essentially independent of frequency, and they obey certain symmetries which greatly reduce the number of independent components that we need to consider. This condition is known as *Kleinman's symmetry* and it amounts to being able to freely permute the Latin indices of the nonlinear tensor without changing its value.

Handling this tensor is still rather cumbersome. It's customary at this point to introduce[5] another tensor [26]

$$d_{ijk}=\frac{\chi^{(2)}_{ijk}}{2} \tag{1.12}$$

which is symmetric in its i and j indices in the case of Kleinman's symmetry. Because of this, this tensor can be rewritten as a 3×6 matrix, d_{il}, by associating the indices j,k to l as laid out in Table 1.1.

j,k:	11	22	33	23,32	31,13	12,21
l:	1	2	3	4	5	6

Table 1.1.: d-tensor index in contracted notation.

Thanks again to Kleinman's symmetry, there are only ten independent components int the d-tensor out of eighteen, which is just a boring puzzle of mixing and matching all the indices in (1.12) according to Table 1.1. As an example, notice that $d_{12}=d_{122}=d_{212}=d_{26}$, and a similar reasoning can be applied to all elements of the d-tensor.

This lets us immediately link each of the components of the polarization density to all fields

[5] In an absolutely arbitrary fashion.

components that influence it, as laid out in the following matrix expression:

$$\begin{pmatrix} P_x(\omega_3) \\ P_y(\omega_3) \\ P_z(\omega_3) \end{pmatrix} = \varepsilon_0 \begin{pmatrix} d_{11} & d_{12} & d_{13} & d_{14} & d_{15} & d_{16} \\ d_{16} & d_{22} & d_{23} & d_{24} & d_{14} & d_{12} \\ d_{15} & d_{24} & d_{33} & d_{23} & d_{13} & d_{14} \end{pmatrix} \cdot \begin{pmatrix} E_x(\omega_1)E_x(\omega_2) \\ E_y(\omega_1)E_y(\omega_2) \\ E_z(\omega_1)E_z(\omega_2) \\ E_y(\omega_1)E_z(\omega_2)+E_z(\omega_1)E_y(\omega_2) \\ E_x(\omega_1)E_z(\omega_2)+E_z(\omega_1)E_y(\omega_2) \\ E_x(\omega_1)E_y(\omega_2)+E_y(\omega_1)E_x(\omega_2) \end{pmatrix} \tag{1.13}$$

Scientists love to classify phenomena, and nonlinear optical effects are not untouched by this. We have classified already these processes by the way the involved wavelengths are combined (e.g. SHG vs. DFG), but we can also classify them in terms of what the *polarization* of each field is:

Type 0 All fields involved have the same polarization.

Type I Both input (e.g. SHG) fields or both output (e.g. DFG) fields have the same polarization.

Type II The input (e.g. SHG) fields or output (e.g. DFG) fields have the orthogonal polarization.

To simplify things, each crystalline structure has some additional limits on which of the d_{ij} can be non-zero, so usually this tensor further simplifies. Since we are going to work with $LiNbO_3$ and potassium titanyl-phosphate (KTP) during the course of our discussion, we will show the d tensor structure for these two crystals as an example [26].

$$\mathrm{LiNbO_3} = \begin{pmatrix} 0 & 0 & 0 & 0 & d_{15} & d_{16} \\ d_{16} & d_{22} & 0 & d_{24} & 0 & 0 \\ d_{15} & d_{24} & d_{33} & 0 & 0 & 0 \end{pmatrix} \quad \mathrm{KTP} = \begin{pmatrix} 0 & 0 & 0 & 0 & d_{15} & 0 \\ 0 & 0 & 0 & d_{24} & 0 & 0 \\ d_{15} & d_{24} & d_{33} & 0 & 0 & 0 \end{pmatrix} \tag{1.14}$$

This also implicates that a given material only allows a subset of all possible processes listed earlier, because some polarization combinations are not possible.

1.1.2. Phase-matching

At this point in our discussion, it looks like nonlinear optics is a cornucopia of possibilities, enabling us to exploit such materials to produce whatever frequency combination our heart desires. We made the mistake of getting too comfortable in our assumptions guiding us here and it's now time to revisit them, before we come to woefully wrong conclusions.

First, the material we are considering is *dispersionless*. Well, that cannot *physically* be true, since no process is truly instantaneous, so we have dispersion, which basically means that the refractive index at time t depends on the value of the refractive index at time $t - \mathrm{d}t$. A dispersive material has a frequency-dependent refractive index (i.e. linear susceptibility), which means that different frequencies will travel at different speeds and will accumulate different spatial phases along the same path.

Second, we are also considering materials which are *isotropic*. While isotropy is not uncommon in materials used in optics (e.g. glasses), this work will focus on material which exhibit a particular kind of anisotropy, birefringence, as previously mentioned.

Recall that we have "hidden" the spatial dependency of the fields into their complex amplitudes $E(\omega)$. If we take this into account, we might notice something which is crucial in understanding these processes. The complete field expression is then

$$\vec{E}(\vec{r},\omega,t) = \vec{A}(\vec{r},\omega,t)e^{-i\left(\omega t - \vec{k}(\omega,\vec{r})\cdot\vec{r}\right)} \tag{1.15}$$

where $\vec{A}$ is a complex vector describing the polarization state of the field, $\vec{k}(\vec{r},\omega,)$ is the *wave vector*[6] which has the form

$$\vec{k}(\vec{r},\omega) = \frac{\vec{n}(\vec{r},\omega)\omega}{c} \tag{1.16}$$

which, for simplicity, we will often shorten to simply $\vec{k}$ and finally $\vec{n}$ is the refractive index vector.

This means two things: one, each dipole will be driven with a different initial phase which is *space dependent*; two, while the driving fields will propagate with a wave vector $\vec{k}(\vec{r},\omega)$, the generated fields will propagate with a different one, which depends on the specific process we are considering (e.g. for the case of SHG, $\vec{k}(\vec{r},2\omega)$). In order to measure any of the fields described by (1.10), the wave vectors must be *matched* in order for the fields radiated by the various dipoles to build up constructively along the interaction volume. This is called, with a rather daring imagination, *phase-matching*. It is not a simple topic by any metric and it is not the focus of this work, but it is nonetheless important to understand the underlying ideas and how they fit in the following chapters.

First, let's simplify our work. We are interested in a semi-quantitative approach here, so we will make some assumptions that do not hold in general but give nonetheless a fairly accurate description of the basic ideas of nonlinear processes. To do this, we will assume that we are treating linearly polarized monochromatic plane fields. We will choose a frame of reference in which the z axis is aligned with the propagation direction of the field and one of the crystallographic axes of the crystal and, for example, the y axis is aligned with the polarization direction, also along a specific crystallographic axis. This will reduce the general expression for our fields (1.15) to

$$E(z,\omega,t) = A(z,\omega,t)e^{-i(\omega t - kz)}. \tag{1.17}$$

We will also assume that the change in amplitude over a distance of the order of an optical wavelength is much smaller than unity (an approximation called *slow-varying amplitude* or SVA approximation). This greatly reduces our math-gymnastics needs, and we can directly plug (1.17) into (1.8) and (1.11) to obtain the so-called *coupled-wave equations*, whose form depends on the type of process we are interested in. This work is all about generating single photons, so we will shift our focus on the process of DFG. The reason for this will be explained soon.

[6] Sometimes also called *propagation constant* and indicated with β.

The coupled-wave equations for the DFG process read [26]

$$\begin{cases} \dfrac{\mathrm{d}A_1(z)}{\mathrm{d}z} = \dfrac{8\pi i\,\omega_1 d_{\mathrm{eff}} A_3}{n(\omega_1)c} A_2^*(z) e^{i\Delta k z} \\ \dfrac{\mathrm{d}A_2(z)}{\mathrm{d}z} = \dfrac{8\pi i\,\omega_2 d_{\mathrm{eff}} A_3}{n(\omega_2)c} A_1^*(z) e^{i\Delta k z} \end{cases} \tag{1.18}$$

where d_{eff} is the effective value of the d tensor for a fixed geometry and crystal class [28] and $n(\omega)$ is the refractive index of the material relative to the polarization direction of the field currently considered. Here, a strong field at ω_3 interacts with a second field at ω_1 to generate the DFG field at $\omega_2 = \omega_3 - \omega_1$. An important factor in these equations is the *wavevector mismatch*

$$\Delta k = k_3 - k_1 - k_2. \tag{1.19}$$

As we previously mentioned, the three interacting field must be phase matched in order to interfere constructively during propagation. This is achieved only when $\Delta k = 0$.

This work is about neither the intricacies of the math behind the analytical solutions to such type of equations (which can be readily found in the literature [26, 29, 30]) nor the study of all possible cases that these equations might cover. We want to instead have an idea about the general physics behind these processes, for which we need not to care about the mathematical details, rather only the final result and how this relates to experimental results. To get a general idea of what happens, we assume that the seed and pump fields do not change significantly during the propagation in the crystal, and we will treat them essentially as constants. We will also assume that there is no DFG field at the beginning of the crystal, so that $A_2(0) = 0$. We can then integrate the second equation of (1.18) from 0 to L, the latter being the propagation length, and calculating the intensity of the field (which is the quantity actually measured)

$$I_2(L) = L^2 |\gamma|^2 |A_1^*(0)|^2 \operatorname{sinc}^2\left(\frac{\Delta k}{2} L\right) \tag{1.20}$$

which is plotted in Figure 1.1 and where

$$\operatorname{sinc}(x) \coloneqq \frac{\sin(x)}{x} \tag{1.21}$$

is the *sinus cardinalis*. To simplify the notation, we have hidden all multiplicative factors in γ.

By looking at the intensity profile, the reason why Δk is an important parameter should be clear. The intensity has a maximum for $\Delta k = 0$, which is known as *phase-matching condition*. This quantity depends on the material through which the fields propagate, the frequencies of said fields and their propagation and polarization directions. It's paramount then that we choose our material with care so that the phase-matching condition is satisfied, while also having good overall optical qualities, like a high nonlinear susceptibility and transparency in the frequency window of interest. One of the most common materials used for such tasks is lithium niobate, which has great transparency in the most common telecom windows, high nonlinearity and also good electro-optical properties (so that high-speed electro-optic devices can be easily manufactured).

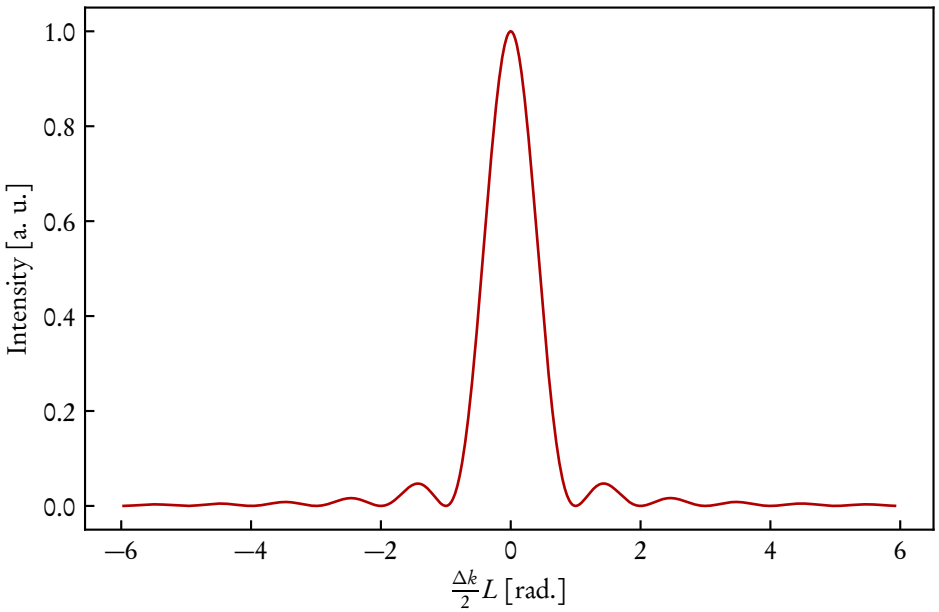

Figure 1.1.: The intensity (or phase-matching) profile of the generated DFG field.

Achieving phase-matching conditions is not an easy task and most of the time is plainly not possible in most materials. The simplest example is collinear Type-0 SHG in a material with normal dispersion[7]. Assume then that our driving field at ω is traveling along the z direction, just as the produced SHG field. Then the equation for the phase mismatch can be regarded as a scalar one and by virtue of (1.16) it simplifies to

$$n(2\omega) = n(\omega) \tag{1.22}$$

which has no solution for a material with normal dispersion. A solution would be to use birefringent materials (like $LiNbO_3$), where the refractive index is a function of the polarization state. This is aptly called *birefringent phase-matching*, but of course gives us very little freedom in the number of possible processes.

In the case of interest of this work (i.e. nonlinear processes in $LiNbO_3$), if we assume a DFG process where the seeding field and the difference field are orthogonally polarized and centered around 1550 nm[8], calculating Δk yields nothing close to 0 (Figure 1.2).

These results underline the fact that we need to compensate the additional relative phase that the three fields accumulate per unit length, somehow. Since (1.19) depends mostly on wavelengths involved and the refractive index of the material, we can do one of two things:

[7] Normal dispersion means that the derivative of the refractive index with respect to the wavelength is negative.

[8] The choice of wavelength range is not random. One of the most common transmission windows in the telecom industry is the so-called "C" band (1530 nm to 1565 nm). Here, optical fibers have extremely low losses of about 0.3 dB km^{-1}.

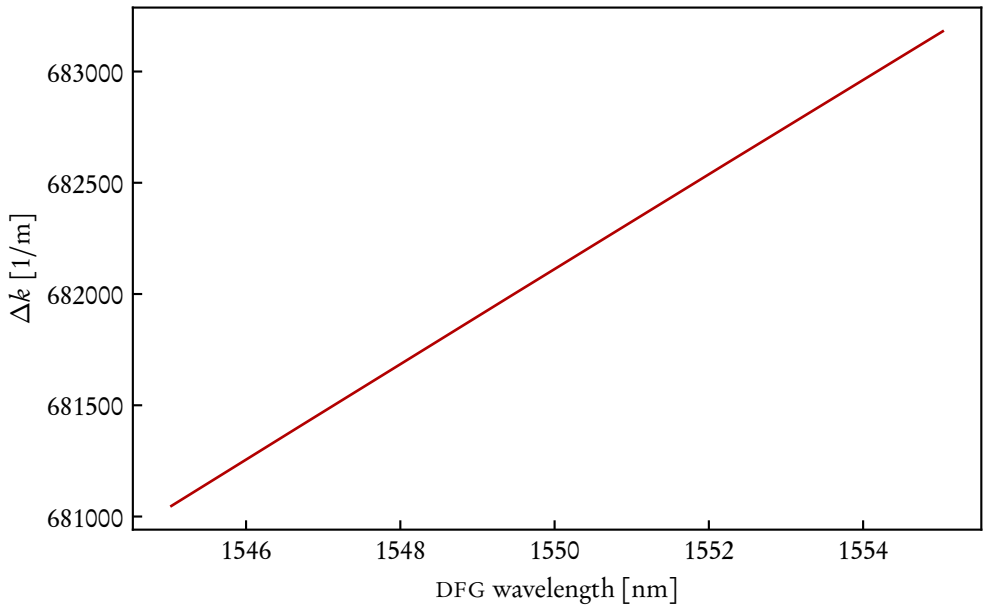

Figure 1.2.: Phase mismatch for a Type-II DFG process in lithium niobate, with a fixed pump at 775 nm.

change the target wavelengths of the process in order to find a tuple that satisfies (1.19) or we choose a different crystal that has the necessary refractive index to allow our process. As we have seen, depending on the process we are interested in, this might just not be possible at all, depending on the process one is interested in.

The solution is to actually *modify* the material we are so interested in with a technique called *periodic poling*. It boils down to periodically changing the orientation of the d tensor in a way that modifies the wave-vector mismatch. Since we are talking about a period change, you can write the tensor d as a Fourier series

$$d(x,y,z) = \sum_{n}^{\infty} i \frac{2d}{(2n+1)\pi} e^{i\,2\pi(2n+1)z/\Lambda} \tag{1.23}$$

where Λ is the period of this inversion. This would modify (1.18) so that integrating along z now introduces an additional factor in the wave-vector mismatch, which is precisely

$$\Delta k \to \Delta k \pm \frac{2\pi}{\Lambda} \tag{1.24}$$

if we choose the first order in the Fourier expansion. This technique opens up a wealth of possibilities, because we can customize Λ to our needs.

We now know roughly how to tailor a given nonlinear process, so it's time to make some photons. Before doing that, we want to address the elephant in the room.

The discussion that we have had up until this point has completely disregarded the quantum nature of light. Everything has been treated as a classical field, because for a general overview of these processes, that's what suffices. If we now want to deal with *single* photons, clearly we need to be more precise, which is exactly what we are going to address in the next sections.

1.2. Creating photon pairs

Consider (1.20). What happens if there is *no* input field at ω_1? There should not be any field at ω_2, right? Wrong.

Remember that the vacuum in quantum mechanics is never really "empty". Vacuum fluctuations could interact with the incoming strong pumping field and stimulate the process of DFG at any possible frequencies that satisfy energy conservation. However, this is not the only relationship that a process needs to obey, as we have seen from our previous discussion. We also need to respect the phase-matching condition, i.e. (1.19) must be (close to) 0 for constructive interference to take place. If you want to see this from a particle point of view, it means that we need to also satisfy momentum conservation. The combination of wavelengths for which both conditions hold is the only one which will coherently build up and which can be detected at the output of the crystal. This is typically called *spontaneous parametric down-conversion* (SPDC), and it results in a process in which a single pump photon decays into a pair of lower energy photons, usually called *signal* and *idler* photons.

1.2.1. Renaming DFG to SPDC

Before trying to justify the new name we have given to our DFG process, we need to re-develop our calculations and turn them "quantum". This means two things. First, in order to describe the evolution of a quantum system, we need to know its Hamiltonian. This means that we need to calculate the energy of the system, which brings us to the next step: quantizing the fields involved [31, 32], turning the field distributions into quantum operators.

Let us set the stage for where these process takes place. We are restricting ourselves to a nonlinear process which happens in a single spatial mode in the transverse direction and along a nonlinear material of length L. This is the case we are concerned with, which is an interaction taking place in weakly pumped waveguide structures in $LiNbO_3$. We are also dealing with Type-II SPDC throughout this work, so that we will always consider the signal and idler photons as orthogonally polarized. Furthermore, we are concerned with processes whose intensities is far lower than the pumping field's, so that we can treat the latter as a fully classical one. Lastly, we will assume a low enough pump power and efficiencies so that we can ignore time-ordering effects [33].

As it is usually the case, here we are not really interested in the evolution of the entire system. We are more interested in the interaction between the fields involved. To focus our attention, we can divide the total Hamiltonian into two parts [34]: one that describes the free evolution of each field, independently from the others, and one that describes the interaction among them. It is the latter that describes the nonlinear processes that we want to investigate. It can be

shown [35] that this interaction Hamiltonian can be written as

$$\hat{H}_{\text{SPDC}} = \mathscr{B} \int \mathrm{d}\omega_s \mathrm{d}\omega_i f(\omega_s, \omega_i) \hat{a}^\dagger(\omega_s) \hat{b}^\dagger(\omega_i) + \text{c.c.} \tag{1.25}$$

where $\mathscr{B}$ hides all the constants that arise from the quantization of the electric fields, depends on the pump power and the overlap integral between the spatial distributions of the fields in the waveguide. The suffixes s and i denote the signal and idler field which we have mentioned earlier, respectively. The operators $\hat{a}^\dagger(\omega_s)$ and $\hat{b}^\dagger(\omega_i)$ are the creation operators for the signal and idler modes at frequencies ω_s and ω_i.

We don't need to concern ourselves with the mathematical details of such formulation, just what's the physics behind it[9]. By reading the Hamiltonian in (1.25) we notice two things: a pump photon always decays into *two* lower energy photons and their spectral properties are completely described by the function

$$f(\omega_s, \omega_i) = \alpha(\omega_s + \omega_i) \phi(\omega_s, \omega_i) \tag{1.26}$$

where $\alpha(\omega_s + \omega_i)$ describes the pump spectrum and $\phi(\omega_s, \omega_i)$ is the phase-matching profile that we have derived earlier. This is the *joint spectral amplitude* (JSA) function, and its shape can tell us a great deal about the type of source we are dealing with.

Let's try to put things in perspective. What does this function *really* look like? As we said at the very beginning of this chapter, $LiNbO_3$ is extensively used to create photon sources, so let's plug in its characteristics into (1.26). If we pump a 3.5 cm long $LiNbO_3$ waveguide which has been periodically poled with a period of 9.21 µm with a pulsed laser centered at 775 nm and a 7 nm bandwidth, we obtain the simulated data of Figure 1.3. There, we have plotted the joint spectral *intensity*, because that's the quantity that can be actually measured in the lab.

Due to the shape of the phase-matching function and the requirement for energy conservation, we can see that the resulting photon pairs generated by this process are strongly anti-correlated in frequency. This means that the detection of a photon at a certain frequency tells us the frequency at which the second photon will be found, resulting in a pair of entangled photons. While some practical applications in quantum optics do rely on such correlations [36], others require photons with no correlations at all [37–39], so it's important to have a clear understanding of the spectral properties of the state that we want to use or manipulate.

1.2.2. Discretizing the spectral modes of a SPDC process.

How do we distinguish between a correlated and an uncorrelated JSA? Clearly, we need something more rigorous than our intuitions arising from looking at a plot. A requirement needed for the JSA to be uncorrelated is that it must be factorable into two function $h(\omega_s)$ and $g(\omega_i)$ that only depend on the frequency of the signal and the idler, respectively. To assess if the JSA satisfies this requirement, we can use the so-called *Schmidt's decomposition* [40, 41], which enables us to rewrite (1.26) into

$$f(\omega_s, \omega_i) = \sum_k \gamma_k h_k(\omega_s) g_k(\omega_i), \tag{1.27}$$

[9] Some might say that the mathematics behind *is* the physics. We agree to disagree.

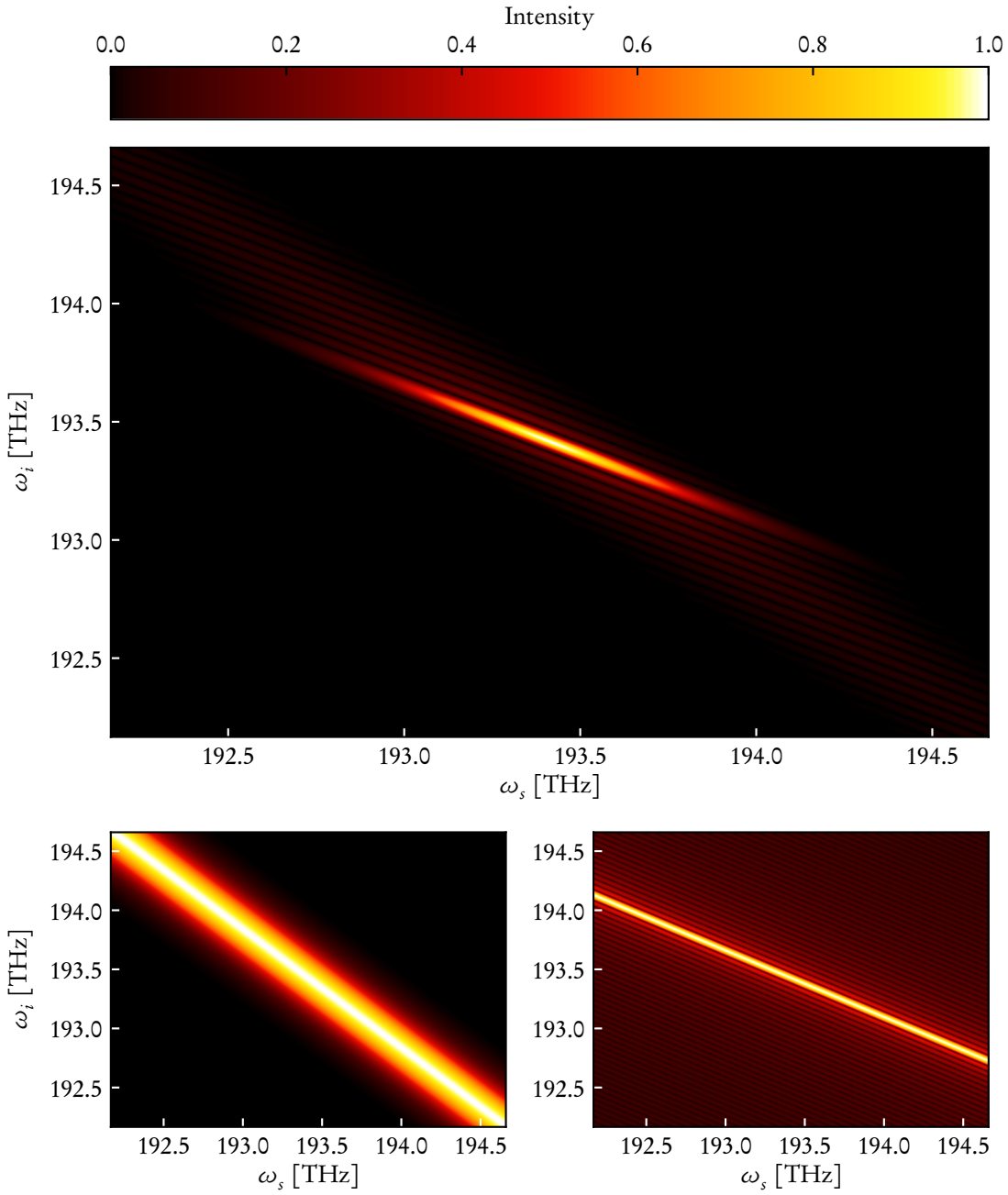

Figure 1.3.: Top: simulated JSI for a SPDC process where a 3.5 cm $LiNbO_3$ sample is pumped by a 7 nm broad pump pulse centered at 775 nm. Bottom left: pump envelope function. Bottom right: phase-matching profile. In order to enhance the contrast between the central peak and the side lobes of the phase-matching function, we have plotted the fourth root of the JSI. This allows us to clearly see how the pump spectrum is responsible for "selecting" the final spectral characteristics of the JSI.

where $h_k(\omega_s)$ and $g_k(\omega_i)$ are two sets of orthonormal functions and where the coefficients γ_k satisfy the normalization condition

$$\sum_k |\gamma_k|^2 = 1. \tag{1.28}$$

The condition for which the JSA is uncorrelated is then that

$$\gamma_0 = 1, \tag{1.29}$$

i.e. the decomposition is made up of only one pair of functions.

We can use (1.27) to define the following *broadband creation operators*

$$\hat{A}_k^\dagger = \int \mathrm{d}\omega\, g_k(\omega)\hat{a}^\dagger(\omega) \tag{1.30}$$

$$\hat{B}_k^\dagger = \int \mathrm{d}\omega\, h_k(\omega)\hat{b}^\dagger(\omega) \tag{1.31}$$

and finally rewriting our Hamiltonian as

$$\hat{H}_{\mathrm{SPDC}} = \mathscr{B} \sum_k \gamma_k \hat{A}_k^\dagger \hat{B}_k^\dagger + \mathrm{c.c.} \tag{1.32}$$

To understand what happens to our initial state, we need to let it evolve by using the Hamiltonian we have calculated. We will restrict ourselves to a case in which the bright pump field is not strong enough to make time-ordering effects relevant [33]. In this case, our output state, is

$$\begin{aligned} |\psi_{\mathrm{out}}\rangle &= \exp\left[\sum_k \left(\zeta_k^* \hat{A}_k \hat{B}_k - \zeta_k \hat{A}_k^\dagger \hat{B}_k^\dagger\right)\right] |\psi_{\mathrm{in}}\rangle = \\ &= \bigotimes_k \exp\left[\left(\zeta_k^* \hat{A}_k \hat{B}_k - \zeta_k \hat{A}_k^\dagger \hat{B}_k^\dagger\right)\right] |\psi_{\mathrm{in}}\rangle \\ &= \bigotimes_k \hat{S}_k(\zeta_k) |\psi_{\mathrm{in}}\rangle \end{aligned} \tag{1.33}$$

where we have defined

$$\hat{S}_k(\zeta_k) = \exp\left[\left(\zeta_k^* \hat{A}_k \hat{B}_k - \zeta_k \hat{A}_k^\dagger \hat{B}_k^\dagger\right)\right] \tag{1.34}$$

as the *squeezing operator* [32] and where the *squeezing parameter* ζ_k is proportional to the Schmidt's coefficient γ_k. In switching the sum inside the exponential to a product of exponentials we did not cheat. We are allowed to do this because the broadband operators that we have defined commute with each other, because the underlying functions that make them up are orthonormal.

This is quite an achievement: we changed our perspective and we can now deal with discrete orthogonal modes instead of a continuum of frequencies. Equation 1.33 is telling us something important, which will be exploited throughout this work: we can treat an SPDC process as being made up of independent squeezers, and we can only have an uncorrelated JSA if we have

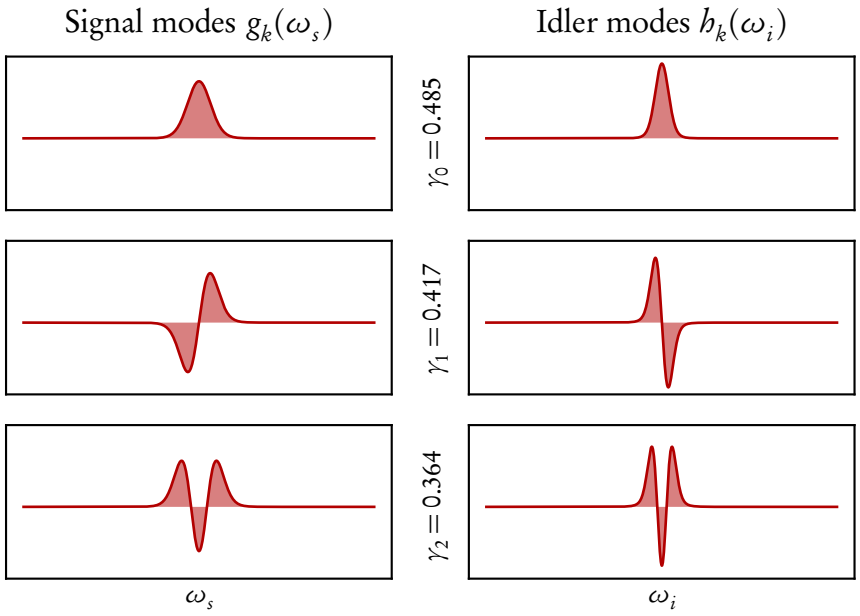

Figure 1.4.: Result of the Schmidt's decomposition of the JSA of Figure 1.3. Here we show the first few modes of the Schmidt's decomposition, with the respective coefficients γ_k.

a single one. This begs the question "*how many squeezers* (or Schmidt's modes) *are there in our previous example?*".

In the case of low pump power, we can define as the *effective* Schmidt's mode number K as the number of mode pairs necessary to describe the generated state, and it's defined as

$$K = \left(\sum_k |\gamma_k|^4 \right)^{-1}. \tag{1.35}$$

This is also linked to the *purity* of the state of each individual photon in the pair. We recover the state of one of the two photons by taking the partial trace over the subsystem of the other (e.g. we trace over the idler)

$$\rho_s = \mathrm{Tr}_i \, \rho_{\mathrm{SPDC}} = \mathrm{Tr}_i \, |\psi_{\mathrm{out}}\rangle\langle\psi_{\mathrm{out}}| \tag{1.36}$$

and we can calculate its purity $P_s = \mathrm{Tr}\, \rho_s^2$, obtaining

$$P_s = \mathrm{Tr}\, \rho_s^2 = \sum_k |\gamma_k|^4 = 1/K. \tag{1.37}$$

1.3. SPDC PROCESSES AS SINGLE PHOTONS SOURCES

When we described the Hamiltonian of a SPDC process, we focused on its spectral properties and we managed to wrestle free from a continuous description, adopting a more manageable

discrete one. We put aside a very important feature, however: the Hamiltonian of (1.25) clearly says that a pump photon decays into two output ones. If we separate these two photons—by means of a polarization-dependent beam splitter (PBS)—then we are *sure* that if one photon is detected at one of the ports of the PBS there *will be* another one at the other port (as depicted in Figure 1.5). This is the basic principle on which *heralded single-photon sources* (HSPS) operate, which have been demonstrated in various platforms [13, 42, 43]. The name comes from the fact that the detection even of one photon *heralds* the presence of a second one in the other mode.

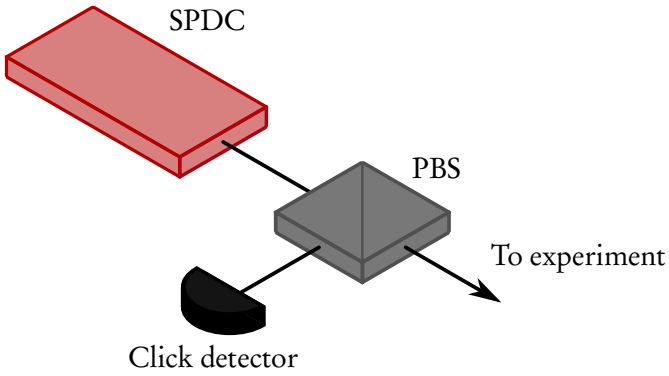

Figure 1.5.: Typical setup used for a HSPS. The two photons being generated by the SPDC can be separated by different means, depending on the process type (i.e. Type-I, II or 0). We are dealing with Type-II SPDC, which produces orthogonally polarized photons, so a PBS is enough to deterministically separate the two photons. Once one of these two photon is detected, we are sure that a twin photon has gone through the other port. We can use this knowledge to either process experimental data accordingly or (in more complex setups) adjust the configuration of the experiment in real-time.

The name heralded *single*-photon sources is misleading, however. While it is true that each pump can decay into two photons that satisfy momentum and energy conservation, the crucial point is that it *can*. There is no guarantee that it *will*. This makes these sources *probabilistic*, which is definitely a bug, not a feature.

1.3.1. From number of modes to number of photons

To understand the physical reason for this, let's get back to our description of the SPDC state (1.33). Let's assume for simplicity that we are dealing with an uncorrelated source, which has a single Schmidt's mode. Through thoroughly unexciting math tricks [32], we can rewrite the SPDC state as

$$|\psi\rangle_{\text{SPDC}} = \sqrt{1-|\lambda|^2}\sum_{n=0}^{\infty}\lambda^n\,|n,n\rangle \tag{1.38}$$

where we have defined

$$\lambda = -e^{i\phi}\tanh r \tag{1.39}$$

and

$$\zeta = re^{i\phi}, \qquad r, \phi \in \mathbb{R}. \tag{1.40}$$

Tracing over one of the two output modes, the probability of measuring n photons in the other is

$$p(n) = \left(1 - |\lambda|^2\right)|\lambda|^{2n}, \tag{1.41}$$

which is a thermal (or Bose-Einstein) distribution in disguise. To see this, we need to calculate the expected mean photon number of the selected mode, which is

$$\langle n \rangle = \sinh^2 r \tag{1.42}$$

which lets us re-write (1.41) as

$$p(n) = \left(\frac{\langle n \rangle}{\langle n \rangle + 1}\right)^n \frac{1}{\langle n \rangle + 1}. \tag{1.43}$$

The photon statistics for a correlated source is not the same as the one presented for a single-mode source. In fact, determining the probability of having produced n photons in one of the two subsystems (either of the idler or of the signal) only accounts to summing the probability of having a certain distribution of the n photons in k modes, which is a convolution of the statistics of the various single squeezers into which we have decomposed our source. In the limit of having a large number of modes, this approximates a Poissonian distribution.

1.4. Conclusion

It is time to delve into what are the consequences of the concepts laid out in this chapter. What do you *do* with this knowledge? We have the proper theoretical tools to describe the SPDC processes and we have seen how these can be exploited to construct single-photon sources. What we are missing are actual applications of such concepts.

In the next two chapters (taken and adapted from Refs. [44, 45]), we will show how such a single-photon source can be further integrated with other technologies, and how to overcome the problem of "purifying" correlated HSPS while maintaining high single-photon generation rates.

2. USING PHOTONS: SPDC SOURCES AS QUANTUM TESTBENCHES

Up until now, we have described SPDC sources seemingly in a vacuum[1]. While the study of the fundamental aspects of such sources is worthy in and of itself, many experiments only require these sources to have certain performances and characteristics, regardless of *how* these are achieved. The more times go on, the more experiments require a simple black box that "emits photons", whose state is specified on the datasheet of the box.

In this chapter—taken and adapted from Ref. [44], of which I'm author—we use an SPDC source as a test-bed to certify that other technologies (in this case, optical metasurfaces) are "quantum-ready", so to say. That is, we show that optical metasurfaces can be employed in a hybrid quantum photonics system with good performance, enabling highly integrated hybrid systems for applications requiring high-dimensionality, such as imaging, sensing, and computing.

2.1. COMBINING QUANTUM SOURCES WITH OPTICAL METASURFACES

State-of-the-art metasurfaces achieve essentially any kind of manipulation of light wavefronts for applications like ultra-flat lenses for imaging [46, 47], vector beam generation [48, 49], optical holography [50] and even nonlinear phase manipulation [51, 52]. While all these concepts solely rely on the classical electromagnetic description, the potential of metasurfaces for quantum applications is still widely unexplored. However, as versatile optical elements for locally altering the amplitude, phase, and polarization of light [53–55], metasurfaces can provide new functionalities to miniaturized quantum systems.

Recently, few initiatives have been taken to investigate the potential of metasurfaces in quantum optics. Jha et al. theoretically proposed that a metasurface can induce quantum interference between orthogonal radiative transition states of atoms [56] and quantum entanglement between two qubits [56]. Later, it was demonstrated that entanglement of spin and orbital angular momentum of a single photon can be generated via a metasurface [57] also, metasurface can provide a compact solution for quantum state reconstruction [58]. However, so far, there is only limited experimental evidence whether metasurfaces are suited for state manipulation in quantum optical experiments. If the current technology of metasurfaces can be directly applied to practical quantum applications, they can offer advanced solutions for quantum imaging [59, 60], sensing [61] and computing [3].

Here, we demonstrate entanglement and disentanglement of two-photon states using an all dielectric metasurface. Our metasurface allows the generation of path-entangled NOON states

[1] Yes, clearly the pun *is* intended.

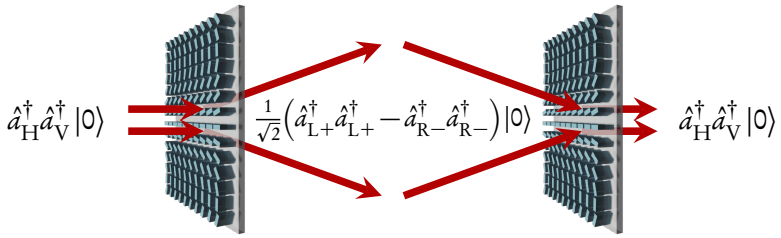

Figure 2.1.: Left: If a single photon pair with orthogonal linear polarization is inserted into the metasurface, it is divided into its circular polarization components. Since the inserted quantum state is a two-photon NOON state in the circular polarization basis, both photons will always choose the same output channel, and spatial entanglement is obtained. Right: The situation reverses for the insertion of a spatially entangled NOON state into the metasurface. The quantum interference leads to a projection back to the original orthogonal linear polarization states, and the photon pair is spatially disentangled.

with circular polarization due to the quantum interference effect. We observe a photon bunching within two spatially distinct output channels of the metasurface. Passing the same metasurface the second time, the generated path-entangled two-photon spin state can be disentangled, without introducing additional phase information. Our experiments indicate that metasurfaces are perfectly suited to provide large-scale and high-dimensional quantum functionalities with properties that go far beyond the conventional optical elements. Thus, hybrid integration of quantum optical elements together with metasurfaces offers the promise for delivering robust multi-photon entanglement and high dimensional quantum applications [62].

2.2. Entanglement and disentanglement

Precise control and preparation of multi-photon entanglement are of fundamental interest for quantum technologies. With the accurate manipulation of the single photons wavefront by a metasurface, spatial and polarization-based entanglement can be achieved. In our case, the metasurface is designed to spatially separate the generated circular polarization states of light and thus enforces a quantum states representation in that particular basis, as sketched in Figure 2.1.

The operation of the metasurface in use is two-fold: first, it converts a circularly polarized state into its cross-polarization equivalent and then spatially separates left and right polarization states. Now, remember what a SPDC state looks like from (1.38). We assume that we are using such a low pump power that $\lambda \gg \lambda^n$ for $n > 1$, so that we can ignore all high-order pairs. This brings us to consider as our input state, after post-selecting on two photon events to ignore vacuum contributions, simply

$$|\psi\rangle_i = \hat{a}_{\mathrm{H}}^{\dagger}\hat{a}_{\mathrm{V}}^{\dagger}|0\rangle \tag{2.1}$$

where we use the indices H and V for the horizontal and vertical polarization states and L and R for the left and right circular polarization states, and the suffix i stands for input. We are also

assuming that the two photons are completely indistinguishable *except* for their polarization state.

Given the operation applied by the metasurface, it's more convenient to switch bases from linear to circular polarization. Keeping in mind that the relationship between the two is

$$\hat{a}_{\mathrm{R}}^{\dagger} = \frac{1}{\sqrt{2}}\left(\hat{a}_{\mathrm{H}}^{\dagger} - i\,\hat{a}_{\mathrm{V}}^{\dagger}\right) \tag{2.2}$$

$$\hat{a}_{\mathrm{L}}^{\dagger} = \frac{1}{\sqrt{2}}\left(\hat{a}_{\mathrm{H}}^{\dagger} + i\,\hat{a}_{\mathrm{V}}^{\dagger}\right) \tag{2.3}$$

we can plug the inverse relationship into (2.1) to obtain

$$|\psi\rangle_i = \frac{1}{\sqrt{2}}\left(\hat{a}_{\mathrm{L}}^{\dagger}\hat{a}_{\mathrm{L}}^{\dagger} - \hat{a}_{\mathrm{R}}^{\dagger}\hat{a}_{\mathrm{R}}^{\dagger}\right)|0\rangle\,, \tag{2.4}$$

where we have dropped a global phase factor of $-i$.

This *looks* like an entangled state, but it's not, because entanglement is a physical property of a system, not a mathematical artifact (e.g. a base choice). After propagation through the metasurface though, the state is also spatially separated and cannot be decomposed into two single-photon states and is therefore path-entangled. We can write our output state, after the metasurface, as

$$|\psi\rangle_o = \frac{1}{\sqrt{2}}\left(\hat{a}_{\mathrm{L}+}^{\dagger}\hat{a}_{\mathrm{L}+}^{\dagger} - \hat{a}_{\mathrm{R}-}^{\dagger}\hat{a}_{\mathrm{R}-}^{\dagger}\right)|0\rangle \tag{2.5}$$

where the new suffixes + and − denote the spatial mode.

The form of (2.5) is known in the literature as NOON state: in general, NOON states are entangled N-photon quantum states, which are commonly used for quantum metrology. Formally, these states can be written as a superposition of two quantum states with all photons allocated in only one of the two channels [63]:

$$|\mathrm{NOON}\rangle = \frac{1}{\sqrt{2}}(|N\rangle\,|0\rangle + |0\rangle\,|N\rangle). \tag{2.6}$$

Interestingly, the same metasurface can be used in the reverse process, in which the circular polarization states are spatially recombined to disentangle the generated state. We utilize the polarization basis change functionality to build a metasurface-based interferometer, in which the balanced beamsplitters (BS) of a standard Mach-Zender type interferometer are replaced by two equal metasurfaces as we have described. By tuning the phase delay φ between the two arms of the interferometer, we obtain the quantum state (which we will fully derive later in this chapter)

$$|\psi\rangle_o = \left(\frac{1}{2}\hat{a}_{\mathrm{H}}^{\dagger}\hat{a}_{\mathrm{V}}^{\dagger}\left(e^{-i\,2\varphi}+1\right) - \frac{1}{4}i\left(\hat{a}_{\mathrm{H}}^{\dagger}\hat{a}_{\mathrm{H}}^{\dagger} - \hat{a}_{\mathrm{V}}^{\dagger}\hat{a}_{\mathrm{V}}^{\dagger}\right)\left(e^{-i\,2\varphi}-1\right)\right)|0\rangle \tag{2.7}$$

in which we can distinguish two cases. For $\varphi = (n+1/2)\pi$, with $n \in \mathbb{Z}$

$$|\psi\rangle_o = \frac{1}{2}\left(\hat{a}_{\mathrm{H}}^{\dagger}\hat{a}_{\mathrm{H}}^{\dagger} - \hat{a}_{\mathrm{V}}^{\dagger}\hat{a}_{\mathrm{V}}^{\dagger}\right)|0\rangle \tag{2.8}$$

which is a path-entangled NOON state, up to a global phase factor, while for $\varphi = n\pi$, with $n \in \mathbb{Z}$

$$|\psi\rangle_o = \hat{a}_{\mathrm{H}}^{\dagger}\hat{a}_{\mathrm{V}}^{\dagger}|0\rangle \tag{2.9}$$

which is the same as our input state. We will investigate both the NOON state generation capabilities of a single metasurface sample and also the tunability of the generated entanglement in a Mach-Zender type interferometry experiment.

2.3. METASURFACE DESIGN AND FUNCTIONALITY

For the experiments, we partnered with the group of Prof. Dr. Thomas Zentgraf, which designed, produced, and tested the metasurface. The metasurface sample is designed to deflect the incident light into two different output directions under angles of $\pm 10°$. The deflection is obtained by using a space-variant Pancharatnam-Berry-phase that results from the polarization conversion for the transmitted light [64]. As a platform for the metasurface, we use silicon nanofin structures. They act as local half-wave plates, which convert the circular polarization states into their cross polarization and add a spatial phase term based on their orientation angle. For our design, we choose a linear phase gradient, which diffracts the incoming light under the desired angle. We note that the sign of the phase gradient explicitly depends on the helicity of the circularly polarized light, which effectively makes our metasurface essentially a spatial separator for the circular polarization states.

2.4. GENERATING NOON SPIN STATES

First, we investigate the NOON-state generation at the metasurface. A key quantum feature of the NOON state is its photon bunching characteristics, i.e. we expect that both photons will always choose the same metasurface output channel after inserting the quantum state (2.1). To demonstrate this bunching effect, we use the setup shown in Figure 2.2. It contains four logical parts: a two-photon source for the generation of the initial quantum state, a Michelson interferometer to adjust the time delay between these two photons, a metasurface as a quantum interference device, and a single-photon detection system. To control the time delay between the two photons, we use a modified Michelson interferometer with a PBS and two quarter-wave plates (QWP). Since the time delay directly influences the temporal overlap between both photons, we utilize it to enable ($\tau = 0$) and disable ($\tau \to \infty$) the quantum interference effect at the metasurface. In the case of no interference, the two photons will choose either output with a 50% chance, while in the case of perfect interference, both photons will always choose the same random output port.

To characterize the generated quantum state, we perform two different coincidence measurements for various time delays τ. First, we measure the number of coincidences between both output channels of the metasurface. The generated NOON state should not contribute to the number of registered coincidences, ideally leading to zero coincidence counts. However, when the initial $|HV\rangle$ photons do not arrive simultaneously at the metasurface, we expect a 50% coincidence probability per inserted photon pair (without losses). Thus, as we vary the time delay τ, we expect the well-known Hong-Ou-Mandel (HOM) correlation dip. Note that

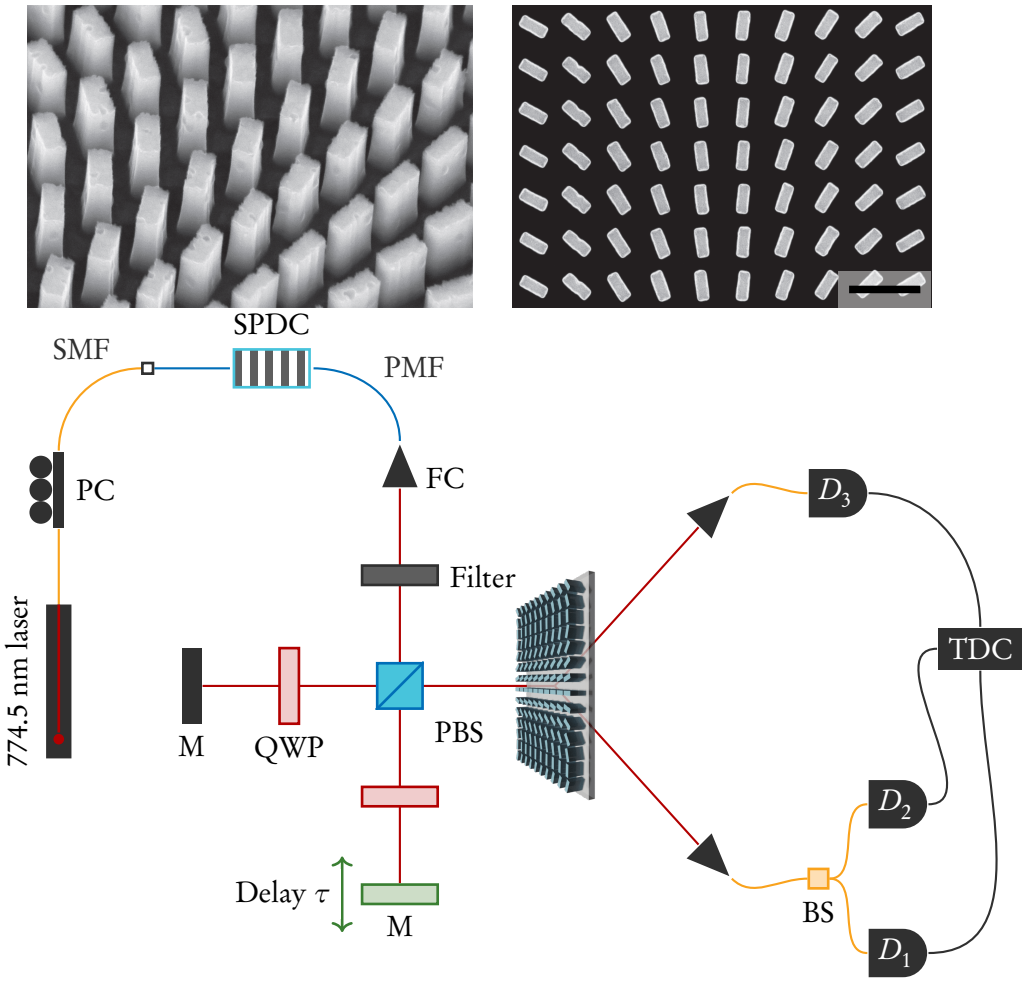

Figure 2.2.: Top: scanning electron microscopy images at 45° (left) and the top view (right) for a small area of the fabricated silicon metasurface (scale bar: 1 µm). Bottom: the two-photon source creates a photon pair with orthogonal linear polarizations by SPDC. The two photons are temporally delayed relative to each other by τ with a Michelson interferometer containing a PBS and QWPs. The photon pair passes through the metasurface where the NOON state is generated. The spatially entangled state is then analyzed by a coincidence measurement system in two different configurations with single photon detectors (D_n). PMF polarization-maintaining fiber, SMF single mode fiber, M mirror, PC polarization controller, TDC time-digital converter.

a visibility higher than 50% verifies the quantum character of interference for these HOM experiments [40].

Second, we measure the number of coincidences between the two outputs of a 50:50 BS that has been placed in one of the output channels of the metasurface. Coincidence counts for this measurement can be obtained only when both photons choose the same output channel of the metasurface. Since the probability for this event is twice as large in the case of interference, we expect a 2:1 ratio in the coincidence counts between $\tau = 0$ and $\tau \to \infty$. Both coincidence measurements are performed simultaneously by using three superconducting nanowire single-photon detectors. One of these detectors (D_3) is directly connected to one of the metasurface output channels, while the other two detectors (D_1 and D_2) are placed behind an integrated BS (a 3-dB fiber coupler), which is connected to the second metasurface output channel. In this configuration, the first coincidence measurement between the two metasurface channels can be calculated as $C_{13} + C_{23}$, where C_{ij} refers to the coincidence rate between the detectors D_i and D_j.

The coincidences show a clear dip at zero-time delay with a high visibility of $(86 \pm 4)\,\%$ (Figure 2.3, top). Note that the visibility clearly exceeds the limit of 50%, which can be achieved with classical coherent light. At the same time, the second coincidence measurement (C_{12}) shows a clear coincidence peak ("anti"-HOM peak) at $\tau = 0$, which confirms that the two photons are always bunched together in one output channel (Figure 2.3, bottom). In the case of interference, both measurements show that the probability of at least one photon in each output channel decreases (first measurement), while the probability of at least two photons in one output channel increases (second measurement). Thus, photon bunching occurs.

To put the performance of the metasurface in perspective, we carry out a calibration experiment for the SPDC source on its own. This experiment is inspired by [40] and allows us to determine an upper bound on the achievable HOM visibility. Here, we use a half-wave plate (QWP) to rotate the linear polarization states to the diagonal (D) and anti-diagonal (A) bases creating the quantum state

$$\hat{a}_{\mathrm{D}}^{\dagger}\hat{a}_{\mathrm{A}}^{\dagger}|0\rangle = \frac{1}{2}\left(\hat{a}_{\mathrm{H}}^{\dagger}\hat{a}_{\mathrm{H}}^{\dagger} - \hat{a}_{\mathrm{V}}^{\dagger}\hat{a}_{\mathrm{V}}^{\dagger}\right)|0\rangle \tag{2.10}$$

where we have defined

$$\begin{aligned} \hat{a}_{\mathrm{D}}^{\dagger} &= \frac{1}{\sqrt{2}}\left(\hat{a}_{\mathrm{H}}^{\dagger} + \hat{a}_{\mathrm{V}}^{\dagger}\right) \\ \hat{a}_{\mathrm{A}}^{\dagger} &= \frac{1}{\sqrt{2}}\left(\hat{a}_{\mathrm{H}}^{\dagger} - \hat{a}_{\mathrm{V}}^{\dagger}\right). \end{aligned} \tag{2.11}$$

This state is then inserted into a fiber PBS, where the two photons interfere creating once again a two-photon NOON state. This "reference" experiment shows a visibility of $(89 \pm 5)\,\%$, which is in agreement for the value found for the case in which the metasurface is used.

2.5. METASURFACE-BASED INTERFEROMETER

Next, we study whether the metasurface also preserves the quantum coherence of the generated state, i.e. the phase relations between the components of the superposition are fixed and not

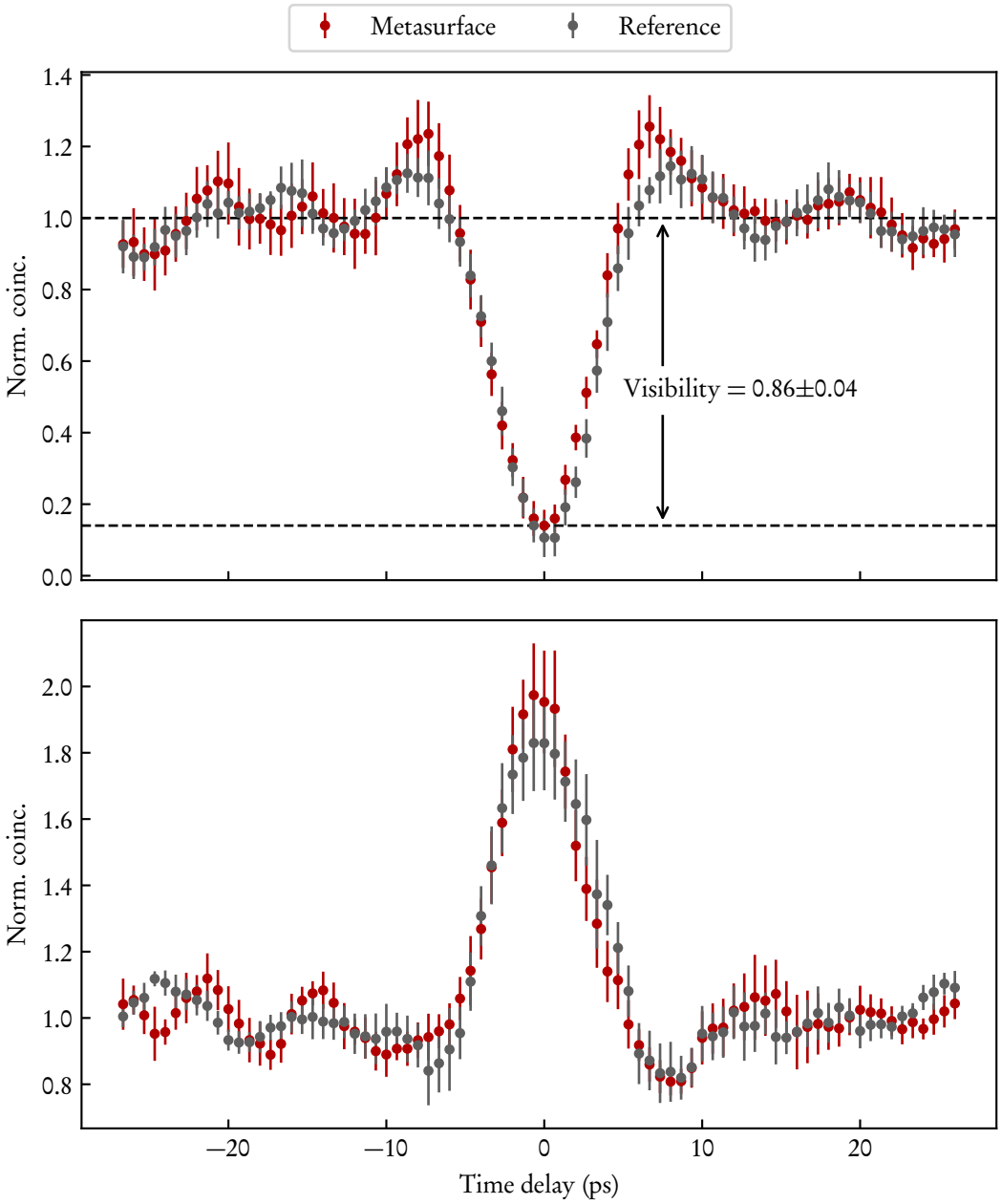

Figure 2.3.: Top: normalized coincidence counts ($C_{13} + C_{23}$) between the two output channels of the metasurface for a variation of the initial photon time delay. The high visibility beyond the classical limit of 50% confirms the expected quantum interference effect. The reference is obtained for a standard (HOM) experiment with a standard BS to characterize the quality of the photon source. Bottom: normalized coincidence counts C_{12} between detectors D_1 and D_2 for the measurement with the polarization BS in one output channel of the metasurface. The peak in the coincidence counts of the "anti"-HOM measurement confirms that the two photons always take the same output channel.

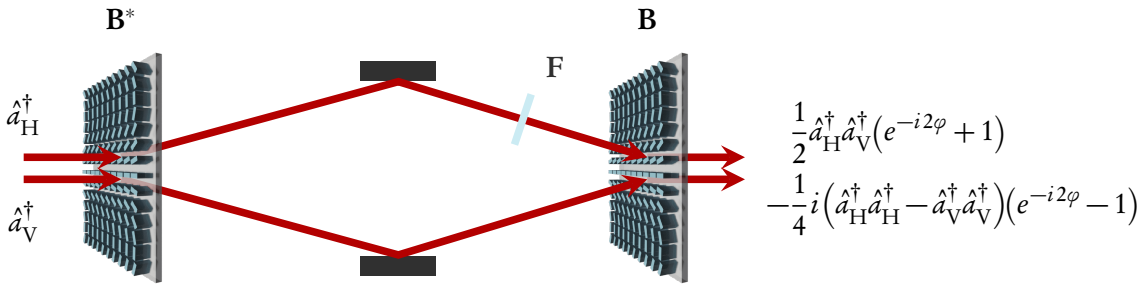

Figure 2.4.: Schematic representation of a MBI and the relationship between the input modes 1 and 2 (left side, H and V) and the outputs 3 and 4 (right side, H and V). The transformation $\mathbf{M} = \mathbf{B}^* \cdot \mathbf{F} \cdot \mathbf{B}$ is here laid out by labeling each component with its respective transformation matrix. Black rectangles are mirrors, blue rectangle is a phase-shifter.

randomly redistributed. Such coherence is important in quantum metrology applications, where phase measurements play a key role. For that, we realized a folded metasurface-based interferometer (MBI) in which the photons pass through the metasurface twice (Figure 2.4). By tilting a 130 µm-thick glass plate in one of the two arms of the interferometer, we introduce a phase difference between the two optical paths. The final state is then separated and analyzed at a PBS.

2.5.1. Mathematical description of the MBI

To better understand the discussion that follows, it's best to describe in general how the MBI acts on a single photon entering it from either input mode, which will also justify the form of (2.7). We are looking for a transformation $\mathbf{M}$ which expresses the input modes 1 and 2 in term of the output modes 3 and 4 (Figure 2.4). This will be handy when we calculate expectation values on those modes, so we will start our construction of such transformation "backwards", i.e. starting from the last metasurface in the MBI. In what follows, keep in mind that we are going to assume no losses, since they don't play an interesting role.

The transformation we are seeking for just a single metasurface is

$$\mathbf{B} = \frac{1}{\sqrt{2}}\begin{pmatrix} 1 & i \\ 1 & -i \end{pmatrix} \tag{2.12}$$

which is the inverse transformation from (2.5) to $|HV\rangle$. Next, the matrix that introduces a phase between the two arms of the interferometer is

$$\mathbf{F} = \begin{pmatrix} e^{-i\varphi} & 0 \\ 0 & 1 \end{pmatrix}. \tag{2.13}$$

Finally, we need to invert (2.12) in order to perform the initial transformation of the interfero-

meter, leading us to the final transformation

$$\mathbf{M} = \mathbf{B}^* \cdot \mathbf{F} \cdot \mathbf{B} = \frac{1}{2}\begin{pmatrix} e^{-i\varphi}+1 & i\left(e^{-i\varphi}-1\right) \\ -i\left(e^{-i\varphi}-1\right) & e^{-i\varphi}+1 \end{pmatrix} \tag{2.14}$$

We will consider two cases in what follows: Fock and coherent input states. The reason for that is that coherent states are the hallmark of "classicality" in quantum optics, while Fock states are "truly" quantum. You can argue (and you would find me agreeing) that classical *is* quantum plus some assumptions, and this forced "border" between quantum and classical worlds is at best misleading. On the other hand, it is hard (and sometimes counterproductive) to avoid accepted conventions, so we will follow the vast amount of literature that makes this distinction.

First let's deal with a coherent (classical) input in one arm of the interferometer and the vacuum in the other. Our derivation of the full transformation **M** has been done in terms of single-photon creation operators, so it's much more convenient expressing our coherent state in the number basis

$$|\alpha\rangle = e^{\frac{|\alpha|^2}{2}} \sum_0^\infty \frac{\alpha^n}{\sqrt{n!}} |0\rangle = e^{\frac{|\alpha|^2}{2}} e^{\alpha \hat{a}^\dagger} |0\rangle . \tag{2.15}$$

We know how one input mode is transformed by the MBI because we have derived its matrix **M**, which links inputs and outputs as

$$\begin{pmatrix} \hat{a}_1^\dagger \\ \hat{a}_2^\dagger \end{pmatrix} = \mathbf{M} \begin{pmatrix} \hat{a}_3^\dagger \\ \hat{a}_4^\dagger \end{pmatrix} \tag{2.16}$$

and we are assuming that vacuum is in mode number two, hence at the MBI output

$$|\psi_\alpha\rangle = e^{\frac{|\alpha|^2}{2}} e^{\alpha \hat{a}_1^\dagger} |0\rangle = e^{\frac{|\alpha|^2}{2}} e^{\frac{\alpha}{2}\left(e^{-i\varphi}+1\right)\hat{a}_3^\dagger} e^{i\frac{\alpha}{2}\left(e^{-i\varphi}-1\right)\hat{a}_4^\dagger} |0\rangle \tag{2.17}$$

We can now calculate what we expect as single count rates at each output mode of them MBI and coincidence rates, as a function of the relative phase between the two arms of the interferometer. If we define the coincidence counts as

$$C = \langle \psi | \hat{n}_3 \hat{n}_4 | \psi \rangle , \tag{2.18}$$

where $|\psi\rangle$ is the input state, we obtain

$$C = \frac{|\alpha|^2}{4} \sin^2(\varphi). \tag{2.19}$$

On the other hand, calculating the average number of photons collected at either detector yields

$$\begin{aligned} N_3 &= |\alpha|^2 \cos^2\left(\frac{\varphi}{2}\right) \\ N_4 &= |\alpha|^2 \sin^2\left(\frac{\varphi}{2}\right). \end{aligned} \tag{2.20}$$

This shows that we expect the number of coincidences to oscillate twice as fast with respect to the single counts in each arm. This makes sense intuitively, because the maximum rate at which

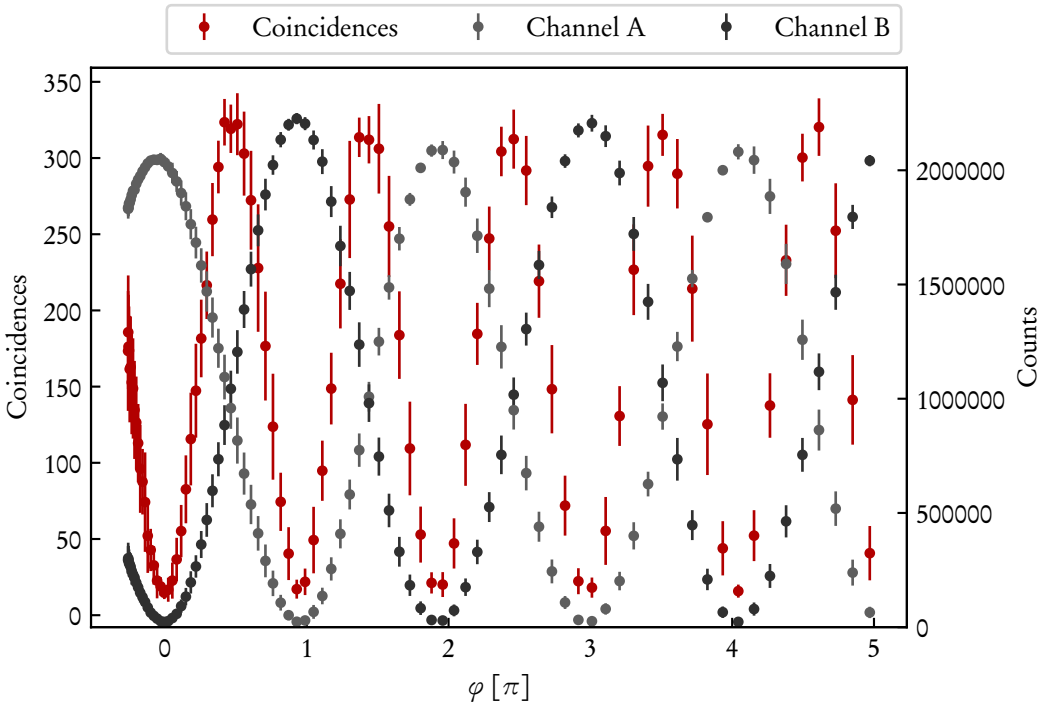

Figure 2.5.: Interference pattern due to the propagation of a weak coherent state through the MBI. We can see that, as predicted by (2.19) and (2.20), the coincidence count rates oscillate twice as fast as the single count rates. This can be interpreted as the coincidences being the product of the single counts.

we are going to detect two photons simultaneously is when the same number of photons reaches each detector. When the phase is such that either detector has the highest intensity, it also means that the other has no photons at all impinging on it, hence there can be no coincidences.

The situation changes drastically if we use single photons as input state, i.e. $|\psi\rangle = \hat{a}_H^\dagger \hat{a}_V^\dagger |0\rangle$. Calculating the expected coincidence rates yields

$$C = \cos^2(\varphi) \tag{2.21}$$

while for the single count rates

$$\begin{aligned} N_3 &= 1 \\ N_4 &= 1. \end{aligned} \tag{2.22}$$

This is in stark contrast with the coherent case: while in that case we had an oscillating behavior for the single count rates, here we see a constant detection rate. This is due exclusively to the input state's nature.

2.5.2. Experimental realization

Let's now implement experimentally what we have just discussed. First, we use a strongly attenuated laser as a weak coherent input state. For the input state

$$|\psi\rangle = |\alpha_H 0_V\rangle, \tag{2.23}$$

i.e. a coherent state in one input and vacuum in the other, the count rates in both output ports of the MBI show an oscillating behavior (Figure 2.5). At the same time, the coincidences show an oscillating behavior with double the frequency, following a $\sin^2(\varphi)$ function. This behavior can be understood from a classical point of view, where the coincidence corresponds to the product of the single counts. Note that φ corresponds to the introduced total phase by passing twice through the tilted glass plate. This is the same behavior that we were expecting according to (2.20) and (2.19).

Next, we launch one photon per input mode $|HV\rangle$ by using the photon pairs from the SPDC source. We observe that the counts at each individual MBI output channel will be constant regardless of the introduced phase φ (Figure 2.6). This is due to the first-order correlation between two MBI outputs being independent of φ. However, when we determine the coincidences between the two outputs, we observe the same double frequency oscillation from the coherent case, which is now phase shifted accordingly. When two orthogonally polarized photons arrive at the metasurface simultaneously, there is no coincidence contribution in the HOM experiment due to the photon bunching effect. In this scenario, path-entangled photon pairs are generated at the metasurface. Thus, the visibility of interference fringes from the MBI is $(86.8 \pm 1.1)\,\%$. In addition, further experiments for various time delays between the initial two photons show a reduced visibility of the coincidence rate. When one photon is delayed by 3 ps, the normalized HOM coincidence rate of approximately 50% tells us that the two photons still overlap partially in time. For this partial overlap, the visibility of the interference fringes is $(67 \pm 2)\,\%$. If one photon is delayed by more than 17 ps, they arrive at the MBI one after the other, with negligible overlap. Correspondingly, no path entanglement is generated inside the MBI. This is in good agreement with our experimental visibility of $(45 \pm 5)\,\%$ for the coincidence rate. The high visibility of the interference fringes in the coincidences rate is higher than the violation limit of Bells inequalities (70.7%) [65]. This underlines how the quantum nature of the state manipulated by the MBI is retained, given that such result cannot be explained with a classical theory.

In contrast to the coherent case, the coincidence counts can no longer be perceived as the product of the single counts. This pure non-classical effect is a key feature of quantum interferometry that is closely related to photon entanglement. The peaks in the coincidences result from the second-order correlation of the entangled NOON spin state with circular polarization, which is generated after passing through the metasurface the first time. Passing through the entire MBI, the entangled NOON spin state is disentangled into the original two-photon state $\hat{a}_{\mathrm{H}}^{\dagger}\hat{a}_{\mathrm{V}}^{\dagger}|0\rangle$ if there is no phase difference between two MBI arms (first term in (2.7)). After splitting the state at a PBS, the two photons arrive at the two detectors simultaneously, which causes the maximum coincidence rates. On the other hand, the minima in the coincidences result from the second-order correlation of the entangled NOON state with linear polarizations (second term in (2.7)). For phase differences of $\varphi = (n + 1/2)\pi$ with $n \in \mathbb{Z}$, the output of the MBI is

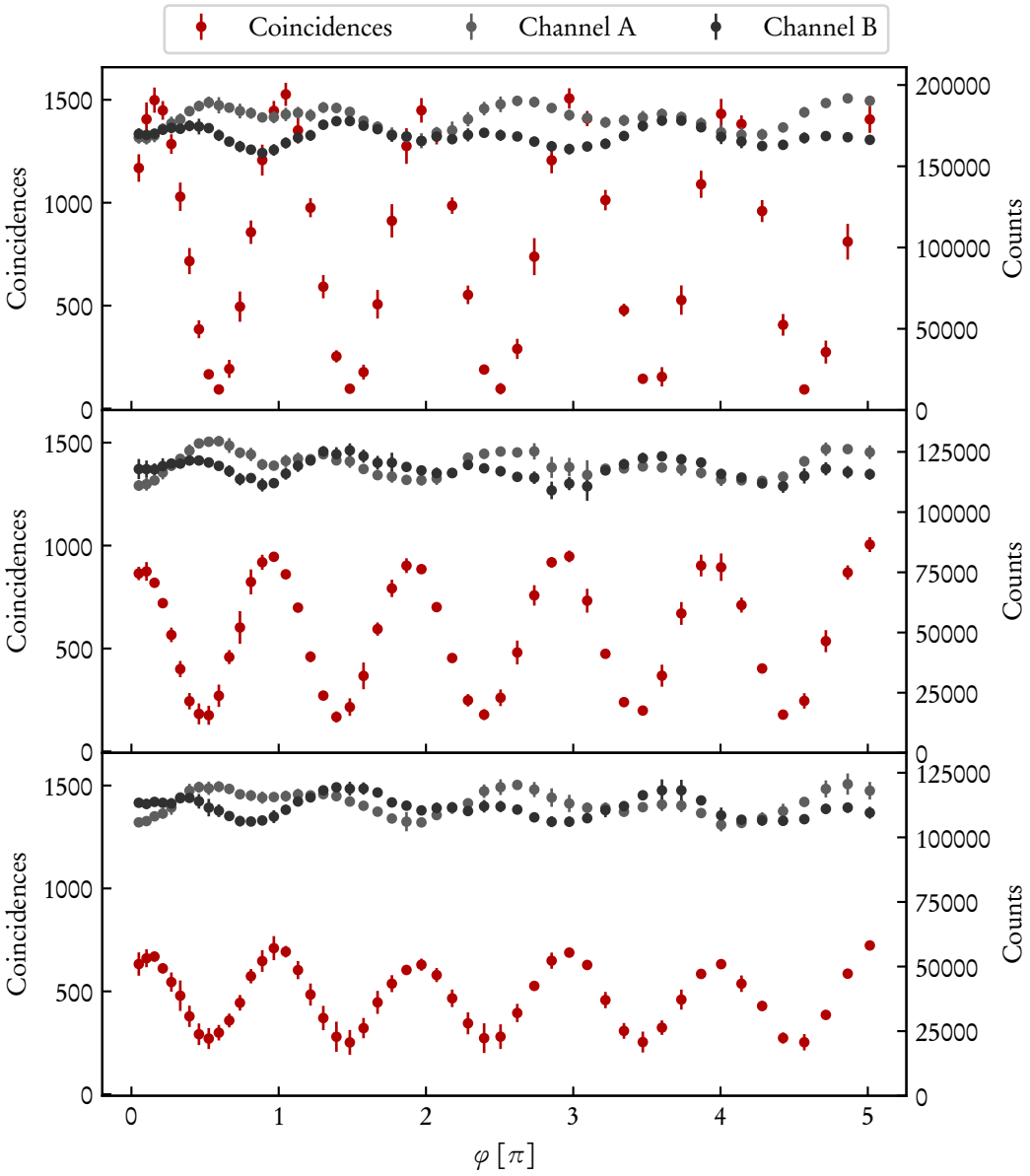

Figure 2.6.: Experimental results for the two-photon state with three different time delays τ after passing through the MBI. The count rates at both detectors are independent of the introduced phase φ and the time delay τ. The measured coincidence rates show an oscillatory behavior with lower visibility at higher delay times. The obtained visibility values are $(86.8 \pm 1.1)\,\%$ for the case of no time delay (top), $(67 \pm 2)\,\%$ for a delay of 3 ps (middle) and $(44 \pm 5)\,\%$ for 17.7 ps (bottom).

solely determined by the second term of (2.7). The two photons are either in the H or V path, but they cannot be in both paths simultaneously. Hence, there is no coincidence contribution, similar to the HOM effect, as shown in Figure 2.3.

2.6. Conclusion

Integrated photonic quantum experiments are routinely performed using large-scale optical components such as directional couplers and BSs. With our experiments, we demonstrate the preparation of spatial entanglement and disentanglement based on a metasurface in a more compact setting. The results are especially remarkable since the metasurface consists of spatially distributed nanostructured elements with slightly different scattering properties. The experiments confirm that quantum entanglement and interference take place at our dielectric metasurface, while phase-sensitive effects (quantum coherence) are preserved. Our findings demonstrate that metasurfaces can achieve an interference performance similar to that of traditional optical components and are indeed viable candidates for integrated quantum nanosensors and quantum interferometry.

Here, we focused on a metasurface for entanglement and interference and therefore for state manipulation purposes. This metasurface operates as one of the basic building blocks of typical photonic quantum circuits, which splits and recombines optical modes in nested interferometers. However, metasurfaces have enormous potential in quantum optics. Their ability to fully control the wavefronts of light can be used to generate multiphoton and high-dimensional entanglement with different spin-OAM. Combining multiple optical functionalities into a single metasurface as an efficient and compact quantum optical device might dramatically improve the performance and even lead to new concepts for practical quantum applications. Since metasurfaces can be used directly at waveguides and fiber-end facets, these hybrid nanophotonics systems for arbitrary basis transformation can be used for robust integrated quantum technologies, from sensor arrays to quantum simulators. In this context, future research has to show whether metasurfaces can directly generate quantum states, such as single photon pairs, in a well-defined and efficient way without the need for an additional source.

This is one example of the maturity of SPDC sources. But the transition from research interest to practical instruments means also that now we need to care more about the performance of such sources. This is what we are going to focus on in the next chapter, where we explore the requirements of having a spectrally decorrelated source with high generation rates.

3. Heralding photons: catching false-positives when filtering SPDC sources

SPDC photon-pair sources are routinely used in quantum optics experiments and, as we have described in the previous chapter, can be used with other technologies to further drive down the required footprint of the overall experiment.

Of course, different experiments require different parameters and the SPDC must be tailored to provide the best performance possible based on those parameters. One example is experiments in which we require not only single photons, but also *pure* photons [66–72]. This chapter is taken and adapted from Ref. [45], of which I'm author.

3.1. The problem with probabilities

We have seen in subsection 1.3.1 that even a source described by a single Schmidt's mode can generate multiple photon pairs at a time. This is of course not a violation of energy conservation, each photon pair will always require the annihilation of a pump photon! The point is that we are dealing with pump pulses which contain millions of photon each, so we can basically treat them as an "infinite" reservoir of pump photons. But even so, experiments involving SPDC tend to keep the mean photon number generated per pulse fairly low [13].

Why is that so? Since we don't live in a theoretical world, where our instruments are the most convenient projection operator possible, we need to use imperfect solutions and compromises. The biggest one is to drop the possibility of *actually* counting how many photons we have in a single mode. In the discrete variable world, the most widespread type of detector is the so-called "bucket" or "click" detector (the technology on which they are based is irrelevant for our discussion). The reason they are called like that is because the only feedback they give is if a photon triggered their detection mechanism, but this mechanism becomes insensitive to further stimulation as soon as it fires. That means that if $n > 0$ photons are impinging on the detectors, the signal we receive is a simple 0 (no detection) or 1 (detection), regardless of how many photons were actually there. There is ongoing work to develop *true* photon-number resolving detectors [73, 74] or so-called *pseudo*-number-resolving detectors, by multiplexing click-type ones [75, 76]. Both of these approaches are promising, but far from being a common tool in quantum optics experiments.

Since we have to live with such limitations (for now, at least), and our objective is still to produce *single* photons, any pump pulse that produces more than one photon pair is detrimental for our purposes and we will regard it as noise. Since the detectors that we use can't distinguish

between one or more photons, it's important to reduce as much as possible these additional contributions.

If we start from a correlated source, the simplest tool at our disposal is of course spectral filtering [77]. This gives us the necessary purity that our experiment requires, but at the cost of limited generation rate of "useful" event, since most of them will be suppressed by the filter itself. A naïve solution is simply to increase the average power per pulse to recover the lost generation rate. But filtering happens *after* the SPDC process and thus it does not change the photon statistics of the single mode it selects. This means that increasing the pump power is not a viable strategy if we want to still keep the single-photon character of the source. Since our detectors cannot count photons, we need to keep the overall probability of generating more than one photon negligible (as in the plot on the bottom left of Figure 4.1) so that *if* our detector clicks, we are fairly sure that it was because of a single photon.

To improve the single photon generation rate of these sources while keeping the noise low, multiple strategies can be used. A difficult but promising approach is multiplexing (detailed later in this work), where multiple sources are combined together with feed-forward switching to improve the rate of single photon generation without increasing the noise. Common schemes are spatial multiplexing [78, 79], time multiplexing [80] and frequency multiplexing [81, 82].

While these are encouraging results, they usually come with a large hardware overhead and additional setup complexity and losses when compared to single sources. To avoid these drawbacks other methods can be used to achieve better performance in certain metrics from a single SPDC source. For example, a combination of high pump repetition rate and spectral filtering has been used [83] to increase the generation rate of single-photons. Alternatively, photon-number-resolving detection can be used to eliminate higher order photon contributions, decreasing the multi-photon noise [84, 85].

Note however, when the herald photon is filtered, many unheralded photons are sent to the heralded arm. Some systems cannot rely on post-processing alone to eliminate these unheralded photons, due to their sensitivity on incoming photon flux (e.g. detection systems based on transition edge sensors [74]). In this case, active feed-forward and electro-optical switches provide a solution, only opening the path to the heralded detector after the herald photon has been detected [86–88]. This approach uses off-the-shelf telecom equipment and thus relies on proven, cost-effective technology only.

In this chapter, we present a scheme which ensures high spectral and photon-number purity of the generated state by conditioning on heralding events both within and outside the filter bandwidth, and add to this an active feed-forward strategy that physically removes unwanted photons. Our method does not pollute the heralded arm of the SPDC state with noise photons and constrains the photon flux to a minimum for single-photon sensitive applications. We compare our scheme with the case of standard passive spectral filtering and measure the reduction in the noise due to our removal of higher order photon number contributions. A measure of this noise is given by the heralded second order correlation function ($g_h^{(2)}(0)$) and we register a maximum improvement of 21%, limited by losses in the heralding arm.

3.2. THEORY

For the best heralding efficiency, often only the heralding photon is filtered. This can still project the heralded photon into a single spectral mode as long as the filter is tight enough [89]. A problem arises if the modes which the filter removes in the heralding arm are still present in the heralded arm, leading to uncorrelated noise. In particular highly multi-mode SPDC states with strong spectral correlations, which are typical for standard waveguide sources, require significant filtering to achieve spectral purity and are strongly affected by this pollution. To counteract this shortcoming we introduce the concept of *extended heralding* (Figure 3.1). Here, we take the idler output of a SPDC source and we filter it in order to increase the purity. We exploit the additional information gained by detecting not only the transmitted light of filter in the heralding arm, but also the rejected part of the spectrum which is normally discarded. We use the additional information present in the reflected heralding mode to improve the photon statistics of the heralded mode, namely by discounting events where a photon is detected in both transmitted and reflected ports, reducing multi-photon events. A field-programmable gate array (FPGA) closes an electro-optic switch only when a photon is detected at the transmission port of the filter, and no photon is present at the reflected port. We can then analyze the photon statistics via a time-to-digital converter (TDC).

We follow the description of Ref. [85] with the addition of filtering and extended heralding, comparing the fidelity of the heralded state to a single photon in a single spectral mode, versus the probability of heralding. Here we take the fidelity of the heralded state before any losses, which is thus an upper limit to the fidelity achievable in practice.

3.2.1. EFFECT OF FILTERING ON FIDELITY

We begin with a SPDC state with a certain distribution of spectral modes given by the Schmidt decomposition of the total state, where we assume the pump power is low enough to neglect time-ordering effects [33]. The state in terms of these broadband modes is [85]

$$|\psi\rangle = \bigotimes_{k=0}^{\infty} \operatorname{sech}(q_k) \sum_{n=0}^{\infty} \tanh^n(q_k) \left| n_k^{(s)}, n_k^{(i)} \right\rangle. \tag{3.1}$$

This means, for each spectral-temporal Schmidt mode k in the tensor product, there is a sum in photon number from 0 to ∞, with a thermal distribution. The squeezing parameters are defined as $q_k = B\lambda_k$, where B is an overall pump power factor, and λ_k are the eigenvalues of the Schmidt decomposition of the joint spectral amplitude. In practice the tensor product and sum need not be carried to infinity; we use a maximum of 20 spectral modes and 6 photons in simulation.

The spectral filter in the heralding (signal) arm rearranges the spectral modes. It suffices to take new (pseudo-) Schmidt decompositions of the joint spectral amplitudes transmitted and reflected by the filter [90, 91], without renormalizing. Then the state, with components now

labeled t for transmitted through the filter and r for reflected, is

$$|\psi\rangle = \bigotimes_{k_t=0}^{\infty} \mathrm{sech}(q_{k_t}) \sum_{n=0}^{\infty} \tanh^n(q_{k_t}) \left| n_{k_t}^{(s)}, n_{k_t}^{(i)} \right\rangle \bigotimes_{k_r=0}^{\infty} \mathrm{sech}(q_{k_r}) \sum_{n=0}^{\infty} \tanh^n(q_{k_r}) \left| n_{k_r}^{(s)}, n_{k_r}^{(i)} \right\rangle, \tag{3.2}$$

where now the squeezing parameters are $q_{k_t} = B_t \lambda_{k_t}$ and $q_{k_r} = B_r \lambda_{k_r}$, and B_r and B_t come from the relative intensities of the transmitted and reflected modes.

We can sort the terms according to photon number as

$$\begin{aligned} |\psi\rangle = \prod_{k_t} \mathrm{sech}\left(q_{k_t}\right) \Bigg(|0_t\rangle + \sum_{k_t} \tanh\left(q_{k_t}\right) \left| 1_{k_t}^{(s)}; 1_{k_t}^{(i)} \right\rangle + \\ + \sum_{k_t \le k_t'} \tanh\left(q_{k_t}\right) \tanh\left(q_{k_t'}\right) \left| 1_{k_t}^{(s)}, 1_{k_t'}^{(s)}; 1_{k_t}^{(i)}, 1_{k_t'}^{(i)} \right\rangle \dots \Bigg) \\ \otimes \prod_{k_r} \mathrm{sech}(q_{k_r}) \Bigg(|0_r\rangle + \sum_{k_r} \tanh\left(q_{k_r}\right) \left| 1_{k_r}^{(s)}; 1_{k_r}^{(i)} \right\rangle + \\ + \sum_{k_r \le k_r'} \tanh\left(q_{k_r}\right) \tanh\left(q_{k_r'}\right) \left| 1_{k_r}^{(s)}, 1_{k_r'}^{(s)}; 1_{k_r}^{(i)}, 1_{k_r'}^{(i)} \right\rangle \dots \Bigg), \end{aligned} \tag{3.3}$$

and continuing with higher number terms. Then we apply a detector (insensitive to the spectral-temporal modes) on the heralding (transmitted) mode, given by the heralding projector

$$\hat{\Pi}_t = c_0 |0\rangle\langle 0| + c_1 \sum_{k_t} \left| 1_{k_t} \right\rangle \left\langle 1_{k_t} \right| + c_2 \sum_{k_t \le k_t'} \left| 1_{k_t}, 1_{k_t'} \right\rangle \left\langle 1_{k_t}, 1_{k_t'} \right| + \dots, \tag{3.4}$$

where $c_{n_t} = 1 - (1-\eta_t)^{n_t}$ is the click probability given n_t photons for detection efficiency η_t. The extended heralding (reflected mode) projector is then $\hat{\Pi}_r = \hat{1} - \hat{\Pi}_t$. This is equivalent to $\hat{\Pi}_t$, with the detection probabilities c_{n_t} replaced by the probabilities of no click, $c_{n_r} = (1-\eta_r)^{n_r}$. Dark counts can be added to either detector with a constant term in the c_n.

Projecting the transmitted and reflected modes with their respective heralding and extended

heralding detectors returns the (normalized) heralded signal state

$$\begin{aligned}\rho_s = \frac{\prod_{k_t}\operatorname{sech}^2(q_{k_t})}{p_{\text{herald}}}\Bigg(& c_{0_t}\left|0_t\right\rangle\left\langle 0_t\right| + c_{1_t}\sum_{k_t}\tanh^2(q_{k_t})\left|1_{k_t}\right\rangle\left\langle 1_{k_t}\right| \\ &+ c_{2_t}\sum_{k_t\le k_t'}\tanh^2(q_{k_t})\tanh^2(q_{k_t'})\left|1_{k_t},1_{k_t'}\right\rangle\left\langle 1_{k_t},1_{k_t'}\right| + \dots\Bigg) \\ \otimes\frac{\prod_{k_r}\operatorname{sech}^2(q_{k_r})}{p_{\text{ext}}}\Bigg(& c_{0_r}\left|0_r\right\rangle\left\langle 0_r\right| + c_{1_r}\sum_{k_r}\tanh^2(q_{k_r})\left|1_{k_r}\right\rangle\left\langle 1_{k_r}\right| \\ &+ c_{2_r}\sum_{k_r\le k_r'}\tanh^2(q_{k_r})\tanh^2(q_{k_r'})\left|1_{k_r},1_{k_r'}\right\rangle\left\langle 1_{k_r},1_{k_r'}\right| + \dots\Bigg).\end{aligned} \tag{3.5}$$

The probabilities of heralding and extended heralding (i.e. getting a click in the transmitted arm, and *no* click in the reflected arm, respectively) are

$$\begin{aligned}p_{\text{herald}} = \prod_{k_t}\operatorname{sech}^2(q_{k_t})\Bigg(& c_{0_t} + c_{1_t}\sum_{k_t}\tanh^2(q_{k_t}) \\ &+ c_{2_t}\sum_{k_t\le k_t'}\tanh^2(q_{k_t})\tanh^2(q_{k_t'}) + \dots\Bigg)\end{aligned} \tag{3.6}$$

and

$$\begin{aligned}p_{\text{ext}} = \prod_{k_r}\operatorname{sech}^2(q_{k_r})\Bigg(& c_{0_r} + c_{1_r}\sum_{k_r}\tanh^2(q_{k_r}) \\ &+ c_{2_r}\sum_{k_r\le k_r'}\tanh^2(q_{k_r})\tanh^2(q_{k_r'}) + \dots\Bigg).\end{aligned} \tag{3.7}$$

Normally, we herald the presence of a signal photon by a successful detection event at the transmission port of the filter in the idler arm, disregarding the state of the reflected port. Extended heralding, i.e. the knowledge of whether a photon was present in the reflected port of the filter or not, gives us a more complete picture, and the combination of the two is what will give us an advantage. If our goal is to prepare *single* photons, then extended heralding will give us the necessary information to reject what would have otherwise been false positives.

Finally, the fidelity of the heralded state to a single photon in the first spectral mode and vacuum in all other modes is

$$\begin{aligned}F &= \left\langle 1_{0_t}\right| \otimes \left\langle 0_r\right| \rho \left|1_{0_t}\right\rangle \otimes \left|0_r\right\rangle \\ &= \frac{\prod_{k_t}\operatorname{sech}^2(q_{k_t})}{p_{\text{herald}}}\frac{\prod_{k_r}\operatorname{sech}^2(q_{k_r})}{p_{\text{ext}}} c_{1_t} c_{0_r}\tanh^2(q_{0_t}).\end{aligned} \tag{3.8}$$

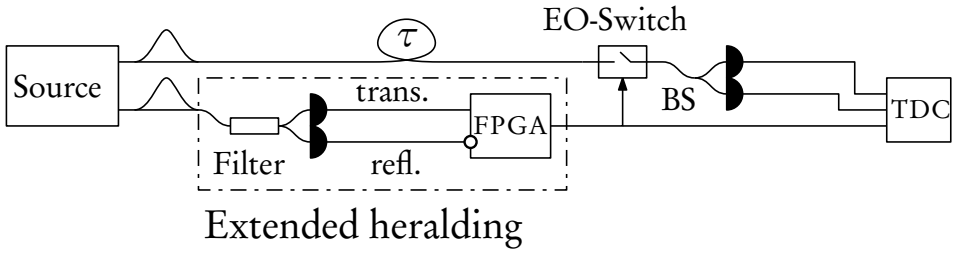

Figure 3.1.: Representation of the proposed scheme. Light coming from both transmission and reflection port of a frequency filter is analyzed by fast electronics (FPGA). The FPGA closes an electro-optic switch when a photon is present only in the transmission port. The statistics of the prepared state is then analyzed with a Time-to-Digital Converter (TDC).

This is the fidelity of the heralded single photon before it is subjected to losses, upper bounding the possible performance of the source. This fidelity is plotted in Figure 3.2, which shows the progression from an unfiltered, spectrally multimode state (with JSI matching our experiment), to filtered but contaminated with multiphoton events, to finally a high-fidelity state. An ideal photon source has simultaneously high heralding probability and fidelity, but without multiplexing heralded single photon sources are limited to the yellow region. Of course, one still wants to operate the sources as close to the upper right corner as possible. Here the unfiltered state shows consistently low fidelity, which can be increased by filtering, in our case to 50 GHz bandwidth. Without losses, the extended heralding case maintains high fidelity for significantly higher heralding probability than the standard filtered case, approaching the theoretical limit much more closely, as shown in the right plot of Figure 3.2. We can see that by using the proposed scheme, we can obtain a source of equal performance in terms of fidelity, but with four times the heralding rate, if we use a fidelity of $F = 0.92$ as our target. This maximal improvement depends of course on the actual spectral characteristics of the source at hand.

It is unfortunately not possible to access this fidelity experimentally due to the difficulty of projecting on the vacuum and single photons in single spectral modes with realistic losses. The source quality can still be accessed, however, via the spectral purity P and heralded $g_h^{(2)}(0)$. Fidelity $F = 1$ corresponds to $P = 1$ and $g_h^{(2)}(0) = 0$. Here the purity is controlled by spectral filtering, which increases the $g_h^{(2)}(0)$ from pollution from other spectral modes, which is subsequently reduced by heralding plus feed-forward.

We now make a few approximations to express the fidelity (3.8) in terms of these experimentally accessible quantities. First, we assume all q_{k_t} and q_{k_r} are small such that $\tanh(q_k) \approx q_k$ and $\mathrm{sech}(q_k) \approx 1$. Then we neglect filtering (dropping the subscripts t), resulting in a fidelity

$$F \approx \frac{c_1 q_0^2}{p_{\text{herald}}}. \tag{3.9}$$

We then assume low overall generation probability and no dark counts, such that we can truncate

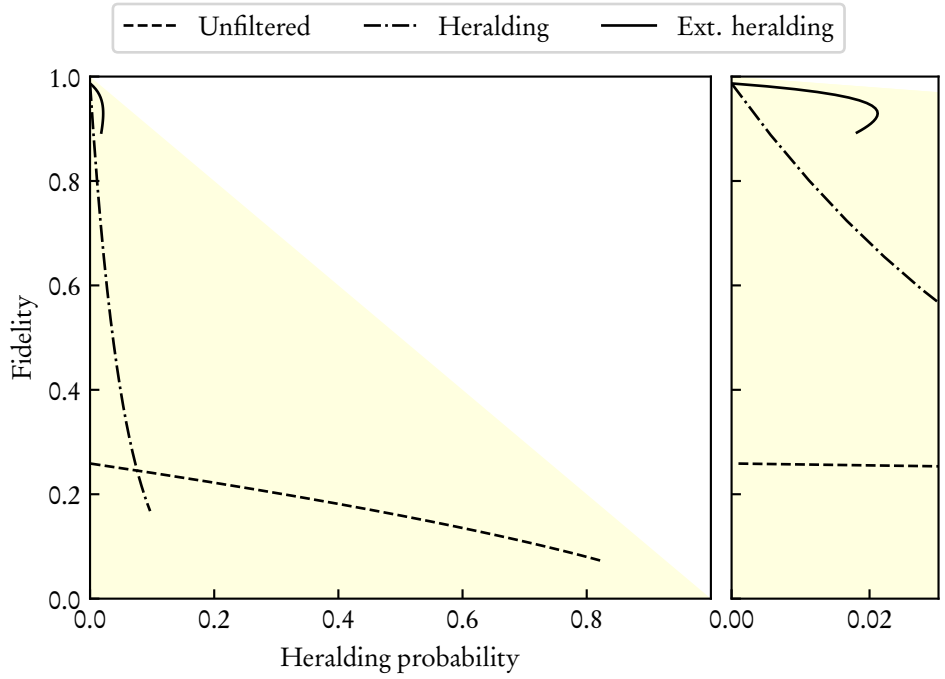

Figure 3.2.: Left plot: theoretical fidelity versus heralding probability, with and without spectral filtering and extended heralding. Each curve is produced by varying the initial (before filtering) mean photon number over $[10^{-2}, 2]$. After filtering and extended heralding, the state reaches and remains in the high-fidelity region for a range of pump powers. Right plot: Detail of the aforementioned range in which the fidelity is consistently higher than both unfiltered and heralded case.

p_{herald} to second order, giving

$$p_{\text{herald}} \approx c_1 \sum_k (q_k)^2 + c_2 \sum_{k \le k'} (q_k)^2 (q_{k'})^2. \tag{3.10}$$

We expand the fidelity in a Taylor series about 0 in the second term of p_{herald} (i.e. $1/(a+x) \approx 1/a - x/a^2$), giving

$$F \approx \frac{q_0^2}{\sum_k (q_k)^2} \left(1 - \frac{c_2 \sum_{k \le k'} (q_k)^2 (q_{k'})^2}{c_1 \sum_k (q_k)^2} \right) \tag{3.11}$$

The spectral purity is given in [92] as

$$P \approx \frac{\sum_k (q_k)^4}{(\sum_k (q_k)^2)^2} \approx \frac{q_0^4}{(\sum_k (q_k)^2)^2}, \tag{3.12}$$

where we assumed that the first Schmidt mode dominates, i.e. $q_0^4 \gg q_{k>0}^4$. Then we can identify

this purity with the square of the first term in our approximate fidelity, resulting in

$$F \approx \sqrt{P}\left(1-\frac{c_2\sum_{k\leq k'}(q_k)^2(q_{k'})^2}{c_1\sum_k(q_k)^2}\right). \tag{3.13}$$

We similarly approximate and truncate the heralded state ((3.5)) to give

$$\rho_s \approx \frac{1}{p_{\text{herald}}}\left(c_1\sum_k(q_k)^2\,|1_k\rangle\langle 1_k| + c_2\sum_{k\leq k'}(q_k)^2(q_{k'})^2\,|1_k,1_{k'}\rangle\langle 1_k,1_{k'}|\right). \tag{3.14}$$

The heralded $g_h^{(2)}(0)$ is given for multimode states [92] with broadband mode operators A_k by

$$g_h^{(2)}(0) = \frac{\left\langle\left(\sum_{j,m}A_j^\dagger A_m^\dagger A_j A_m\right)\right\rangle}{\left\langle\sum_j A_j^\dagger A_j\right\rangle^2}, \tag{3.15}$$

which when substituting ρ_s results in

$$g_h^{(2)}(0) \approx \frac{2c_2 p_{\text{herald}}\sum_{k\leq k'}(q_k)^2(q_{k'})^2}{(c_1\sum_k(q_k)^2)^2}. \tag{3.16}$$

We then keep p_{herald} only to first order, allowing to identify the second term of our approximate fidelity with $g_h^{(2)}(0)/2$, resulting in

$$F \approx \sqrt{P}\left(1-\frac{g_h^{(2)}(0)}{2}\right). \tag{3.17}$$

For the filtered case, with and without extended heralding, the derivation is similar, and it shows that the same result as (3.17) apply. Again, we assume all q_{k_t} and q_{k_r} are small such that $\tanh(q_k)\approx q_k$ and $\operatorname{sech}(q_k)\approx 1$. Then the fidelity is

$$F \approx \frac{c_{1_t}c_{0_r}q_{0_t}^2}{p_{\text{herald}}p_{\text{ext}}}. \tag{3.18}$$

We then assume low overall generation probability and no dark counts, such that we can truncate p_{herald} to second order, giving

$$p_{\text{herald}} \approx c_{1_t}\sum_{k_t}(q_{k_t})^2 + c_{2_t}\sum_{k_t\leq k_t'}(q_{k_t})^2(q_{k_t'})^2, \tag{3.19}$$

and p_{ext} to first order as

$$p_{\text{ext}} \approx c_{0_r} + c_{1_r}\sum_{k_r}(q_{k_r})^2. \tag{3.20}$$

We also neglect the third-order term in the product $p_{\text{herald}}p_{\text{ext}}$, giving fidelity

$$F \approx c_{1_t} c_{0_r} q_{0_t}^2 \left(c_{1_t} c_{0_r} \sum_{k_t} (q_{k_t})^2 + c_{2_t} c_{0_r} \sum_{k_t \le k_t'} (q_{k_t})^2 (q_{k_t'})^2 + c_{1_t} c_{1_r} \sum_{k_t} (q_{k_t})^2 \sum_{k_r} (q_{k_r})^2 \right)^{-1}. \tag{3.21}$$

We then expand the fidelity in a Taylor series about 0 in the second two terms of the denominator $(1/(a+x) \approx 1/a - x/a^2)$, giving

$$F \approx \frac{q_0^2}{\sum_{k_t} (q_{k_t})^2} \left(1 - \frac{c_{2_t} c_{0_r} \sum_{k_t \le k_t'} (q_{k_t})^2 (q_{k_t'})^2}{c_{1_t} c_{0_r} \sum_{k_t} (q_{k_t})^2} - \frac{c_{1_t} c_{1_r} \sum_{k_t} (q_{k_t})^2 \sum_{k_r} (q_{k_r})^2}{c_{1_t} c_{0_r} \sum_{k_t} (q_{k_t})^2} \right) \tag{3.22}$$

The spectral purity is the same as before [92]

$$P \approx \frac{\sum_{k_t} (q_{k_t})^4}{\left(\sum_{k_t} (q_{k_t})^2 \right)^2} \approx \frac{q_0^4}{\left(\sum_{k_t} (q_{k_t})^2 \right)^2}. \tag{3.23}$$

We now include the reflected modes in the truncated heralded state ((3.5)) to give

$$\begin{aligned} \rho_s \approx \frac{1}{p_{\text{herald}}} & \left(c_{1_t} \sum_{k_t} (q_{k_t})^2 \left| 1_{k_t} \right\rangle \left\langle 1_{k_t} \right| + c_{2_t} \sum_{k_t \le k_t'} (q_{k_t})^2 (q_{k_t'})^2 \left| 1_{k_t}, 1_{k_t'} \right\rangle \left\langle 1_{k_r}, 1_{k_r'} \right| \right) \\ \otimes \frac{1}{p_{\text{ext}}} & \left(c_{0_r} \left| 0 \right\rangle \left\langle 0 \right| + c_{1_r} \sum_{k_r} (q_{k_r})^2 \left| 1_{k_r} \right\rangle \left\langle 1_{k_r} \right| \right). \end{aligned} \tag{3.24}$$

The heralded $g_h^{(2)}(0)$ is given for multimode states [92] with broadband mode operators A_k by

$$g_h^{(2)}(0) = \frac{\left\langle \left(\sum_{j,m} A_j^\dagger A_m^\dagger A_j A_m \right) \right\rangle}{\left\langle \sum_j A_k^\dagger A \right\rangle^2}. \tag{3.25}$$

Substituting ρ_s and neglecting the reflected modes in the denominator results in

$$g_h^{(2)}(0) \approx \frac{2 c_{2_t} c_{0_r} p_{\text{herald}} \sum_{k_t \le k_t'} \left(q_{k_t} \right)^2 (q_{k_t'})^2}{\left(c_{1_t} c_{0_r} \sum_{k_t} (q_{k_t})^2 \right)^2} + \frac{2 c_{1_t} c_{1_r} p_{\text{herald}} \sum_{k_t} (q_{k_t})^2 \sum_{k_r} (q_{k_r})^2}{\left(c_{1_t} c_{0_r} \sum_{k_t} (q_{k_t})^2 \right)^2}. \tag{3.26}$$

The factor 2 comes from the annihilation operators themselves when they act on the same mode (i.e. $j = m = k_t = k_t'$), and from the two equivalent arrangements of annihilation operators when they act on different modes (e.g. $j = k_t$, $m = k_r$; or $j = k_r$, $m = k_t$). We then keep p_{herald} only to first order and assume negligible dark counts such that $c_{0_r} \to 1$, allowing to identify the second term of our approximate fidelity with $g_h^{(2)}(0)/2$, resulting in the same fidelity as without filtering, namely

$$F \approx \sqrt{P} \left(1 - \frac{g_h^{(2)}(0)}{2} \right). \tag{3.27}$$

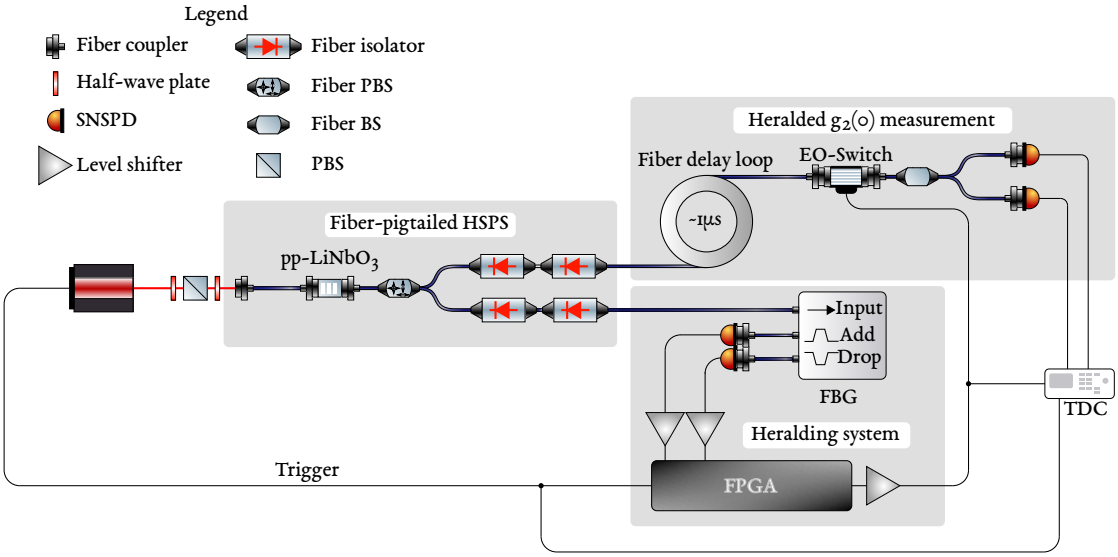

Figure 3.3.: Experimental setup. Black thin lines represent electrical connections, while thick blue lines are single-mode fibers. The electro-optic switch (EO-Switch) is a 2×2 device whose unused ports are not depicted. The Time-To-Digital converter is connected to a computer for data storage (not depicted).

3.3. Experimental setup

The experimental setup is shown in Figure 3.3. We use a type-II SPDC source based on a periodically-poled titanium-indiffused lithium niobate waveguide. The source is fiber-pigtailed and is engineered to produce single photon pairs at 1560 nm when pumped at 780 nm and kept at room temperature [13]. However, in this experiment the source is kept at around 50 °C, to shift the degeneracy point of the source into a range that fits the window of the fiber Bragg-Grating (FBG) filter used for heralding.

A pulsed laser system (*Spectra Physics Tsunami*) with a 2 ps bandwidth and centered at 777.24 nm with a repetition rate of 500 kHz pumps the SPDC and acts as the system clock. In order to control power and polarization of the pump, a half-wave plate, a polarizing beam-splitter, and a second half-wave plate, are placed just before light is coupled into the SPDC source. The pump is then coupled into a polarization maintaining fiber directly pigtailed to one of the end facets of the lithium niobate chip. Photon pairs are then collected at the output end facet by another polarization maintaining fiber. The output fiber is fusion-spliced to a fiber polarizing beam-splitter to separate the two outputs of the source (typically called “signal” and “idler”). The outputs of the fiber PBS are then also spliced to two fiber isolators per arm to suppress the residual pump light. In our case, the signal arm is the one being filtered and the idler is the arm being analyzed.

The signal arm is connected to an FBG filter (*AOS Manual FBG*) centered at 1554.5 nm and with 0.25 nm bandwidth. The two outputs of the filter correspond to the selected portion of the spectrum we want to use for heralding (“add” or transmitted) and the extended-heralding

one ("drop" or reflected).

To implement the schemes described above, we monitor both outputs of the filter and apply two different heralding criteria. In the first case, which we will use as benchmark and label simply "heralding", the heralding signal is taken to be a click in the transmitted arm of the filter. In the second case, labeled extended heralding, the heralding signal is a combination of two events: a click in the transmitted arm and no clicks in the reflected arm. Additionally, in this second case the extended heralding signal is used to close an electro-optic switch. This means that we are physically removing unheralded photons from the system instead of simply discarding such events during data-analysis, a feature which proves crucial in light sensitive applications.

In both cases, the signal arm photons are detected with a superconducting nanowire single-photon detector (SNSPD, *PhotonSpot*). The generated outputs are amplified to TTL levels and redirected to the FPGA (*Xilinx Spartan 6*) which produces the final heralding signal, depending on the condition set. This signal is then fed to a TDC (*AIT TTM8000*) for analysis.

The idler arm is routed to a fiber loop which introduces a delay of approximately 1 µs. This gives enough time for the electronics to generate the appropriate heralding signal as described above. This then is used to close an electro-optic switch, which is normally open (i.e. blocking transmission of the light). The output of the switch is then coupled to a non-polarizing beam-splitter, whose outputs are finally connected to two SNSPDs. Their outputs are analyzed by the TDC, which registers the timestamps of each detector click and saves them onto a computer.

3.4. Analysis and discussion

To characterize the efficacy of extended heralding in the presence of realistic spectral mode distributions, losses, and higher-order photon states, we performed numerical simulations using QuTiP [93]. We calculate the two-photon joint spectral amplitude of our photon pair source, perform a Schmidt decomposition to find the relative strengths of the involved squeezers, then normalize the overall pump power to give the appropriate total mean photon pair number. Next idealized (square, lossless) filters are applied to the heralding arm, and detector operations are applied to the transmitted and reflected arms, and we calculate the fidelity from (3.8). We also analyze the spectral purity and photon statistics via the $g_h^{(2)}(0)$ in order to compare with experiment. Finally we introduce the *heralded single-photon fitness* F_{HS}, so named because it captures two important aspects of a heralded single photon source: the presence of one photon in a single spectral mode upon heralding, and the absence of photons without heralding. The former is improved here by extended heralding, and the latter by using feed-forward to control a physical switch on the heralded mode. The contributions of these terms are weighted by their likelihood. We define the heralded single-photon fitness as

$$\begin{aligned} F_{HS} &= p_{\text{herald}} F + (1 - p_{\text{herald}}) P_{\text{noclick}} \\ &\approx p_{\text{herald}} \sqrt{P} \left(1 - \frac{g_h^{(2)}(0)}{2} \right) + (1 - p_{\text{herald}}) P_{\text{noclick}} \end{aligned} \tag{3.28}$$

where P_{noclick} is the probability of getting no detection in the heralded mode given that there was no heralding signal. This probability is also scaled to take into account losses in the setup, i.e.

$$P_{\text{noclick}} = 1 - \frac{P_{\text{click}}}{\eta} \tag{3.29}$$

where η is the heralded photon's Klyshko efficiency, which gives the probability of producing no photon inside the source.

As stated before, filtering is the simplest way to improve the purity of a source with a correlated spectrum. This comes at a cost, namely a reduction in the generation rate of single-photons. To counteract this effect, the natural answer would be to increase the pump power used, but if we look at Figure 3.2, increasing the pump power means moving from left to right along the curves. That means that trying to recover the generation rate leads to lower fidelities, so we need to find a compromise.

To show this behavior, we record the $g_h^{(2)}(0)$ value at different power levels when using the heralding signal from the transmitted FBG port. We show the data as a function of heralding probability as only the photons which have been heralded are usable. As summarized by Figure 3.4, the $g_h^{(2)}(0)$ captures the undesired increase of the multiphoton-component contribution as the heralding probability increases. The $g_h^{(2)}(0)$ value is calculated according to

$$g_h^{(2)}(0) = \frac{C}{S_1 S_2} H, \tag{3.30}$$

where C is the number of heralded coincidences at the end of the non-polarizing beam-splitter, S_1 and S_2 are the heralded counts at each output, respectively, and H is the number of heralding signals in the experiment.

If we now take into account the reflected port of the FBG filter to generate the extended heralding signal, we can see that, for the same value of heralding probability, we have decreased the $g_h^{(2)}(0)$ value, indicating that we effectively mitigated the spurious contributions of multiple pairs. Additionally, the data is in good agreement with our theoretical model, which allows us to extrapolate the best possible improvement when sourcing components with lower losses.

The data in Figure 3.4 show the measured values of the $g_h^{(2)}(0)$ and the fidelity, with the respective theoretical models. We can see that in each case theory and experiment are in good agreement, particularly for the solid lines, which directly implement in simulation the approximations made in the approximate fidelity (3.17). An additional consideration is that this scheme is more effective the harder the source is pumped, e.g. reaching a maximum improvement in $g_h^{(2)}(0)$ of 21%, or for the same $g_h^{(2)}(0)$, an improvement in the count rate of 1.2 times.

The performance of extended heralding is mainly limited by the losses in the experimental setup, as can be seen in the significant difference in the simulated curves with and without losses. Fiber-to-fiber connections, the FBG itself and the network connecting the source to the detection system all amount to an estimated 30% total transmission. Sourcing better components could increase the improvement obtained with this scheme over simple heralding to a more than 80% reduction in the $g_h^{(2)}(0)$.

In the previous two measurements, it is not necessary to implement feed-forward, as the same result can be achieved with post-selection. However, active gating is of importance when the total light flux reaching the experimental setup must be kept to a minimum, as it allows only correctly heralded photons to pass. The source fitness parameter F_{HS} as introduced in (3.28) directly captures this improvement, which cannot be achieved with post-selection, and gives us a quantitative measure of the noise reduction achieved thanks to this scheme. In contrast to the improvement in fidelity, here the increase in photon fitness is more significant for higher losses, as more losses in the heralding arm mean more unheralded events make it to the detectors without feed-forward. As seen in Figure 3.5, the source fitness after extended heralding and feed-forward is nearly perfect, with a maximum improvement of 53%.

Another parameter used to characterize active sources is the output noise factor (ONF) [86]. Given a heralding probability of 0.0037, optical switch on-time of 200 ns and optical switch extinction ratio of 20 dB, we calculated a ONF of (2.4 ± 2.0) %.

3.5. Conclusion

We have introduced and implemented a scheme called extended heralding, aimed at improving the standard filtering used to increase the spectral purity of photon pair sources with a correlated joint spectrum. A significant improvement is found when compared to a passive filter, especially when care is taken to minimize losses throughout the setup. This scheme is also easy to implement on top of an existing HSPS, requiring no modification of the existing setup. Finally, we have demonstrated a significant reduction in unwanted incident light through the use of active feed-forward, which is important in practical light-sensitive scenarios.

As much as this solution does improve the performance of a HSPS, there is only so much one can do. In the next part of this work, we will introduce an alternative set of tools to tackle the problem of deterministically generating pure single photon from SPDC sources.

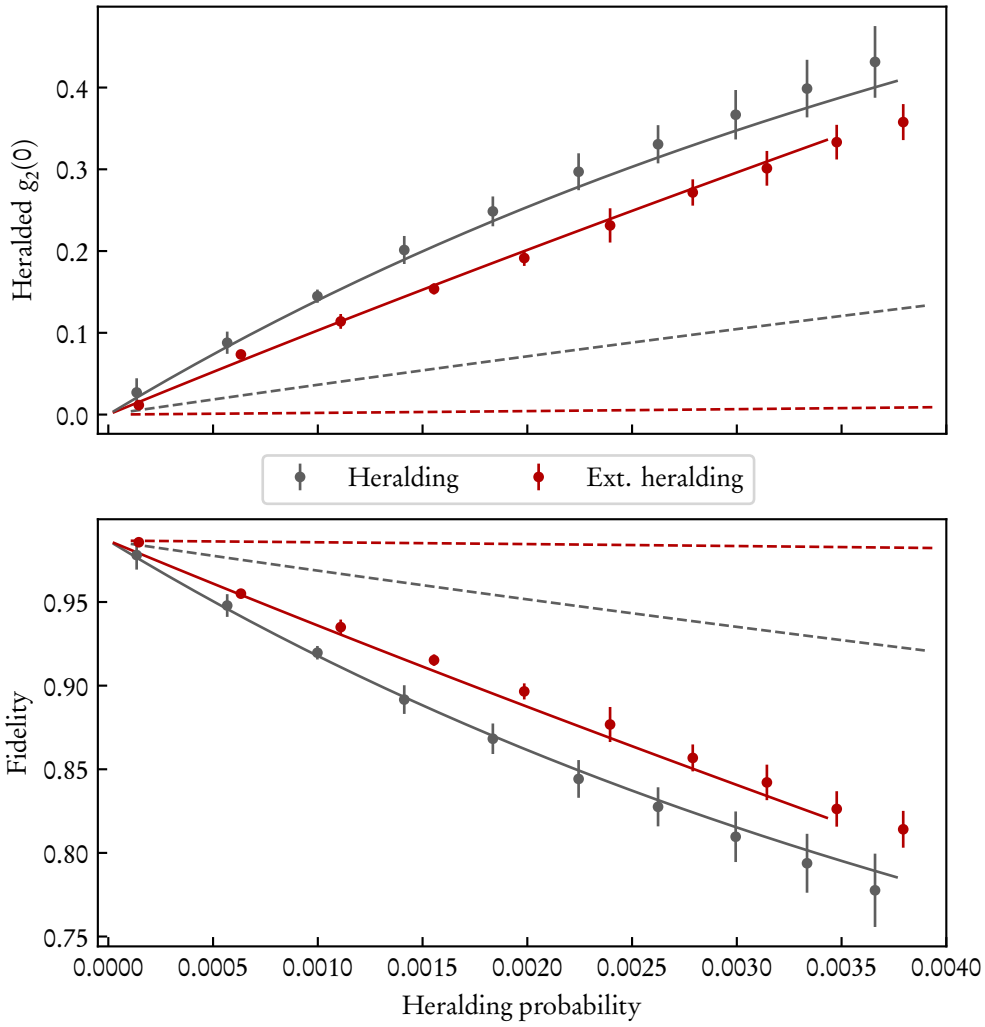

Figure 3.4.: Effect of normal and extended heralding. The two figures, top and bottom, represent equations (3.30) and (3.17), respectively. Error bars are statistical errors with 1-sigma confidence interval calculated over ten repetitions of the experiment, each with an integration time of 120 seconds. Solid lines represent our theoretical models, taking into account the experimental parameters. Dashed lines represent the same model in the case of lossless components throughout the setup.

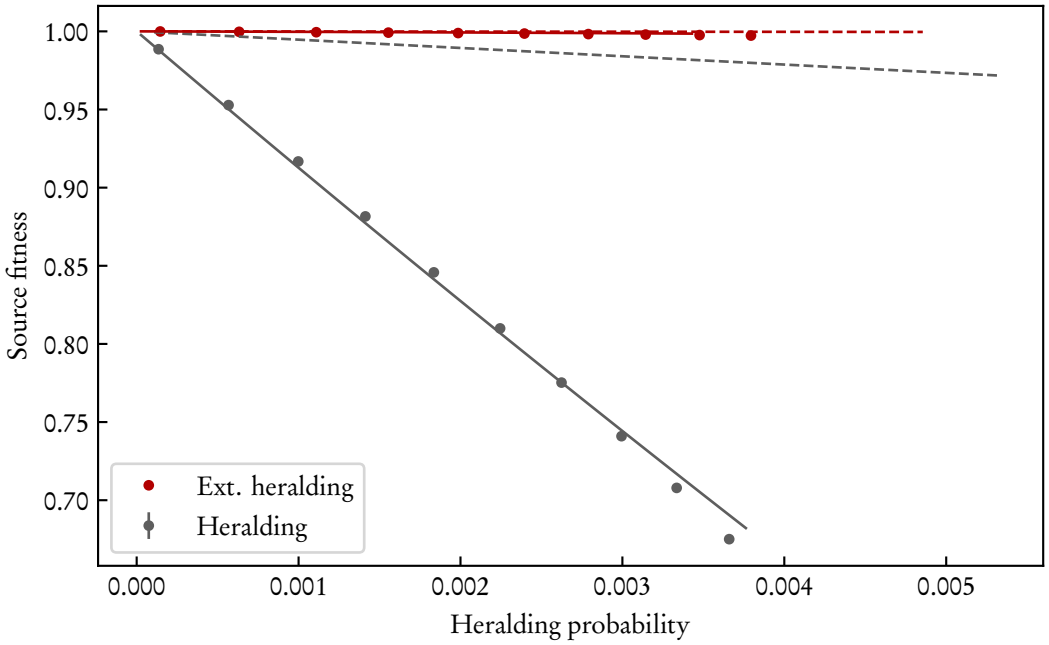

Figure 3.5.: Source fitness as single photon source (Equation 3.28). As above, solid lines represent our theoretical models, and dashed lines represent the same model with lossless components.

Part II.

All sources for one photon

4. MULTIPLEXING PHOTONS: A WORKAROUND FOR HSPSS' LIMITATIONS

We have discussed in the last part how HSPSs can be used in conjunction with other technologies and how we can avoid some inconveniences when tailoring these sources to our needs. As much as we would like to improve things, there is only so much we can do. Some limitations of these type of sources can't simply be ignored or disregarded and we must either face the music or we need to think outside the box.

In this chapter, we will discuss the concept of *source multiplexing*, and how it will help us against the probabilistic nature of SPDC sources. But first we need to understand *why* we need multiplexing and how it relates with the concepts laid out in the first chapter of this work.

4.1. THE IDEAL HSPS IS NOT NEARLY ENOUGH

Figure 4.1 highlights the difference in photon number statistics between a correlated and uncorrelated source. It is clear that we are fighting an uphill battle when we say that we want to generate single photons with SPDC sources, because our objective is to generate a *single* photon, not *at least* one photon.

Let's have a look at the performance of one of the simplest sources we can think of: a single-mode HSPS. We defined in (1.38) the state generated by such a source as

$$|\psi_{\text{SPDC}}\rangle = \sqrt{1-|\lambda|^2}\sum_{n=0}^{\infty}\lambda^n\,|n,n\rangle\,. \tag{4.1}$$

We need to define *how* we are going to herald the photons generated by this source, so we need to define how our detectors act on the state (4.1). We define in general a set of POVMs

$$\hat{\Pi}(n) = \sum_{N=n}^{\infty} p_d(n|N)\,|N\rangle\langle N|\,, \tag{4.2}$$

which define a measurement of the outcome n, and where $p_d(n|N)$ is the conditional probability of detecting n photons when N are actually present at the input of the detector. Based on this, we can define two types of detectors. We have already encountered one, the "bucket" or "click" detector, in chapter 2 and chapter 3, which has only two outcomes, "click" or "no-click". We assume that the efficiency of such detector is η_d, i.e. a single photon has a probability η_d of triggering the detector, and we obtain

$$p_B(\text{“no-click”}|N) = (1-\eta_d)^N \tag{4.3}$$

$$p_B(\text{“click”}|N) = 1 - p_B(\text{“no-click”}|N) \tag{4.4}$$

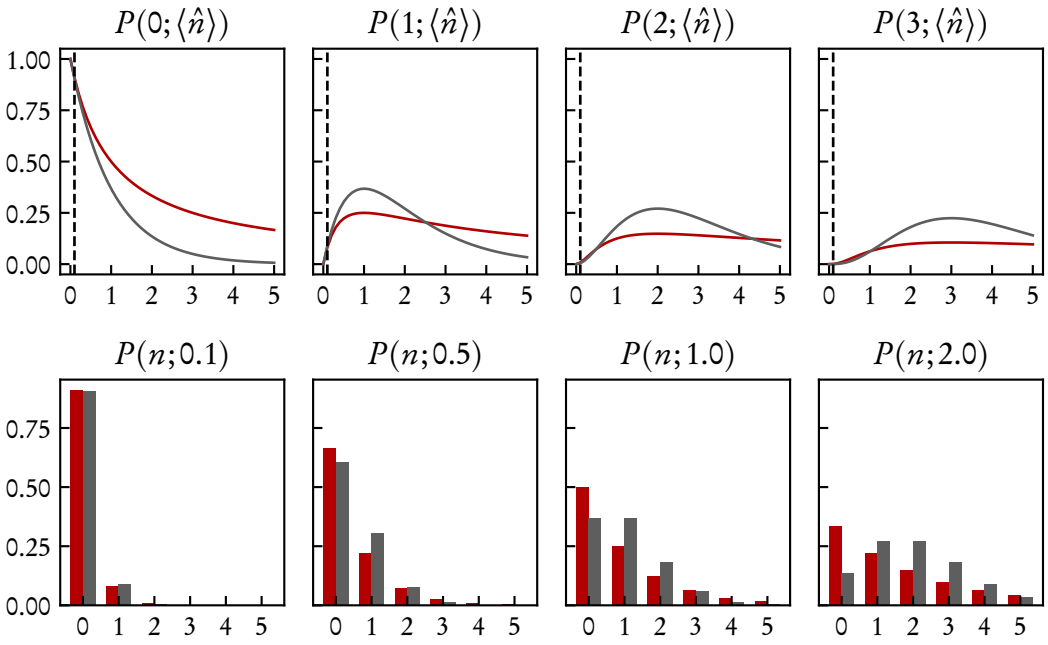

Figure 4.1.: Photon number statistics overview for both correlated (gray) and uncorrelated (red) sources. Top row: probability of generating $n \in \{0,1,2,3\}$ photons as a function of the mean photon number per pulse. The dashed lines mark the $\langle\hat{n}\rangle = 0.1$ level under which HSPSs are usually operated. Bottom row: probability of generating n photons assuming a fixed mean photon number per pump pulse.

where the suffix B indicates a bucket detector.

On the other hand, if we are lucky enough to have a photon-number resolving detector (PNRD), using basic probability theory we can calculate what's the probability of detecting n photons given that N where present as

$$p_R(n|N) = \binom{N}{n} \eta_d^n (1-\eta_d)^{N-n}, \tag{4.5}$$

where we have assumed that our PNRD has an efficiency η_d of detecting a single photon. The suffix R stands for "resolving".

Having a description for our detectors, we can now ask two questions: what is the probability of heralding the presence of a single photon and what does the heralded state look like. A heralding event is of course one where we detect a single photon in one of the two modes of our state in (4.1). The heralding probability is

$$\begin{aligned} p_H = \langle \psi_{\text{SPDC}} | \Pi(1) | \psi_{\text{SPDC}} \rangle &= \left(1-\lambda^2\right) \sum_{n,n',N}^{\infty} \lambda^{n'} \lambda^n p_d(1|N) \left\langle n', n' \right| |N\rangle\langle N| \, |n, n\rangle \\ &= \left(1-\lambda^2\right) \sum_{n,n',N}^{\infty} \lambda^{n'} \lambda^n p_d(1|N) \delta_{n,n'} \delta_{n',N} \delta_{N,n} \\ &= \left(1-\lambda^2\right) \sum_{n=1}^{\infty} \lambda^{2n} p_d(1|n) \end{aligned} \tag{4.6}$$

where we have assumed that λ is real [19]. The reduced heralded state is found by tracing over the heralding sub-space, i.e.

$$\hat{\rho}_H = \frac{\text{Tr}\{\Pi(1)\hat{\rho}_{\text{SPDC}}\}}{p_H} = \frac{\sum_n^{\infty} \lambda^{2n} p_d(1|n) |n\rangle\langle n|}{\sum_n^{\infty} \lambda^{2n} p_d(1|n)}. \tag{4.7}$$

All that's left is to calculate the fidelity to the single photon Fock state, defined as

$$F = \langle 1 | \hat{\rho}_H | 1 \rangle = \frac{\lambda^2 p_d(1|1)}{\sum_n^{\infty} \lambda^{2n} p_d(1|n)}. \tag{4.8}$$

With equations (4.6) and (4.8) we are now able to shed some light on the problem of wanting both a fast and deterministic single photon source. For the case of a multimode source, we refer the reader to [19], from which this analysis is inspired. Looking at Figure 4.2, it's clear that HSPSs are not fit to be pure, deterministic, single-photon source, because in that case, we should be able to reach the top right corner of the plots of the first row, where both the heralding probability and the fidelity are 1. This is not a technical limitation. Even with perfect ($\eta_d = 1$) number-resolving single photon detectors, the intrinsic nature of these sources simply does not allow us to reach our goal. There is hope though, as we stated at the beginning of this chapter. Clearly *one* source is not enough for our needs, but it turns out that combining multiple sources into a single one does get rid of the limitation that we have just described [18]. This is what we called source multiplexing, and it's going to be focus of the rest of this chapter.

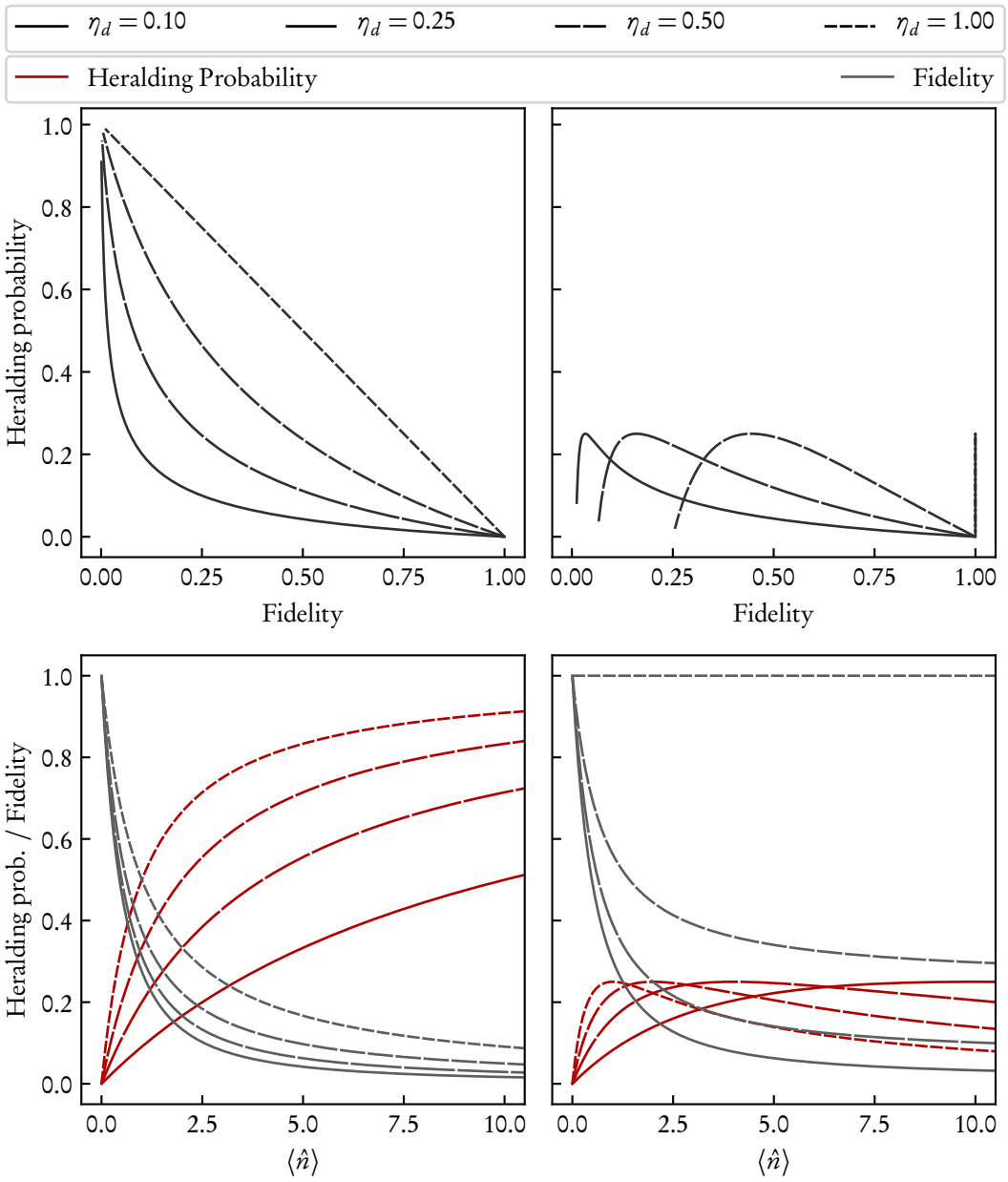

Figure 4.2.: Top row: comparison between the fidelity to single-photon Fock state of a HSPS and its heralding probability. These are parametric plots in the mean photon number. Plotting the fidelity against the heralding probability serves to underline the inherent problems related to wanting to maximize one or the other. Our goal is to reach the top-right corner of these plots, but the intrinsic behavior of these sources hinders us. Bottom row: functional dependence of the heralding probability and the fidelity on the average photon number. Left column: click detectors; right column: PNRDs.

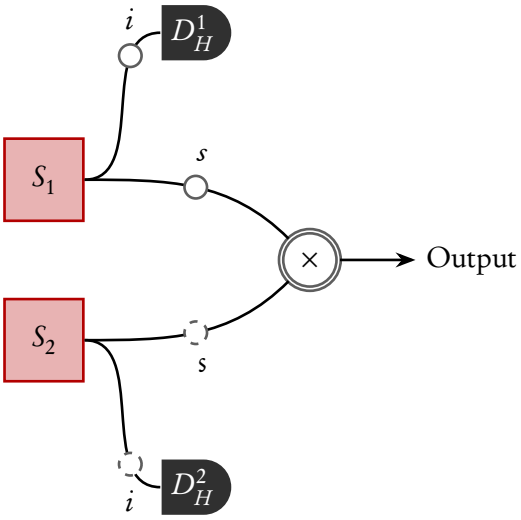

Figure 4.3.: Schematic representation of spatial multiplexing. Multiple identical sources are triggered all at the same time and their heralding (idler, i) outputs are all checked for photons. If one of the sources has effectively produced a photon, then that source's heralded signal (s) will be routed through the network to the output mode, ready to be further manipulated.

4.2. Spatial multiplexing

Multiplexing comes in different "varieties", depending on which degree of freedom in your system you are leveraging, each of which has its pros and cons. One of the most straightforward cases is *spatial* multiplexing.

The main idea is as follows: a single-mode perfect HSPS has a 25% chance that it will actually produce a single photon. If we put N together and we trigger them all at the same time, then the probability that *at least one* will produce a single photon will be higher than the single one, namely

$$p_{\text{MUX}} = 1-(1-p_s)^N, \tag{4.9}$$

where p_s is the probability of our source generating a single photon. We can estimate from this that we would "only" need 17 sources [19] to achieve >99% probability of producing a single photon. After we record a successful heralding event, we can then route the generated photon into a predefined spatial mode through a switching network triggered by some logic controller. We buffer each HSPS output signal with an optical delay so that the logic controller has enough time to set up the switching network accordingly.

This is of course in an ideal world, but we need to keep our feet down. Seventeen sources are not a small amount and each of them comes with associated hardware necessary to herald one photon of the pair and route the other one down to the output. Let's calculate what's the impact of losses in this type of setup. We will assume that all components involved are identical for simplicity. We will call η_i and η_s the collection efficiencies of the signal and idler arm, respectively (not accounting for detector losses), η_n the efficiency of the entire switching

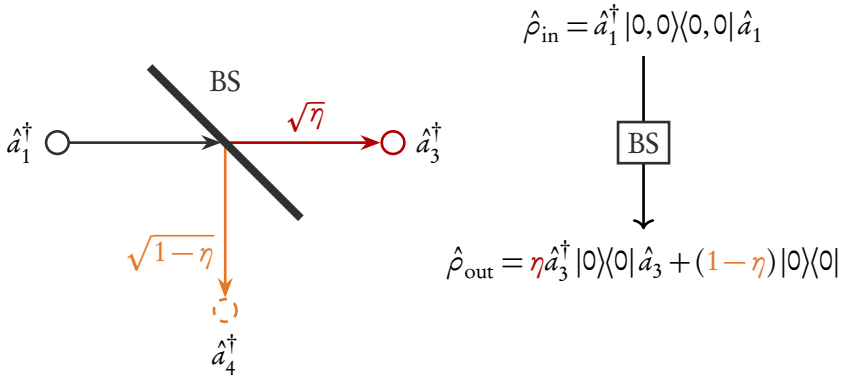

Figure 4.4.: Schematic representation of the loss model described in this chapter. Each photon has a certain probability η of being transmitted. We ignore the ones which get reflected (with probability $1-\eta$) and only care about mode 3 of the BS, regardless of the state of mode 4, thus having a mixed state as output.

network, η_d the efficiency of the detectors and η_ℓ the efficiency of the buffering optical loops.

If we want to multiplex N sources, then we need $S = \lceil \log_2(N) \rceil$ optical switches to route one of the sources' outputs to the main one. This is called multiplexing *depth* (i.e. how many switches the selected photon will go through) and it amounts to a total loss of

$$\eta_n = \eta_\ell \sigma^S \tag{4.10}$$

where σ is the efficiency of a single switch (including input and output routing elements, like mirrors or fibers).

What's the chance that we are actually going to detect a *heralded* single photon at the output? The emphasis on "heralded" is not put there at random: we are not interested in the overall probability of having some photon at the output, we want to be *sure* that there is going to be one (otherwise, why would we use HSPSs at all?). To answer this question we need three elements: the probability that we successfully herald a single photon; the probability that this is *actually* a single photon and not a multi-photon event which our detectors could not discriminate—which is the case for bucket detectors giving out false-positives even with perfect efficiency; and lastly the probability that this certified single photon does not get lost in the switching network. We follow the analysis of [94], with the difference that here we arrive at more general results. For simplicity, we disregard the role of dark counts in our analysis.

We will model a lossy component as a non-polarizing BS with transmission η followed by a perfect component (Figure 4.4). A BS with transmission η transforms its input modes $\hat{a}_1^\dagger, \hat{a}_2^\dagger$ into the outputs

$$\begin{aligned} \hat{a}_1^\dagger &= \sqrt{\eta}\hat{a}_3^\dagger + \sqrt{1-\eta}\hat{a}_4^\dagger \\ \hat{a}_2^\dagger &= \sqrt{1-\eta}\hat{a}_3^\dagger - \sqrt{\eta}\hat{a}_4^\dagger \end{aligned} \tag{4.11}$$

so any input Fock state can be rewritten in terms of the output states of the BS accordingly

$$|n,m\rangle = \frac{\left(\hat{a}_1^\dagger\right)^n}{\sqrt{n!}}\frac{\left(\hat{a}_2^\dagger\right)^m}{\sqrt{m!}}|0\rangle = \frac{\left(\sqrt{\eta}\hat{a}_3^\dagger + \sqrt{1-\eta}\hat{a}_4^\dagger\right)^n}{\sqrt{n!}}\frac{\left(\sqrt{1-\eta}\hat{a}_3^\dagger - \sqrt{\eta}\hat{a}_4^\dagger\right)^m}{\sqrt{m!}}|0\rangle\,. \tag{4.12}$$

As we did previously with the case of the perfect HSPS setup, we will deal with one or the other sub-system of our collective state, so it's more convenient to work in terms of density matrices. For this, we need to understand how the BS transformation (4.12) affects each matrix element $|n\rangle\langle n'|$ of the Fock space. By applying the transformation, we obtain

$$|n\rangle\langle n'| = \sum_k^n \sum_{k'=0}^{n'} \gamma_{kk'}^{nn'}(\eta)\,|n-k,k\rangle\langle n'-k',k'|\,, \tag{4.13}$$

in which the second mode in each ket (i.e. k and k') represents the "loss" mode and where we defined

$$\gamma_{kk'}^{nn'}(\eta) = B_k^n B_{k'}^{n'} \frac{\sqrt{(n-k)!k!}\sqrt{(n'-k')!k'!}}{\sqrt{n!}\sqrt{n'!}}\sqrt{\eta}^{n+n'-k-k'}\sqrt{1-\eta}^{k+k'}\,, \tag{4.14}$$

B_k^n being the binomial coefficient.

The density matrix of our SPDC state reads

$$\begin{aligned}\hat{\rho}_{\text{SPDC}} &= \left(1-\lambda^2\right)\sum_n^\infty\sum_{n'}^\infty \lambda^{n+n'}\,|n,n\rangle\langle n',n'| = \\ &= \left(1-\lambda^2\right)\sum_n^\infty\sum_{n'}^\infty \lambda^{n+n'}\,|n\rangle\langle n'|\otimes|n\rangle\langle n'|\end{aligned} \tag{4.15}$$

where we can substitute $|n\rangle\langle n'|$ with (4.13), obtaining

$$\begin{aligned}\hat{\rho}_{\text{SPDC}} = \left(1-\lambda^2\right)\sum_n^\infty\sum_{n'}^\infty \lambda^{n+n'} &\sum_{k=0}^n\sum_{k'=0}^{n'}\gamma_{kk'}^{nn'}(\eta_s)\,|n-k,k\rangle\langle n'-k',k'| \\ &\otimes\sum_{\ell=0}^n\sum_{\ell'=0}^{n'}\gamma_{\ell\ell'}^{nn'}(\eta_i)\,|n-\ell,\ell\rangle\langle n'-\ell',\ell'|\,.\end{aligned} \tag{4.16}$$

We are clearly not interested in the loss modes, so we can trace them out, yielding

$$\hat{\rho}_{\text{SPDC}}^L = \left(1-\lambda^2\right)\sum_n^\infty\sum_{n'}^\infty \lambda^{n+n'}\sum_{k=0}^n\sum_{\ell=0}^n\gamma_{kk}^{nn'}(\eta_s)\gamma_{\ell\ell}^{nn'}(\eta_s)\,|n-k,n-\ell\rangle\langle n'-k,n'-\ell|\,. \tag{4.17}$$

While we made the assumption in (4.6) that we were dealing with a perfect setup, now we have the necessary details to drop this assumption, and check what's going on when we have

real components. The heralding probability, assuming that our heralding mode is the idler one, is

$$\begin{aligned} p_H(\eta_i,\eta_d) &= \mathrm{Tr}\{\hat{\rho}^L_{\mathrm{SPDC}}\Pi(1)\} = \\ &= (1-\lambda^2)\sum_{n}^{\infty}\sum_{n'}^{\infty}\lambda^{n+n'}\sum_{k=0}^{n}\sum_{\ell=0}^{n}\sum_{N=1}^{\infty}\gamma_{kk}^{nn'}(\eta_s)\gamma_{\ell\ell}^{nn'}(\eta_i)p_d(1|N)\times \\ &\times\sum_{m,m'}^{\infty}\langle m,m'||N\rangle\langle N||n-k,n-\ell\rangle\langle n'-k,n'-\ell||m,m'\rangle \end{aligned} \tag{4.18}$$

which is just a cornucopia of Kronecker deltas, i.e. $\delta_{ij}=0$ if $i\neq j$. These amount to $n=n'$ and $n-\ell=N$, infinite sums of geometric series and binomial expansions, like most of the rest of this section will be. Together with the previous constraint that $\ell=\ell'$, this let's us simplify the factors $\gamma_{\ell\ell'}^{nn'}(\eta_i)$ to

$$\gamma_{\ell\ell'}^{nn'}(\eta_i)=B^n_{n-N}B^n_{n-N}\frac{(n-N)!N!}{n!}\eta_i^N(1-\eta_i)^{n-N}=B^n_{n-N}\eta_i^N(1-\eta_i)^{n-N}=\gamma_N^n(\eta_i). \tag{4.19}$$

The factors $\gamma_{kk'}^{nn'}$ also undergo a similar transformation, taking into account also that $k=k'$

$$\gamma_{kk'}^{nn'}(\eta_s)=B^n_k\eta_s^{n-k}(1-\eta_s)^k=\gamma_k^n(\eta_s). \tag{4.20}$$

Taking a closer look at (4.18), we can see that the sum over k is independent of N, and it amounts to one. It's the polynomial expansion of $(\eta_s+(1-\eta_s))^n$, which is 1 independent of η_s. This makes intuitively sense, because the heralding probability *cannot* depend on the collection efficiency of the signal arm. The sum over N *looks* the same, but care must be taken to check the limits of the sum. The sum over N starts at one, and this restricts also the sum in n to start at one. This is because $n,\ell,N\in\mathbb{N}_0$ and as we said $n-\ell=N$, but if the minimum value of N is 1, then it must be that the minimum value of n is also 1. Lastly, the upper bound of the sum over N must be n, so that the factorials in $\gamma_N^n(\eta_i)$ are defined. This leaves us with

$$p_H(\eta_i,\eta_d)=(1-\lambda^2)\sum_{n=1}^{\infty}\lambda^{2n}\sum_{N=1}^{n}\gamma_N^n(\eta_i)p_d(1|N) \tag{4.21}$$

which, for $\eta_i=1$, is the same as (4.6).

To move forward, we need to choose which type of detector we are going to use, so that we can plug the appropriate form of $p_d(1|N)$. If we use a bucket detector, we can extend the sum over N to 0, since $(1-(1-\eta_d)^0=0)$, leading us to

$$\begin{aligned} p^B_H(\eta_H) &= (1-\lambda^2)\sum_{n=1}^{\infty}\lambda^{2n}\sum_{N=0}^{n}\gamma_N^n(\eta_i)\big(1-(1-\eta_d)^N\big)= \\ &= (1-\lambda^2)\sum_{n=1}^{\infty}\lambda^{2n}(1-(1-\eta_i\eta_d)^n)= \\ &= (1-\lambda^2)\left(\frac{1}{1-\lambda^2}-\frac{1}{1-\lambda^2(1-\eta_H)}\right)= \\ &= \frac{\lambda^2\eta_H}{1-\lambda^2(1-\eta_H)} \end{aligned} \tag{4.22}$$

where $\eta_H = \eta_d \eta_i$ is the overall heralding efficiency of the idler arm. A sanity check confirms that for $p_H^B(\eta_H = 0) = 0$ and $p_H^B(\eta_H = 1) = \lambda^2$.

The reduced heralded state $\hat{\rho}_H$ is found by tracing over the subspace of the idler and renormalizing:

$$\begin{aligned}\hat{\rho}_H^B &= \frac{\mathrm{Tr}\{\hat{\rho}^L_{\mathrm{SPDC}}\Pi(1)\}_s}{p_H^B(\eta_H)} = \\ &= \frac{1-\lambda^2}{p_H^B(\eta_H)} \sum_n^\infty \sum_{n'}^\infty \lambda^{n+n'} \sum_{k=0}^n \sum_{\ell=0}^n \sum_{N=1}^\infty \gamma_{kk}^{nn'}(\eta_s)\gamma_{\ell\ell}^{nn'}(\eta_i) p_B(1|N) \times \\ &\times \sum_m^\infty \langle m||N\rangle\langle N|\,|n-k, n-\ell\rangle\langle n'-k, n'-\ell|\,|m\rangle\,.\end{aligned} \tag{4.23}$$

We can make the same arguments for the case of (4.18) to simplify the equation, realizing that this lead us to $n = n'$ and $\ell = n - N$:

$$\hat{\rho}_H^B = \frac{1-\lambda^2}{p_H^B(\eta_H)} \sum_{n=1}^\infty \lambda^{2n} \sum_{k=0}^n \sum_{N=1}^n \gamma_k^n(\eta_s)\gamma_N^n(\eta_i) p_B(1|N)\, |n-k\rangle\langle n-k|\,. \tag{4.24}$$

The sum over N, is independent of the rest and can be carried out immediately, obtaining

$$1-(1-\eta_H)^n. \tag{4.25}$$

This is nothing more than (4.4), in which the detector efficiency has been modified from η_d to $\eta_d \eta_i = \eta_H$.

Finding the fidelity F to the photon state $|m\rangle$ is straightforward, and follows the same reasoning and algebraic tricks used to obtain p_H^B:

$$\begin{aligned}F_m^B(\eta_H, \eta_s) &= \langle m|\hat{\rho}_H^B|m\rangle = \\ &= \frac{(1-\lambda^2)\lambda^{2m}\eta_s^m}{p_H^B(\eta_H)} \left(\frac{1}{(1-\lambda^2(1-\eta_s))^{m+1}} - \frac{(1-\eta_H)^m}{(1-\lambda^2(1-\eta_H)(1-\eta_s))^{m+1}} \right)\end{aligned} \tag{4.26}$$

The case for PNRDs is similar, and we will spare the details: the whole point of the math-rollercoaster of the previous paragraphs was exactly to explain the methods used to get to the results once. We will only directly give the probability of heralding a single photon

$$p_H^R(\eta_H) = \frac{(1-\lambda^2)\lambda^2\eta_H}{(1-\lambda^2(1-\eta_H))^2} \tag{4.27}$$

and the corresponding probability that the heralded state contains m photons:

$$F_m^R(\eta_H, \eta_s) = \frac{(1-\lambda^2)\lambda^{2m}\eta_s^m\eta_H(1-\eta_H)^{m-1}}{p_H^R} \frac{m + \lambda^2(1-\eta_H)(1-\eta_s)}{(1-\lambda^2(1-\eta_H)(1-\eta_s))^{m+2}} \tag{4.28}$$

This last result is obtained "by noticing that"[1]

$$\sum_{n=m}^{\infty} \frac{nn!x^{n-m}}{(n-m)!} = m!\frac{m+x}{(1-x)^{m+2}} \tag{4.29}$$

and also, regarding the validity of such closed sums, remembering what my university professor of statistical mechanics said during a lecture: we don't check if we can swap a sum and an integral, or if a series converges, we just assume we can, otherwise reality would not exist[2].

Finally, we can calculate the probability that our N multiplexed sources produce a single photon. This equals the probability that *at least* one source fires successfully times the probability that that heralded source actually produced p photons but $p-1$ were lost in the switching network because of losses. We obtain

$$p_M^B = \left(1-\left(1-p_H^B(\eta_H)\right)^N\right)\sum_{p=1}^{\infty} F_p^B(\eta_H,\eta_s)p\eta_n(1-\eta_n)^{p-1} \tag{4.30}$$

for bucket detectors, and

$$p_M^R = \left(1-\left(1-p_H^R(\eta_H)\right)^N\right)\sum_{p=1}^{\infty} F_p^R(\eta_H,\eta_s)p\eta_n(1-\eta_n)^{p-1} \tag{4.31}$$

for PNRDs. These become increasingly tedious to solve analytically but a closed form can still be found. We won't describe all the steps to close the sums because, again, there is nothing new with respect to the previous results: it's always infinite geometric series.

To conveniently write these closed forms, we define two sets of quantities for the case of PNRDs and bucket detectors, with suffixes R and B, respectively. Starting with bucket detectors, we define

$$A_B = \frac{\left(1-\lambda^2\right)\lambda^2\eta_s\eta_n}{p_H^B} \tag{4.32}$$

$$D_B = 1-\lambda^2(1-\eta_H)(1-\eta_s) \tag{4.33}$$

$$d_B = 1-\lambda^2(1-\eta_s) \tag{4.34}$$

$$g_B = \frac{\lambda^2\eta_s(1-\eta_n)}{d_B} \tag{4.35}$$

$$G_B = \frac{\lambda^2\eta_s(1-\eta_n)(1-\eta_H)}{D_B} \tag{4.36}$$

so we can rewrite

$$\sum_{p=1}^{\infty} F_p^B(\eta_H,\eta_s)p\eta_n(1-\eta_n)^{p-1} = A_B\left(\frac{1}{d_B^2(1-g_B)^2} - \frac{1-\eta_H}{D_B^2(1-G_B)^2}\right) = F^B. \tag{4.37}$$

[1] At least, my symbolic calculator did.

[2] I want to stress anyway that we did check the requirements for closing the sums, and they are respected.

For PNRDs, instead, we have

$$k_R = \lambda^2(1-\eta_H)(1-\eta_s) \tag{4.38}$$
$$D_R = 1-k_R \tag{4.39}$$
$$A_R = \frac{(1-\lambda^2)\eta_H}{p_H^R D_R^2(1-\eta_H)} \tag{4.40}$$
$$x = \frac{\lambda^2\eta_s(1-\eta_H)}{D_R} \tag{4.41}$$
$$\gamma = (1-\eta_n)x \tag{4.42}$$

and we use all of these to rewrite

$$\sum_{p=1}^{\infty} F_p^R(\eta_H,\eta_s)p\eta_n(1-\eta_n)^{p-1} = A_R x\eta_n\left(\frac{2\gamma}{(1-\gamma)^3}+\frac{k+1}{(1-\gamma)^2}\right) = F^R. \tag{4.43}$$

Equations (4.37) and (4.43) are the total fidelities of the heralded state, accounting for all possible ways in which we can actually get a single photon, because they account for all possible ways of a false-positive decaying into a single-photon state due to losses.

If we want to understand the merits of multiplexing, we should focus on its building blocks, i.e. the switching network and the number of sources used. To do this, we assume that we have perfect detectors ($\eta_H = 1$) and that the optical loops and routing optics of the signal arm are lossless ($\eta_\ell = \eta_s = 1$). This leaves us with three variables: the type of detector used, the efficiency of each single switch in the network—with the additional assumption that all switches are identical—and the number of sources being multiplexed.

Figure 4.5 gives an overview of how multiplexing affects the performance of a single photon source. The first thing we notice is that we can indeed approach the case in which both the fidelity and the heralding probability tend to 1. This depends on many factors of course, first of all on the type of detector used. As we increase the pump power, of course bucket detectors will allow through more noise due to multi-photon components, driving down the fidelity. On the other hand, a perfect PNRD will of course give us a perfect fidelity, independently on how many sources we multiplex: for a perfect detection scheme and maximal single-photon generation probability of each source (which, for thermal sources, happens when $\langle\hat{n}\rangle = 1$), the fidelity of each heralded state is identically 1, hence why the fidelity does not change neither with pump power nor with number of multiplexed sources (and why the top right plot of Figure 4.5 seems strangely empty). Nonetheless, it's good to keep in mind that the fidelity is of course also dependent on the losses of the system *before* the detector, in general.

Another aspect that depends on the choice of detectors is the probability that a single photon will be delivered at the output. When maximizing the probability that a single source will emit a single photon, the maximum fidelity and heralding probability are both upper-bound to 50% each in the case of bucket detectors. We need to use a lower mean photon number in order to keep down the noise due to multi-photon components. This limitation is not present in the case of PNRDs, but here is evident that the losses of each switch in the network plays a fundamental role as the number of sources increases. What these results underline is the need

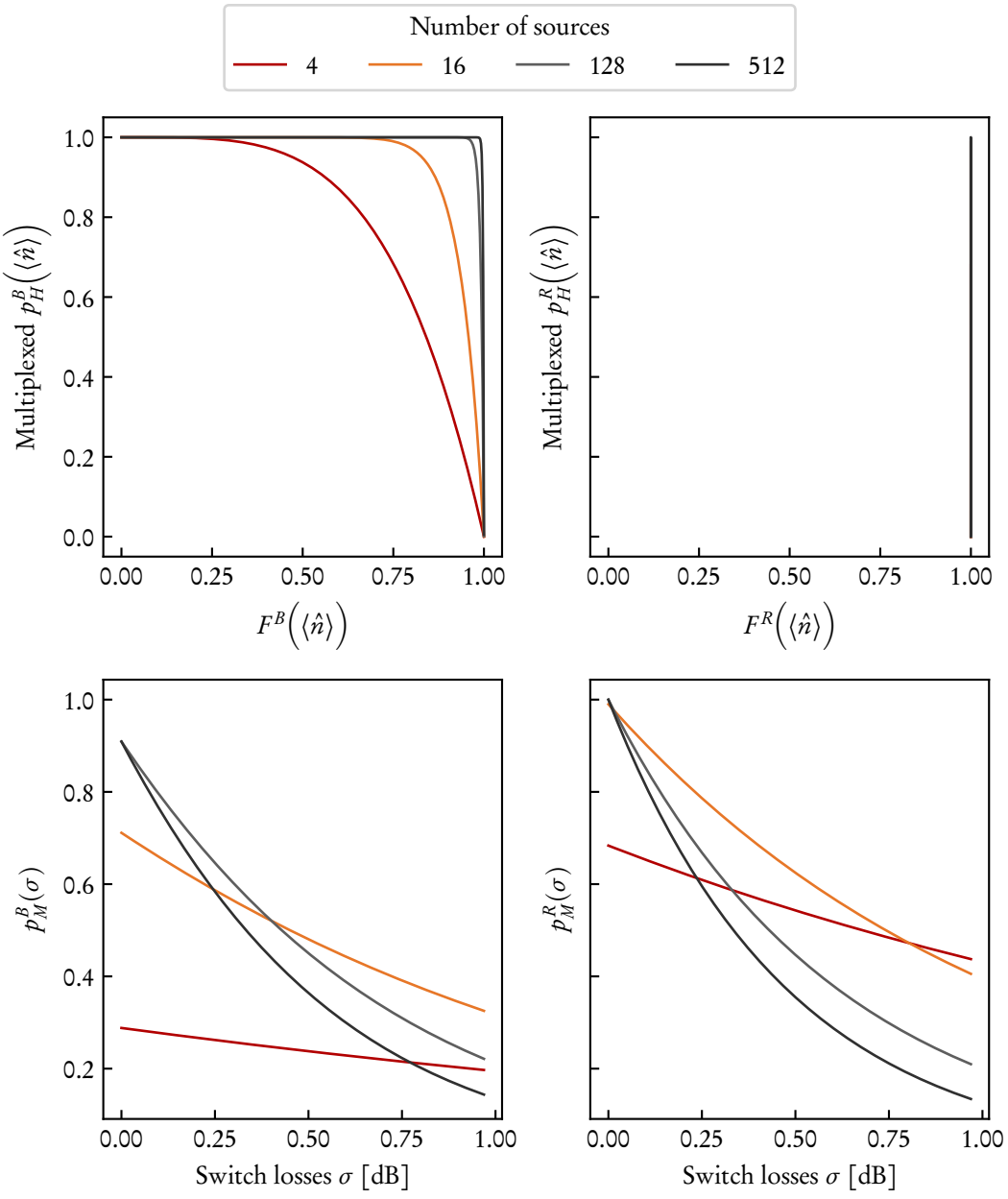

Figure 4.5.: Top row: comparison of heralding probability and single-photon state fidelity for a multiplexed system, with a varying number of multiplexed sources. The curves are parametric in the mean photon number of the source, and we have assumed no losses. Bottom row: multiplexed probability of generating a single photon for different number of sources a function of the efficiency of a single switch, with $\langle\hat{n}\rangle = 0.1$ when using bucket detector, and $\langle\hat{n}\rangle = 1$ when using PNRDs. Left column: bucket detectors. Right column: PNRDs. For details, see text.

for low-loss switches used in the network, since they are the bottleneck of this scheme when it comes to increase the number of sources to be multiplexed.

We would like to point out that the results in the top row of Figure 4.2 *do not depend on the particular architecture* of the multiplexing scheme. There is no reference here on how the different sources are brought together. Rather, these results depend exclusively on the fidelity of a *single* HSPS and the fact that we are waiting for at least one of them to fire. As we will show later in another example of multiplexing architecture in section 4.3, the multiplexed heralding probability has the same form, without references on the details of the implementation.

We have seen here that in ideal circumstances, we still need a hefty number of sources in order to achieve high fidelity and high heralding probability. Sixteen sources might not mean much, but when we start adding losses in the rest of the system, the number of sources starts to rapidly increase. Another point of view is the efficiency of the switch itself: typical insertion losses for off-the-shelf fiber-integrated switches range from 1 dB to 2 dB, which is pretty high and limits the number of sources that can be multiplexed. Lastly, each source requires a detection system—ideally a PNRD—that adds to the cost of the entire multiplexed source. However, one big advantage of spatial multiplexing is that this type of multiplexed sources are fast, because each single source in the system will be pumped synchronously, so that we can scale up the number of sources without increasing the wait time between successive events. Of course, if the rest of the hardware allows it.

4.3. Time multiplexing

What we described as of now looks a bit daunting. Strict efficiency requirements and hardware overhead make spatial multiplexing look like a good idea on paper, and indeed there are experimental realizations of such setups [78, 95]. However, spatial multiplexing is not the only way to orchestrate multiple sources to provide a single output photon, and one other scheme that fixes some of the drawbacks of the spatial multiplexing one is *time multiplexing* (Figure 4.6).

One of the many drawbacks of spatial multiplexing is the ever-increasing hardware requirements that come with increasing number of sources. Time multiplexing fixes this by using a *single* HSPS which gets pumped multiple times, up to N. Each time a pulse triggers a successful heralding event, we store the generated output photon into an optical loop, whose length is such that the time it takes for the photon to complete matches the period at which the source is pumped. After the N pump pulses have been delivered, we release the photon stored in the loop and we start over.

This has the clear advantage that the hardware required to implement the scheme is fixed and does not depend on the number of multiplexed sources. This greatly improves compactness and drives down the cost of the overall setup. The main drawback is, of course, that the rate at which we can deliver triggered single photon at the output is now scaled down by the number of sources we want to multiplex, because we need to wait those many pump cycles before we release the generated photon.

Of course, this setup is also not really "symmetric", because the losses experienced by the photon we stored will depend on *when* it was generated. Worst-case scenario, if we manage to generate a single photon on the first pulse and we store it, that photon will "see" the losses in

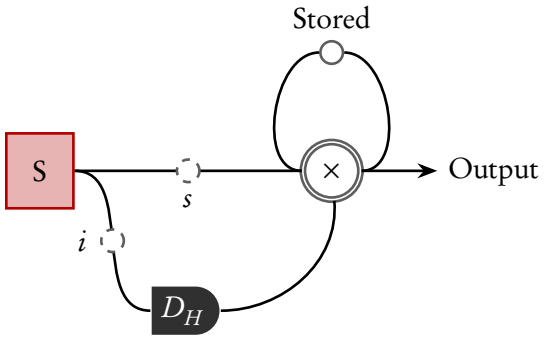

Figure 4.6.: Depiction of a time multiplexing scheme. The source S is pumped periodically with a burst of N pulses, each of which has a certain probability of generating an idler i and signal s photon. If the heralding detector is triggered by the idler, then the coupler switches in a photon. If no photon gets detected at the next pulse in the burst, the coupler is kept in its original state, keeping the stored photon in the loop. At the end of the burst, the stored photon is released.

our loop and routing elements N times. This is not great but can do better. Instead of taking the first photon that we generate, it makes much more sense to take the *last* generated photon and discard all the others. This minimizes the losses seen by the output photon and will increase our chance of actually routing it to the target output mode.

The treatment to obtain the necessary figures of merit for the case of time multiplexing is not much different from the case of spatial multiplexing. Clearly, the probability that a single HSPS on its own delivers a single photon is independent of the scheme in use. The multiplexing probability is also unchanged, since it's the probability that at least one pulse generates an heralding event. The different degree of freedom is irrelevant in shaping the functional form of this quantity. What will change is the fidelity to the single photon state of the entire source. This is because in the case of spatial multiplexing (with identical switches in the network) each source would see the same amount of loss. In the case at hand here instead, each source (i.e. time bin) will see a different amount of loss, due to the fact that it will pass through the loop and switch a different number of times, depending on which source triggers.

The basic components of interest of our scheme are: an optical loop with efficiency η_ℓ; a switch capable of routing a photon in or out of the loop, with an insertion loss of σ; our choice of detection scheme, either bucket detectors or PNRDs. We will follow the treatment of [96].

Assume that we generate a photon in the time bin t out of the total N. The losses seen by this photon are

$$\eta_t = \eta_\ell^{N-t} \sigma^{N-t+1} \tag{4.44}$$

since the photon will pass once through the switch, and then $N-t$ times through both the loop and again the switch. The fidelity of the heralded photon in the time bin t, to the single photon state, is taken by summing over all possible events in which n photons were produced,

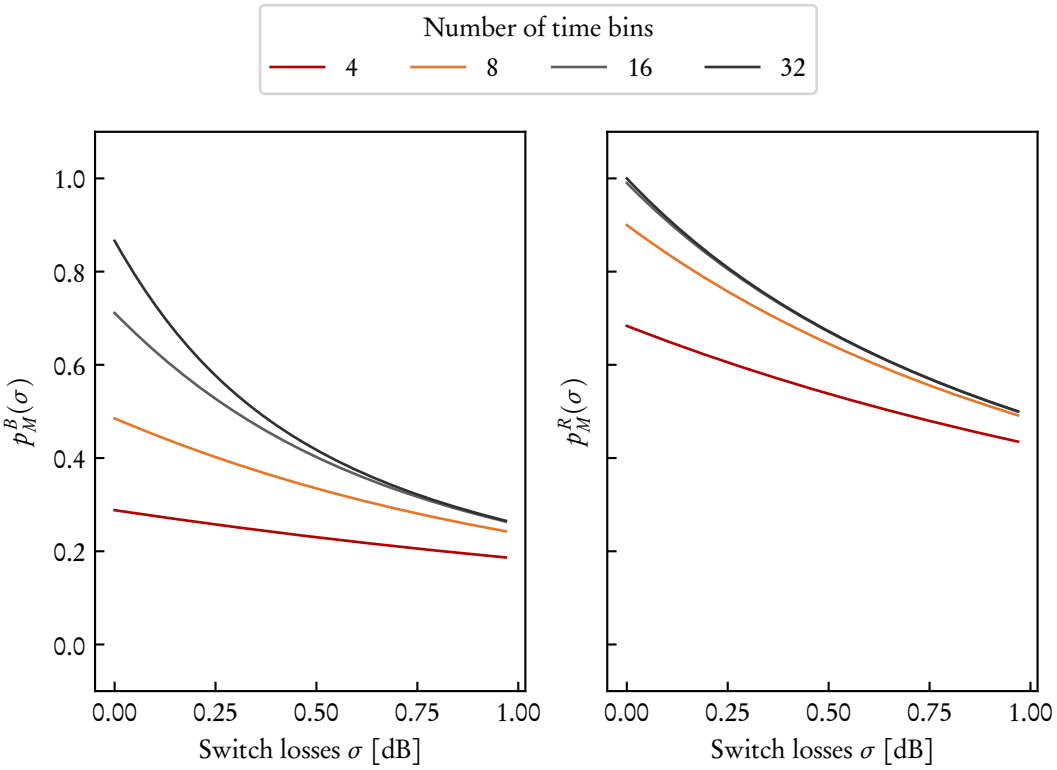

Figure 4.7.: Probability that our time-multiplexed source will emit a single photon as a function of switch loss and for growing number of time bins used. Left: bucket detectors, $\langle\hat{n}\rangle = 0.1$. Right: PNRDs, $\langle\hat{n}\rangle = 1$. All other sources of loss have been removed. For details, see main text.

but only one made it through, as it was the case for spatial multiplexing, namely

$$F_t = \sum_{p=1}^{\infty} F_p^D \, p\eta_t (1-\eta_t)^{p-1}, \tag{4.45}$$

where D labels the chosen type of detector, and F_p^D is one of (4.26) or (4.28).

This describes the probability that a single photon will come out of the t-th time bin, discarding all possible previous ones, and assuming that no further heralding events will trigger. The complete fidelity is going to be the average of such fidelities, weighted with the probability that no further heralding event will be triggered. Since $F_0 = 0$, we have

$$F_{\text{TMUX}}^D = p_H^D \sum_{t=1}^{N} F_t (1-p_H^D)^{N-t}. \tag{4.46}$$

Figure 4.7 shows the performance of our multiplexing scheme as a function of the two most important parameters, number of multiplexed time bins and efficiency of the switch. Here

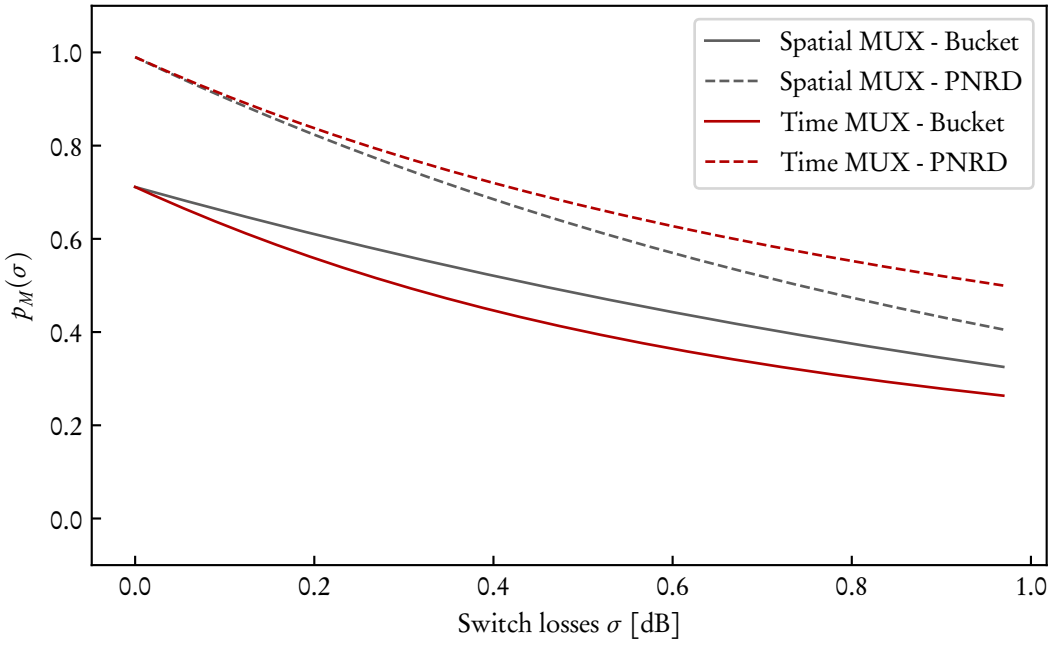

Figure 4.8.: Comparison between single-photon generation probabilities of time and spatial multiplexing, with different types of detectors, as a function of switch losses. Details in the main text.

is also evident that, all other components being the best money can buy, it's paramount that we use a highly efficient switch. Perhaps even more interesting is a direct comparison of time and spatial multiplexing (Figure 4.8). All parameters being equal, time multiplexing has an advantage with respect to spatial multiplexing in terms of efficiency, when PNRDs are used, but the situation is reversed in the case of bucket detectors. This can be understood in terms of how much loss each HSPS experiences in each scheme. In spatial multiplexing, it does not matter which source triggers: the number of components in the path of the heralded photon will always be the same. In the case of time multiplexing, on average, the generated photon will experience *less* losses, because now the amount of loss seen by the generated photon does depend on which source fired, while the probability that each pulse triggers the HSPS is the same regardless of the time bin. The problem here arises because of the inability of bucket detectors effectively distinguish between one or more photons triggering the detector at the same time. This means that a higher number of false positives are let through, and some of these might decay to a single-photon state due to the losses in the setup. Since in time multiplexing the losses of the effective network are less on average, the generated multiphoton state has a lower probability of decaying into a single-photon one, thus having a lower fidelity.

Of course, this is offset by one big advantage of time multiplexing, i.e. we get additional sources "for free". As long as we manage to obtain or fabricate high quality switches and components, there is no additional hardware requirement to increase the number of multiplexed sources. This is a great advantage in the case of bucket detectors, where one needs to drive each

source at very low level in order not to pollute the output with multi-photon components that the detectors are not able to distinguish from single-photon ones. The only way to increase the heralding probability in this case is then to increase the number of sources, which is much more convenient in the case of time multiplexing.

4.4. Conclusions

In order to solve the problem of deterministically generating single photon, using HSPSs, we have introduced the concept of "multiplexing". This technique has proven quite the revelation, allowing us to break free of the limits that single HSPS have on their own. By combining multiple sources together, we can arbitrarily approach both high fidelities to a single-photon state and almost certainty that at each clock cycle we will obtain our photon. We have compared two types of multiplexing, temporal and spatial, but we want to mention that these two are not the only ones in existence. Remember that up until now, we have dealt with a spectrally pure source, in order to ease the math and capture the essence of multiplexing. But since multiplexing is really just multiple single sources, i.e. *squeezers*, we could have used a multi-mode source and multiplex together its various Schmidt's modes. Indeed, this is the basis of *frequency* multiplexing, but the math behind it is at the end of the day the same as for spatial multiplexing, thus we did not mention it up until now. Worth noting is also that there are implementation of each of such schemes [78, 80, 82, 95], underlying the fact that interest in this area is high, and for good reasons.

But, of course, "all that glitters is not gold". Indeed, the introduction of multiplexing increases dramatically the hardware requirements in order to implement the chosen scheme, which is not only an important economic aspect to consider, but also a problem of added complexity in general. To be viable, high quality components need to be used and it would be desirable to also reduce the overall footprint of the components used, so that the added hardware complexity is offset by the miniaturization of the latters. This is the direction we are going to go in the next chapter, where we will briefly talk about opto-electronic devices based on $LiNbO_3$ waveguides and their role in source multiplexing.

5. SWITCHING PHOTONS: ELECTRO-OPTIC DEVICES FOR MULTIPLEXED SOURCES

One thing that was consistent in our analysis of multiplexed sources was the ubiquity of devices that we called "switches". We have emphasized that these devices play a crucial role in our setups, and we have based our analysis of the performance of our sources on how efficient these devices are.

The aim of this chapter is introducing briefly some of the concepts behind electro-optical devices. This matter can take a lifetime of research (let alone a doctorate) so we will steer clear of the details and as we have done for the analysis of nonlinearities in crystals, we will highlight the most important features of these devices in what follows.

5.1. WAVEGUIDES AND COUPLED-MODES THEORY

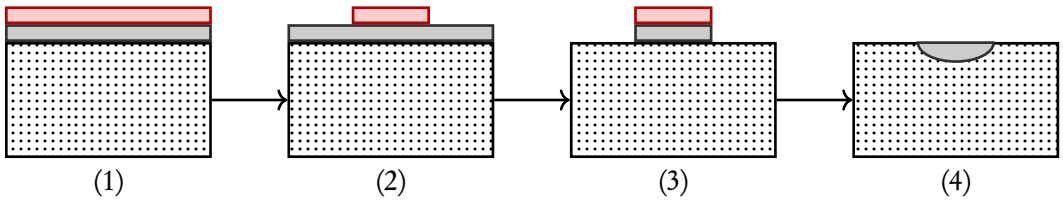

Figure 5.1.: Schematic representation of the fabrication process of a Ti-strip waveguide in $LiNbO_3$. Red: photoresistive film. Gray: titanium layer. Dotted section: $LiNbO_3$ crystal. After depositing a layer of titanium and photoresistive film on top of each other (1), a predefined pattern is developed out of the photoresistive film thanks to a photomask and a lithographic process (2). The exposed titanium is etched away, leaving a stack of photoresistive film and titanium patterned according the mask (3). The photoresistive film is removed and the titanium is diffused in the crystal in a high-temperature oven. This produces a refractive index change in the $LiNbO_3$ crystal, creating a waveguiding structure (4).

Let's start simple and define first of all what a *guided* mode is. A guiding structure, or waveguide from now on, is a structure in which the energy of a propagating field flows only along the structure, not across. Solving the Maxwell's equations in general in waveguiding systems is usually not possible analytically, and a slew of numerical methods and software packages have been developed to tackle this problem. If we assume that ours are weakly guiding waveguides and they are aligned along the x direction of our reference frame, then we can write

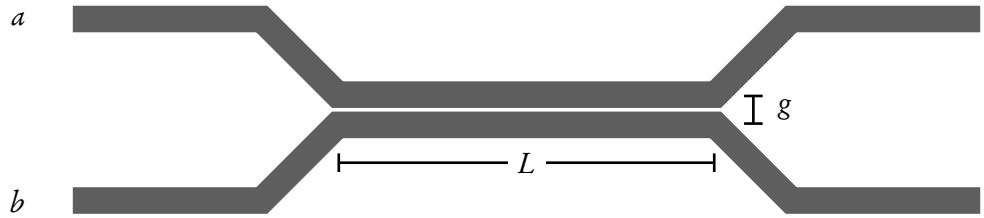

Figure 5.2.: Schematic representation of a direction coupler. The gray regions are waveguides, which slowly approach each other until settling to a core-to-core distance g. The length L is the interaction length, in which the presence of one waveguide perturbs the field distribution in the second one.

the equation for a field $\vec{E} = \vec{\mathcal{E}} e^{i\omega t - \beta x}$ as [97]

$$\nabla_t \vec{\mathcal{E}} + \left(\frac{\omega^2}{c^2} n^2(y,z) - \beta^2 \right) \vec{\mathcal{E}} = 0 \tag{5.1}$$

which can be seen as an eigenvalue problem, in which $\vec{\mathcal{E}}$ are the eigenfunctions and β^2 are the eigenvalues. As per our definition of guiding structure, the eigenfunctions must vanish exponentially at infinity. This means that our field distributions will have a maximum somewhere. In the guiding region, the solutions to the wave equations are oscillatory, but they must match the exponential solutions at infinity. Thus, only a discrete subset of β^2 values are allowed in the guiding region and as many guided *modes*. There is no need to complicate our discussion, and we can immediately say that from now on we will only deal with structures which allow the propagation of a single spatial mode. What's interesting to our discussion is not an isolated waveguide, but rather two in proximity with each other. This is the base of what is called a *directional coupler*.

Assume that we have two waveguides, a and b which are at infinite distance from each other. Then (5.1) can be solved separately in each region and independently from the other and it will yield two solutions $\vec{E}_\alpha$ with $\alpha = a, b$. When bringing close the two waveguides, the total field in the combined structure can be expressed as the sum of the single modes, whose amplitudes varies with x, i.e.

$$\vec{E} = A(x)\vec{\mathcal{E}}_a e^{i\omega t - \beta_a x} + B(x)\vec{\mathcal{E}}_b e^{i\omega t - \beta_b x}. \tag{5.2}$$

The presence of the second waveguide modifies the spatial distribution of the refractive index $n^2(y,z)$ "seen" by the mode of the first waveguide by a small amount, if the waveguides are not too close. By solving (5.1) for the complete field $\vec{E}$, we can arrive [22, 97] to two mutually dependent (*coupled*) equations for the amplitudes $A(x)$ and $B(x)$:

$$\frac{\mathrm{d}A}{\mathrm{d}x} = -i\gamma_{ab} B e^{i(\beta_a - \beta_b)x} - i\gamma_{aa} A \tag{5.3}$$

$$\frac{\mathrm{d}B}{\mathrm{d}x} = -i\gamma_{ba} A e^{i(\beta_a - \beta_b)x} - i\gamma_{bb} B \tag{5.4}$$

in which we have defined the coupling constants

$$\gamma_{ab} = \frac{\omega}{4}\varepsilon_0 \iint \vec{\mathcal{E}}_a^* \Delta n_a^2(y,z) \vec{\mathcal{E}}_b \mathrm{d}y\mathrm{d}z \tag{5.5}$$

$$\gamma_{ba} = \frac{\omega}{4}\varepsilon_0 \iint \vec{\mathcal{E}}_b^* \Delta n_b^2(y,z) \vec{\mathcal{E}}_a \mathrm{d}y\mathrm{d}z \tag{5.6}$$

$$\gamma_{aa} = \frac{\omega}{4}\varepsilon_0 \iint \vec{\mathcal{E}}_a^* \Delta n_b^2(y,z) \vec{\mathcal{E}}_a \mathrm{d}y\mathrm{d}z \tag{5.7}$$

$$\gamma_{bb} = \frac{\omega}{4}\varepsilon_0 \iint \vec{\mathcal{E}}_b^* \Delta n_a^2(y,z) \vec{\mathcal{E}}_b \mathrm{d}y\mathrm{d}z, \tag{5.8}$$

where $\Delta n_\alpha^2 = n_\alpha^2 - n_s^2$, and n_s^2 is the refractive index of the substrate, away from either waveguide. The terms in ab, ba are the coupling between the two waveguides, while the terms in aa, bb modify the propagation constants of the respective modes, due to the presence of the other waveguide.

Assuming no incoming field in waveguide b and $\gamma_{ab} = \gamma_{ba} = \gamma$, we can solve this system of equations and get a way of expressing the optical power in the two waveguides as a function of position:

$$P_a = P_0 - P_b \tag{5.9}$$

$$P_b = P_0 \frac{\gamma^2}{\delta^2 + \gamma^2} \sin^2\left(\sqrt{\gamma^2 + \delta^2}x\right) \tag{5.10}$$

with P_0 the power initially fed into waveguide a and $\delta = \frac{1}{2}(\beta_a + \gamma_{aa}) - \frac{1}{2}(\beta_b + \gamma_{bb})$. We can see that if we assume that the refractive index distributions of the two waveguides are the same and they guide the same type of mode, $\delta = 0$ and we obtain full power transfer only if the region in which each waveguide perturbs the mode of the other (*interaction length* L) has a length of $L_c = (m + 1/2)\pi/\gamma$, which we will call critical interaction length. The state in which power is fully transported into the adjacent waveguide is called *cross* state, while the state in which there is no net power transfer, because $L = m\pi/\gamma$ is called *bar* state.

Of course, devices like these look pretty static, and in fact would serve a very limited amount of applications. Turns out, in fact, that these devices are best used in an *active* way. In general, once you produce such a device, you can't modify its geometry or composition in a practical way, short of grinding the device to shorten it. What you *can* do is take advantage of a class of devices whose refractive index is significantly affected by an externally applied electric field. If that's the case, then this field would be capable of modifying δ and in turn it would be able to modulate the power being transferred from one waveguide to the other, from cross state to bar state and back.

5.2. Electro-optic modulators

The electro-optic effect (or Pockels effect) is a linear effect of some crystals, in which an external field is able to modify the refractive index of the crystal itself. This modifies the impermeability

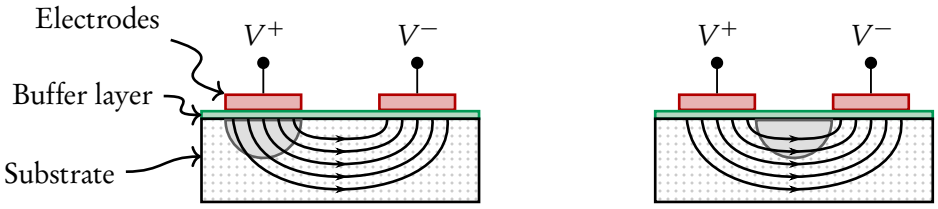

Figure 5.3.: Schematic representation of electrode placement: on top (left) and side-by-side (right) of the waveguide (pictured in gray). Second waveguide of the coupler not pictured and sketch not to scale. Black lines in the $LiNbO_3$ substrate are sketches of the field lines due to the applied voltage on the electrodes.

tensor [97] or equivalently the index ellipsoid. In the absence of an applied field, the index ellipsoid can be written as

$$1 = \frac{x^2}{n_x^2} + \frac{y^2}{n_y^2} + \frac{z^2}{n_z^2} \tag{5.11}$$

where x, y, z are the axes of the crystal. An applied field modifies this into

$$1 = x^2\left(\frac{1}{n_x^2} + r_{1k}E_k\right) + y^2\left(\frac{1}{n_y^2} + r_{2k}E_k\right) + z^2\left(\frac{1}{n_z^2} + r_{3k}E_k\right) + 2xy\,r_{4k}E_k + 2yz\,r_{5k}E_k + 2xz\,r_{6k}E_k \tag{5.12}$$

where summation over k is implied, and $E_{k=1,2,3}$ are the components of the applied field. The components r_{ij} form the *electro-optic tensor*. Depending on the crystal and the direction of the applied field, the net effect can either be a simple stretching of the index ellipsoid or both a stretch and a rotation. The latter means that the electro-optic tensor can also couple different polarizations to each other.

What this means for us is that an application of a field on our waveguide has the potential to modify the refractive index distribution and thus δ in (5.10). The way this is usually done is by placing electrodes either on top or on the sides of a waveguide (Figure 5.3) depending on which component of the electro-optic tensor one want to use and the orientation of the crystal with respect to the electrodes. We can approximate the field distribution made by the pair of electrodes as a parallel plate capacitor and approximate the field E_k responsible for the change in refractive index as $\Gamma V/g$, where V is the applied voltage, g is the gap between the electrodes (usually in the order of µm) and Γ is a correction factor taking into account the overlap between the applied field and the guided mode, obtaining

$$\Delta n(V) = -n^3 \frac{r\,V}{2g}\Gamma. \tag{5.13}$$

5.2.1. Switched directional couplers

These results are crucial for our applications. For multiplexing, we have seen that we need a device that acts as switch, either blocking or letting through our signal, and electro-optics fits the requirements perfectly. Take again (5.10). We start from a situation in which we have

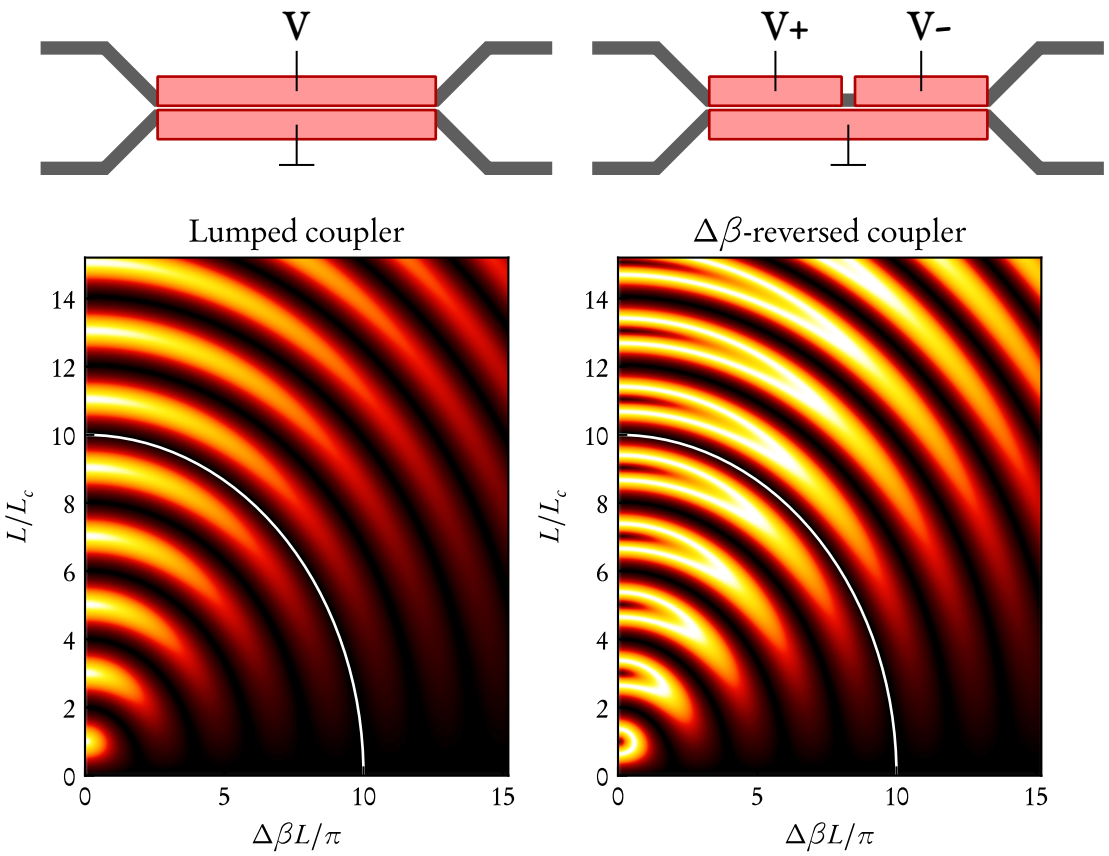

Figure 5.4.: Switching diagrams for two types of electrodes topology: lumped and $\Delta\beta$-reversed. The white lines are an example of combinations of parameters along which we can move to be constantly in the bar state.

constructed a device in which δ is 0 when no voltage is applied and with an interaction length of $x = L_c$. We use a z-cut $LiNbO_3$ crystal in which our waveguides have been fabricated along the x direction. This means that if we look at Figure 5.3, the crystallographic z-axis is pointing upwards, and the y-axis rightwards, assuming that we are looking at the output of the waveguide[1]. In this configuration, an electrode placed directly on top of the waveguide will apply a field which will modify the refractive index proportionally to the r_{33} element of the electro-optic tensor. We can see that by applying a voltage, we can completely *shut off* this power transfer (in the case of an incoming TM field), and switch to the bar state, by applying a total phase-shift $2\delta L_c = \sqrt{3}\pi$. Notice how you can make $\eta = P_b/P_0 = 1$ by carefully choosing the appropriate interaction length, but you can't do that electro-optically, because of the factor in front of the sine in (5.10), which is inversely proportional to the applied voltage.

You can of course have different electrode topologies, and beside the "lumped" electrode type, a common alternative is the "$\Delta\beta$-reversed" coupler (Figure 5.4). This applies an additional degree of freedom in changing β, i.e. space, by periodically reversing the sign of the applied

[1]Which is *very* bad for you eye-sight! Please don't do that.

voltage. The transfer efficiency $\eta_{\Delta\beta}$ for N alternating section is in this case [22]

$$\eta_{\Delta\beta} = \sin^2(\gamma_{\text{eff}} L) \tag{5.14}$$

where

$$\gamma_{\text{eff}} = \frac{N}{L} \arcsin\left(\sqrt{\eta}\right), \qquad \eta = P_b/P_0. \tag{5.15}$$

Looking at Figure 5.4, if we use lumped electrodes, only when L is an odd numbers of critical lengths we can achieve maximum transmission, but controlling this parameter is rather difficult, and once the device is fabricated, it's fixed. On the other hand, we can see that the maximum values of transmission in the case of the $\Delta\beta$-reversed electrodes now *can* be reached electro-optically, which is a big advantage.

We have developed and characterized such $\Delta\beta$-reversed switches, in the hope of implementing a multiplexing scheme based on the concepts developed in chapter 4. These samples were designed to work at 1550 nm, with an interaction length L of 1 cm and a gap g of 7 µm. To characterize their performance, we couple light (DFB diode laser at 1550 nm) into one of the waveguides and monitor the two outputs simultaneously with InGaAs photodiodes. A computer controlled digital-to-analog converter acquisition board (DAQ) takes care of both controlling the applied voltage and recording the signal from the photodiodes. The low voltage signal from the DAQ board is amplified by an in-house-built amplifier, with a rise time of 10 µs, and then applied to the electrodes deposited on the sample via needle probes.

The results are displayed in Figure 5.5. In the colormaps, we plot the output intensity at either port (cross or bar), normalized by their maximum values, as we want to assess the switching efficiency (i.e. how close to zero we can really get). Each point (V_+, V_-) represents a state of the entire switch, and we can find two of such operation points in which the switch is either in the bar $(V_+^{\ominus}, V_-^{\ominus})$ or cross $(V_+^{\otimes}, V_-^{\otimes})$ state. As we can see in the first two plots, we are able to fully control the signal in either port. The problem that we found, and which is shown in the second row of the colormaps, is that after some use (in timescales which vary from minutes to days) the switching map is warped and distorted. When dealing with single-photon experiments, it's not uncommon for data acquisition to date hours or days, so this type of behavior is unsuited for such delicate experiments. This is a problem which is known in the literature [98] and it involves the *buffer layer* between the electrodes and the crystal. The buffer layer is necessary to avoid losses due to the conductive metal being in reach of the guided mode in the waveguide. At the same time, the charge distribution in this layer can be modified by high voltages or prolonged application of low voltages, and spurious currents may develop between the electrodes. This process is not necessarily "elastic", meaning that if no voltage is applied for a long time on the sample, the switching map will not be restored. While this means that these switches can't be used for our purposes, they have provided invaluable insight into how to improve our fabrication methods and the overall design of our devices.

5.2.2. Electro-optic polarization controllers

We want to finish this chapter by introducing another type of electro-optic modulator, whose purpose is to control the polarization state of a field being guided along a waveguide. As we

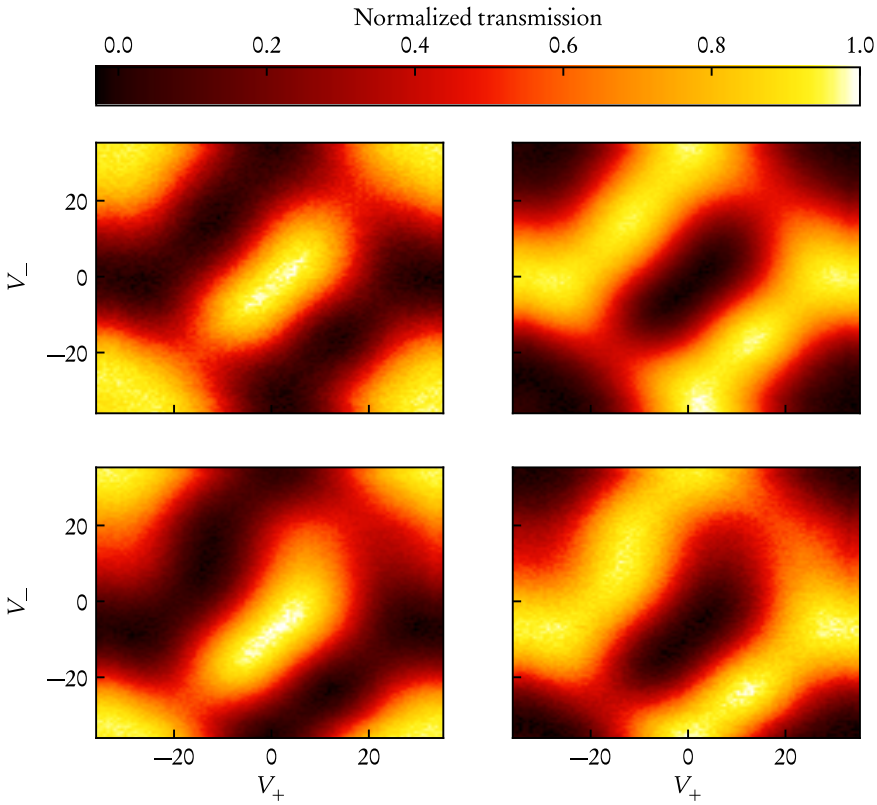

Figure 5.5.: Example of switch characterization for a particular $\Delta\beta$-reversed sample. Top: switching behavior for different voltages V_+ and V_- applied to the two electrodes in one of our $\Delta\beta$-reversed samples. Left column: bar state. Right column: cross-state. First row: initial characterization. Second row: same characterization after prolonged use of the sample. See text for details.

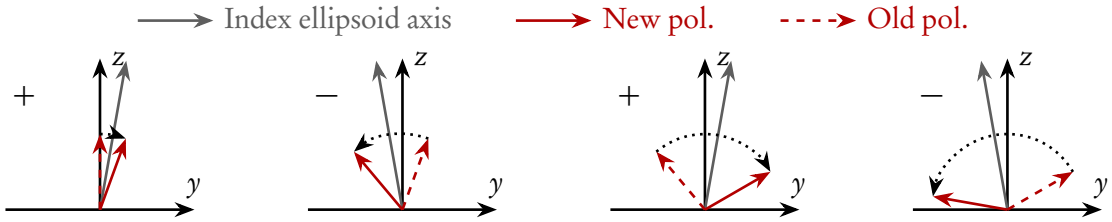

Figure 5.6.: A representation of the "Solč" polarization converter. Each of the four diagrams represents the relationship among the crystal axes (black arrows), index ellipsoid axes (gray arrow, depicting only the "extraordinary" axis), and field polarization direction (red arrows). At each diagram, we advance by half period in our periodically-poled region. At each half period, the sign of the dielectric tensor is inverted by the periodic poling process, indicated by the plus or minus sign in the diagrams. This mirrors the index ellipsoid along the z axis. Since each section acts as a $\lambda/2$–plate, it mirrors the polarization direction along the orientation of the extraordinary axis of the plate. This slowly drives the complete rotation of the polarization of the field.

will see in the next chapter, we will "misuse" this device for other purposes than its intended one, but it's good to have a basic understanding of how such device operates.

We will first describe the concept behind this device qualitatively (Figure 5.6). Consider a waveguide fabricated in a $LiNbO_3$ crystal (a birefringent material) and aligned along the x axis of our reference frame. In the region that we are examining, assume that there is a periodic perturbation of the dielectric material which flips the sign of the dielectric tensor at each half period. Without any applied field, this sign change makes no difference for a field polarized along one of the crystallographic axes. If we now apply a field along the y axis of the crystal, we are introducing a rotation of the index ellipsoid, as we described earlier, since we are now making use of the r_{51} component of the electro-optic tensor. If the period of the perturbation is such that each half-period length of the material acts as a $\lambda/2$–plate, then the polarization of the incoming field will be mirrored accordingly, and it will keep on rotating as long as it moves through the periodic perturbation. This arrangement is known as folded Solč filter [99], and is depicted in Figure 5.6.

More precisely, the effect of the periodic perturbation is to modify the phase mismatch between the two polarization modes, and we can tailor such that

$$\Delta\beta = \beta_o - \beta_e - K = 0, \qquad K = 2\pi/\Lambda \tag{5.16}$$

where Λ is the poling period and the suffixes o and e indicate the ordinary and extraordinary propagation constants. This means that in (5.10) $\delta = 0$, so the transfer efficiency becomes

$$\eta = \sin^2(\gamma L) \tag{5.17}$$

where

$$\gamma \propto n^3 r_{51} \frac{V}{g} \tag{5.18}$$

is the coupling constant between the two polarization modes [22].

5.3. CONCLUSIONS

We have seen a brief introduction on electro-optical devices, which has given us the basics to understand why they are so important in realizing multiplexed sources. They satisfy the fundamental requirement in source multiplexing, which is the fast reconfiguration of the routing network used to select the output of the chosen HSPS. They are not simple devices by any means, as we have shown here, and their construction requires careful planning and constant research efforts to improve their characteristics.

Given the results of our effort for developing electro-optical directional couplers, we went back to the drawing board to see if we could find an alternative multiplexing scheme. This is what we will describe in the next chapter, where we present a new multiplexing scheme based both on time and frequency multiplexing, which uses in a clever way precisely the type of modulator that we presented here last.

6. Orchestrating photons: time-frequency multiplexed single photon source

In our quest for a deterministic single photon source, we have explored various types of multiplexing, weighing their pros and cons. What should be clear by now is that among these solutions, there is no ultimate one. Each design decision we make brings along advantages and disadvantages, and the decision on which side of coin to focus on entirely depends on our needs. If we want to be fast, either spatial or frequency multiplexing is the way to go. Small footprint and overall cost require time multiplexing, enabling us to reuse the same resources many times and driving complexity down.

These are not binary decisions though, and if our requirements allow it, we can try to find a compromise between the full repetition rate speed of spatial multiplexing and the compactness of time multiplexing. In this chapter, we are going to demonstrate such a compromise, introducing a hybrid time-frequency multiplexing scheme that tries to maximize the best features of both individual solutions.

The idea is the following: we transform a single-mode source [12] into a multi-mode one, by creating ad-hoc time-frequency correlations which can later be accessed via frequency-resolved heralding, meaning that by heralding a specific frequency mode, we access the *temporal* information about the idler. We can multiplex the heralded temporal modes into a single output mode by means of a single fast electro-optical modulator [100]. This allows us to avoid the use of a deep switching network, characteristic of a spatially multiplexed source, and the losses due to its components. Moreover, as opposed to usual time-multiplexing schemes, we operate on temporal modes whose spacing is three orders of magnitude smaller, so there is no need to scale down the main system clock by the number of multiplexed modes (in the case of common laser systems used in research settings, whose repetition rate is of the order of 80 MHz). We show that we have successfully characterized the necessary state-engineering setup and the electro-optic modulator involved in this scheme, paving the way to a complete implementation once a suitable mode-selective detection scheme becomes available.

6.1. Multiplexing scheme

Remember that at the end of chapter 4, we hinted at the fact that single mode sources are definitely *not* the only way to go, when creating multiplexed setups and we have seen in chapter 1 that a correlated HSPS can be thought of being composed by some number of pure sources. This is the starting point of the multiplexing scheme that we are going to detail in this chapter.

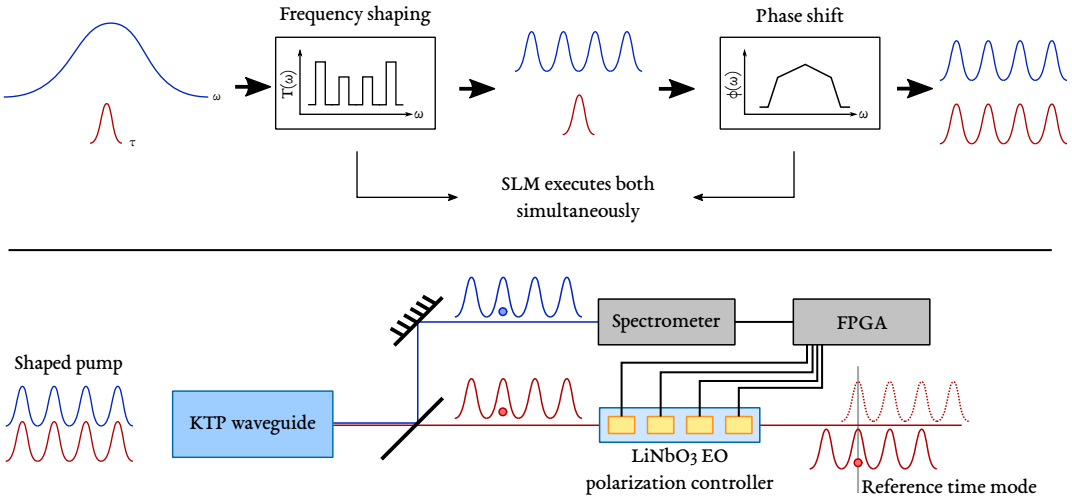

Figure 6.1.: Schematic representation of the multiplexed source. An ultrafast pump pulse centered around 650 nm is first reshaped into N independent frequency modes via an SLM. The latter also adds a frequency-dependent phase shift to each of the N modes in order to separate them in time and creating a one-to-one correlation between a given frequency and time mode. Detection of a given frequency mode at the output of the SPDC triggers the activation of a lithium niobate modulator which compensates the SLM phase shift in the signal arm by rotating its polarization at one of four locations, introducing a phase shift which is dependent on the difference between ordinary and extraordinary refractive indices and the path through the crystal after the switching position.

Our scheme is based on the source detailed in [12]. It's a single-mode KTP birefringent waveguide, with a narrow-bandwidth phasematching, which produces non-degenerate photon pairs, where the idler has a much narrower bandwidth with respect to the signal (top row of Figure 6.2). First, we shape the pump spectrum in order to create different frequency modes in the signal arm, and the narrow-bandwidth and flat phase-matching allows us to this without introducing frequency correlations. Then, we need to turn this into a multi-mode source. To accomplish this, we apply a frequency-dependent phase on the pump pulse, which creates temporal correlations in the generated SPDC state. We can access this multi-mode state by spectrally resolving the signal arm and projecting the signal photon into a well defined frequency mode. A detection event for a given frequency mode gives us information about which time mode the signal is currently occupying. At this point, we can apply the necessary time delay to the idler photon in order to shift it to a predefined temporal mode, thus eliminating the time correlations we have introduced earlier.

This scheme effectively combines the advantages often attributed to either spatial and time multiplexed sources (SMS and TMS from now on, respectively). In our scheme, the selected photon does not propagate through a logarithmic tree of switching components, which removes the hardware overhead and the propagation losses which are inherent in spatially multiplexed sources. At the same time, the temporal separation between the temporal modes in our scheme needs to be such as to ensure negligible overlap between adjacent modes, which is in the order of the coherence time of the signal photons (i.e. picoseconds). Common pulsed laser systems used in research have have repetition rates in the order of 80–70 MHz, i.e. a system clock period of about 12 ns. This is much longer than the overall separation between first and last temporal modes used in this scheme, meaning that we can exploit fully the effective system clocks most commonly available, as opposed to time multiplexed sources. Finally, using a HSPS with a well defined frequency output mode allows us to avoid strong frequency filtering, as would be necessary in a frequency-multiplexed source, which would be detrimental to the final generation rate.

6.2. Experimental setup and characterization

The experimental implementation of such a scheme is based on two major components: a spatial light modulator (SLM) which lets us shape the frequency spectrum of the pulse pumping a KTP birefringent waveguide HSPS and a fast lithium niobate modulator operating as a polarization controller to introduce the necessary picosecond-scale time compensation. Our goal is to characterize both each of these components to ensure that they are suitable for the implementation of the scheme presented earlier.

6.2.1. SPDC spectrum shaping

The source we are using is a KTP waveguide using birefringent phase-matching. Comparing this to usual quasi-phase-matched sources, it means that we are taking advantage of the intrinsic characteristics of the crystal itself and no additional fabrication is required, besides the development of the waveguide itself. The additional advantage is that this source, when pumped with an appropriate wavelength (650 nm), is a spectrally-decorrelated HSPS. It emits photon

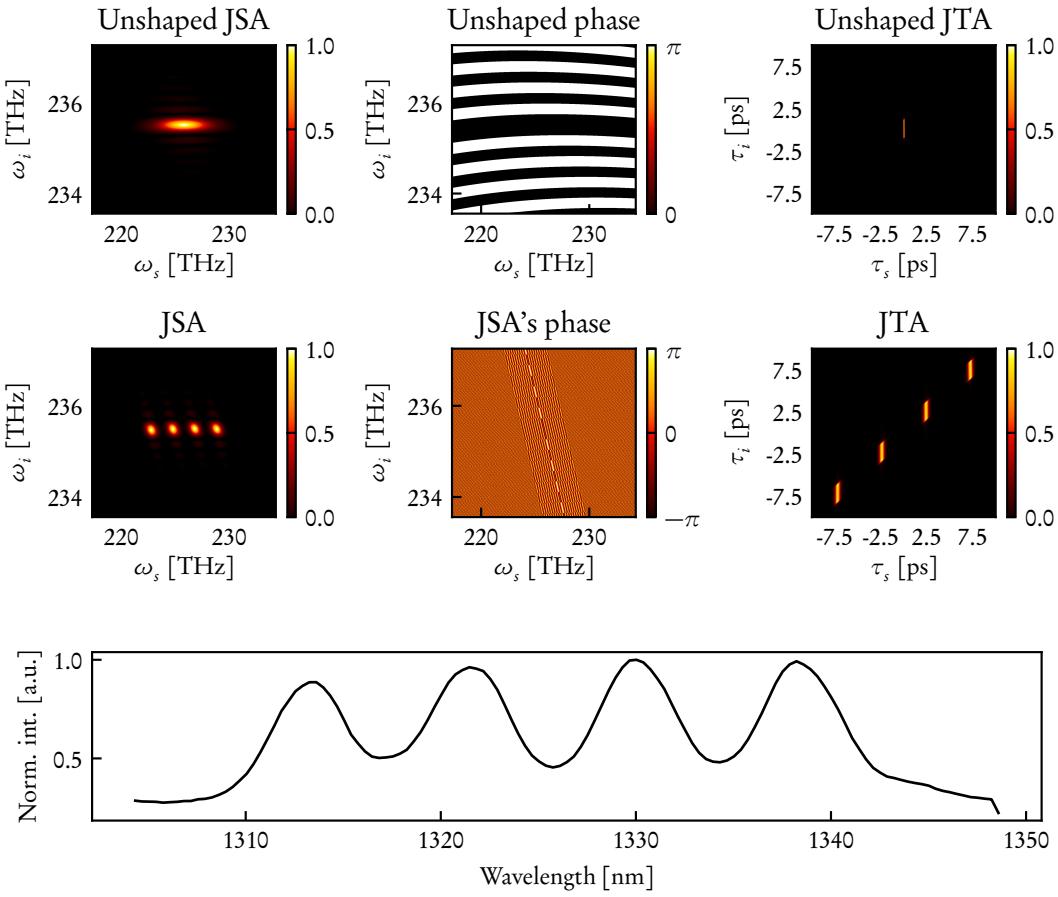

Figure 6.2.: Top: simulated JSA (left) with associated phase (center), and JTA (right) of the original SPDC process, showing an uncorrelated JSA. Middle: simulated JSA (left) with associate phase (center), and JTA (right) of the SPDC process with pump shaping applied, creating four temporal-frequency modes. Bottom: Idler photon spectrum acquired with the TOF spectrometer described in the main text. The reconstructed spectrum's resolution is limited by the amount of dispersion and the relatively high jitter (ca. 1 ns) of the SNSPD used.

pairs at 1273 nm (idler photon) and 1328 nm (signal photon), the former having a 1nm broad bandwidth while the latter having a 30 nm bandwidth. Indeed, a measurement of the second order correlation function of the idler photon, after filtering only the residual side lobes, results in a value of $g_2(0) = 2.02 \pm 0.05$, which is in agreement with the value of 2 expected for a decorrelated source.

In order for our scheme to work, we need to be able to shape the idler photon so that it presents N distinct frequency modes and we need to be able to shift these modes in time by a time $\tau(\omega_i)$, where ω_i is the central wavelength of one of the spectral modes we are generating. We start from a single pump pulse centered at 650 nm. A grating diffracts this pulse, redirecting the various frequency components onto an SLM, which acts both as a programmable mirror and phase shifter. Since the frequency modes are now mapped onto different positions on the SLM screen, we can select which sections of the spectrum to reflect/refract, effectively turning the SLM into a filter which creates the necessary frequency modes for the scheme. We can create efficiently four frequency modes, while keeping a good SNR and ensuring that each mode does not overlap with its neighbors. This is limited by the pump bandwidth and the phase-matching bandwidth. The SLM can also apply an arbitrary phase shift to each newly created frequency mode, enabling us to turn our single-mode source into a multi-mode one (Figure 6.2).

To verify that we are able to shape the SPDC spectra as we need, we first route the signal (broadband) photon to a time-of-flight (TOF) spectrometer (resolution of roughly 0.5 nm), which is composed of dispersive single-mode fibers in conjunction with a superconducting nano-wire single-photon detector (SNSPD, *QuantumOpus*) and a time-to-digital converter (TDC) [101]. After applying the necessary reflection pattern on the SLM screen and adjusting the phase of each frequency component, we register the spectrum given in Figure 6.2. The jitter of the SNSPDs used compromises the resolution of the spectrometer, but we can nonetheless clearly see four frequency modes being generated by the source.

Finally, as last characterization step of the source itself, we want to verify that we are able to also displace in time each of the generated frequency modes. We will measure this time displacement in an HOM-type [102, 103] interference measurement. To do this, a coherent reference field centered around the idler photon's wavelength is prepared. This is accomplished by propagating this reference field through a 4-f line setup, with which we can match the reference's central wavelength and bandwidth to the idler photon's. Afterwards, the reference and the idler photons are interfered at a non-polarizing balanced BS and we scan the relative time of arrival at the BS by changing the optical path length traversed by the reference. The results of such experiment are shown in Figure 6.3, where we can see that we can introduce an arbitrary delay to the idler photon depending on its corresponding frequency mode. The reduction in visibility of the last measurement is due to the setup's instability during very long measurements. Nonetheless, this proves that we have the necessary flexibility in shaping the SPDC output field, which is of crucial importance for our scheme.

6.2.2. Picosecond-range delay line

In our scheme, a detection event in the signal path not only heralds the presence of a twin photon in the idler path, but also carries information about the time delay of said photon with respect to a predetermined reference. This information allows us to collapse our output time

modes into a single one, erasing any time correlations. Here we present how we are able to achieve such precise time manipulation, which happens on picosecond time scales.

The idea comes from [100]: in birefringent materials light experiences different refractive indices depending on relative orientation of the polarization axis of the traveling field and the principal axes of the crystal. This means that two fields traveling with orthogonal polarizations will experience a temporal walk-off which in this case is not a detrimental effect of the material's dispersion, but rather a fundamental one.

A field traveling through such a medium with a linear polarization aligned to the so called "fast-axis" of the crystal, will traverse it in a time t_0. This depends on the length L and absolute value of the group index n_g of the material. If the polarization of the field is changed at a position x inside the material, then it will take an additional time $\tau = \Delta n_g (L-x)/c$, for the field to cross the entire crystal. We can exploit this fact to shift the heralded temporal mode that contains a photon to a reference output mode. To do this, we have produced a lithium niobate device which hosts four 7 mm long polarization converters placed at regular intervals of 18.4 mm. A single polarization converter is composed of a periodically poled region on which gold plated electrodes have been deposited. The two electrodes lie beside the waveguide underneath, such that the application of an electric field will couple the orthogonally polarized modes thanks to the mediation of the r_{51} component of the electro-optic tensor [104], as described in chapter 5. The device (pictured in Figure 6.4) has been designed to work at a central wavelength of around 1275 nm. The total length of the sample is about 82 mm, with internal losses of $0.05\,\mathrm{dB\,cm^{-1}}$. At these lengths, fabricating homogeneous structures becomes non-trivial, so we first characterized the conversion spectrum of each section and tuned each central wavelength to the target one by locally changing the temperature of each section. To achieve this, the sample rests on four copper block whose temperature can be individually set via Peltier elements lying underneath. The operation temperature of each section does not exceed 30 °C and we have found that a 1mm air gap between adjacent sections is enough to avoid thermal coupling.

To characterize the conversion spectra of each polarization controller, a linearly polarized broadband pulse is launched into the device. The electrodes on each section have been connected to independent voltage supplies, in order to individually control each section's conversion "strength" (i.e. what fraction of the incoming field gets converted to the orthogonal polarization mode). A polarizer after the device removes the polarization component parallel to the incoming field's, leaving only what has been successfully converted by the device. This is later analyzed by a spectrometer (*Ando* Optical Spectrum Analyzer AQ6317B). We sequentially maximize the conversion of each section and record the respective spectrum, fine tuning the temperature of each section in order to shift the central wavelength to the target one. An example of such tuning can be seen in Figure 6.5 where we tune each section individually in a range from 23.5 °C to 28.5 °C. We find a tunability for the center of the device's phase-matching of $-0.45\,\mathrm{nm\,°C^{-1}}$ on average.

This leads to the data presented in Figure 6.6, where we have recorded the ratio between output and input spectrum of the device, after filtering of fast oscillations due to spurious Fabry-Perot type resonances in our setup. We can see that we are able to overlap all four spectra to the target wavelength thanks to temperature tuning of the individual sections and achieve

almost complete conversion.

The last characterization step is measuring the effective relative delay between polarization modes that each section introduces. We characterize this in the same way we characterized the phase shift introduced by the SLM, i.e. via an HOM-type interference. We prepare a reference field in the same fashion and interfere it with the idler output of the SPDC after propagation through our device. We start by aligning the idler photon to the slow axis of the crystal, so that each section will rotate it to the fast one. We then scan the relative path lengths of the two interfering fields when one of the four sections is set to fully convert the polarization state, while the others are set to have no effect. This leads to the data in Figure 6.7, where we can see that each section's activation leads to a different shift in time.

According to data from [105, 106], we expect each section to introduce a delay of about 5.07 ps but our measured section delays do not perfectly agree with this figure. This can be attributed to the fact that, as previously stated, fabricating long homogeneous samples is difficult and small imperfections in the waveguide's geometry influences the effective refractive index seen by the propagating field, which will inevitably differ from the one in the aforementioned work. Nevertheless, this does not hinder the application of our scheme, since the pump's time profile can be fine-tuned by the SLM to account for such deviations, once they are known.

To complete this scheme, we need a time-selective measurement that rejects the spurious modes remaining after the selected signal photon has been shifted. One way is of course direct detection of such time modes. This requires not only extremely fast SNSPDs with a time jitter lower than the lowest section's delay [107], but also fast enough data acquisition electronics to record such events. This proves to be rather difficult, as the electronics required for such timings lies in the 10–100 GHz range. An easier way would be to rely on time-selective optical processes. One example would be homodyne detection, which, being mode-selective, lends itself very well to the task. While good for benchmarking and testing, homodyne detection effectively destroys the prepared photon, which is not ideal when building a single-photon source. A third alternative would be to use a device like the quantum pulse gate [108]. This device not only is mode-selective, but the mode-selection process generates a photon which lies in a fixed temporal mode, and it's then available to be used. As a further advantage of this solution is that it is based on the same platform as the delay device itself, which allows in principle for both components to be integrated into a single one.

6.3. Conclusion

We started this chapter by saying that there is no singular "best" solution when it comes to multiplexing, and compromises must be reached. This is true also for our implementation, where there are clear advantages and disadvantages. Our solution uses a source which is spectrally decorrelated *from the start*. This removes the problem of reducing the probability of delivering a photon at the output (i.e. an increased η_s in chapter 4) because no tight filtering is necessary. Secondly, no loop or photon storage is necessary, unlike time multiplexing, since ours is a single-pass solution. This avoids additional losses due to the storage of the photon in an optical delay line, as seen in time multiplexing. Finally, we are able to use a narrower bandwidth for our modulator, with respect to frequency multiplexing schemes. This is because we can focus

on the single frequency mode that our HSPS produces as idler photon, another advantage of using a spectrally pure HSPS.

The limitation of this scheme lies mainly in the phase-matching of the source used. We have chosen a range of wavelength in which the phase-matching function is rather flat for the idler photon, but this of course limits the number of modes we can multiplex. If we want to increase this number, we need to pack more modes in the same frequency range, and this means more filter and consequently lower generation rates. Also, with each new mode we need to add a corresponding detector to herald its presence, driving up the hardware overhead.

We have shown that each component in the proposed scheme works as expected and that the setup is flexible enough to account for fabrication imperfections that can arise in such devices. It combines advantages from multiple pre-existing solutions in an integrated platform. We believe that with proper mode-selective filtering and fast detection, it's possible to create a more compact and resource-efficient source of single-photons which overcomes the physical limits of standard HSPSs and can be easily either directly integrated or externally interfaced with other integrated components, thanks to the efficiency with which devices based on lithium niobate can be fiber pigtailed [13].

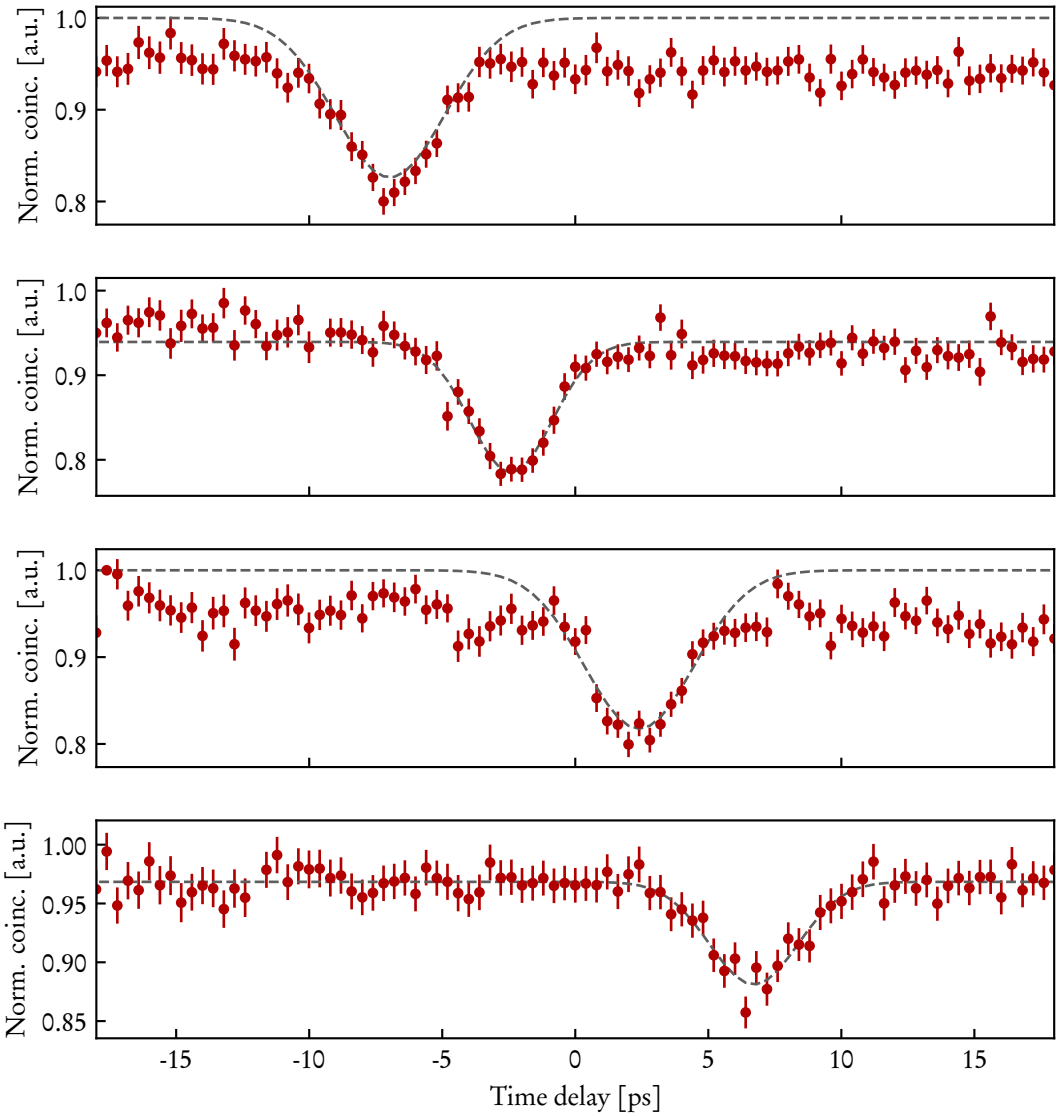

Figure 6.3.: HOM interference between the idler photon of the SPDC after shaping and a reference field at 1275 nm. Dots are experimental data, dashed lines are fits to this data. Each trace represents the interference between the reference field and one of the aforementioned modes, when the remaining three are not present. The sudden jumps which are visible in some parts of the traces (e.g. the right side of the third trace from the top) are due to automatic tuning of the OPO cavity used as seed for the pump of the SPDC. Instability in ambient temperature in the lab does not allow us to disable such readjustments, since the cavity would drift too rapidly compared to the time required for each trace to be acquired.

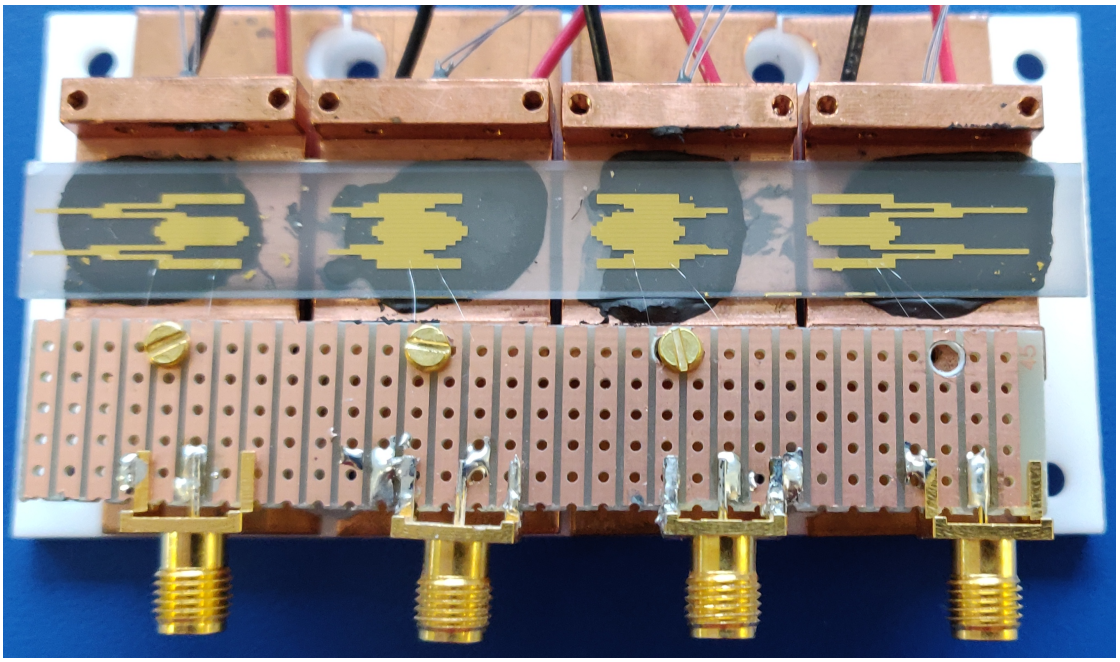

Figure 6.4.: Photograph of one of the polarization-based delay chips, and the one whose characterization we describe in the main text. The sample rests on a holder composed of four thermally isolated sections. Each section holds a Peltier module which is used to regulate the individual temperature of each controller. The sample is glued onto the holder with a thermally conductive glue, which enables optimal heat transfer. We have found that the thermal conductivity from adjacent sections is low enough that no temperature cross-talk occurs, even if we are modulating the temperature of a single crystal. Lastly, SMAs connectors can be seen at the bottom of the picture, which allow us to control the applied voltage to a section

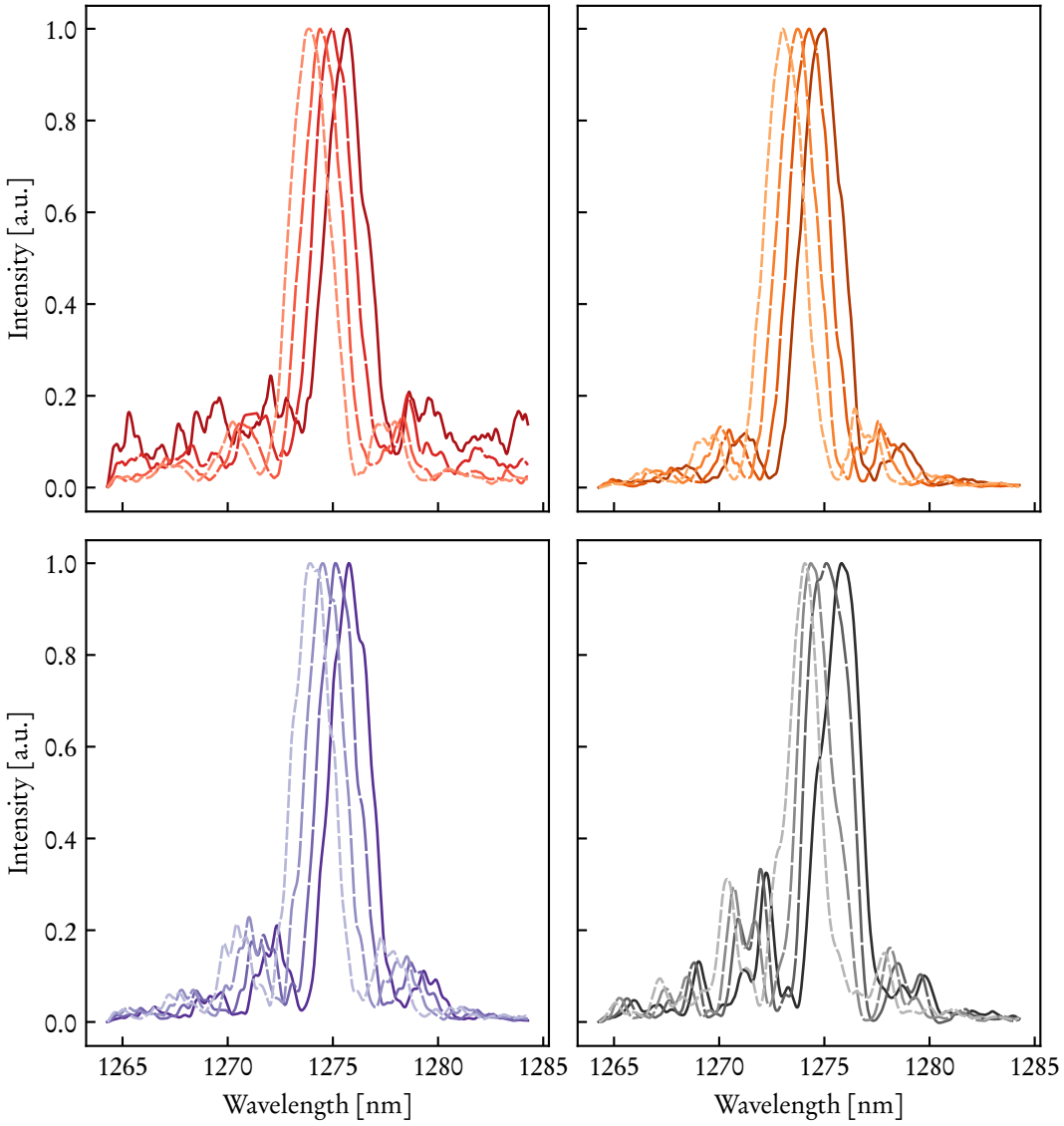

Figure 6.5.: Tuning of the phase matching for each individual section, from left to right and from top to bottom. The darker the color, the lower the temperature. The data has been smoothed to remove spurious Fabry-Perot resonances that would compromise the readability of the plots.

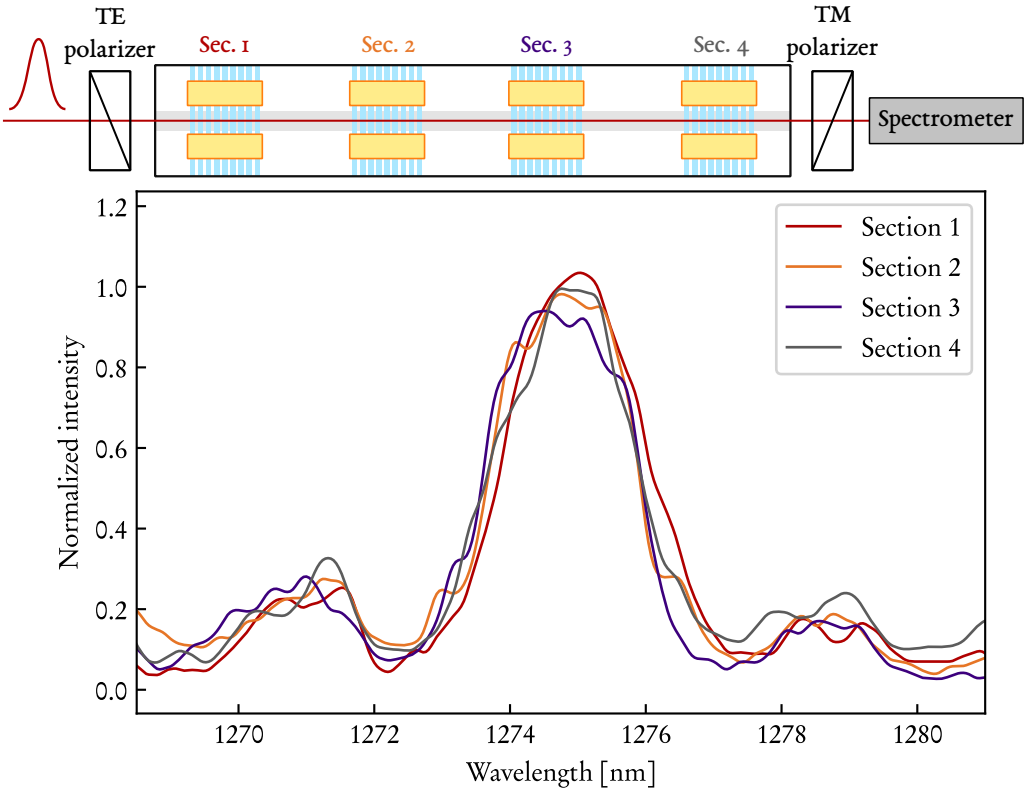

Figure 6.6.: Top: schematic representation of the spectral characterization setup. One state of polarization is coupled into the device and get converted to the orthogonal one by one of the sections, one at a time. The output polarizer analyzes this converted field and the latter is registered by the spectrometer. Bottom: the spectra of the individual polarization controllers, after proper temperature tuning. This shifts the central wavelength of the individual sections, maximizing the mutual overlap of all spectra.

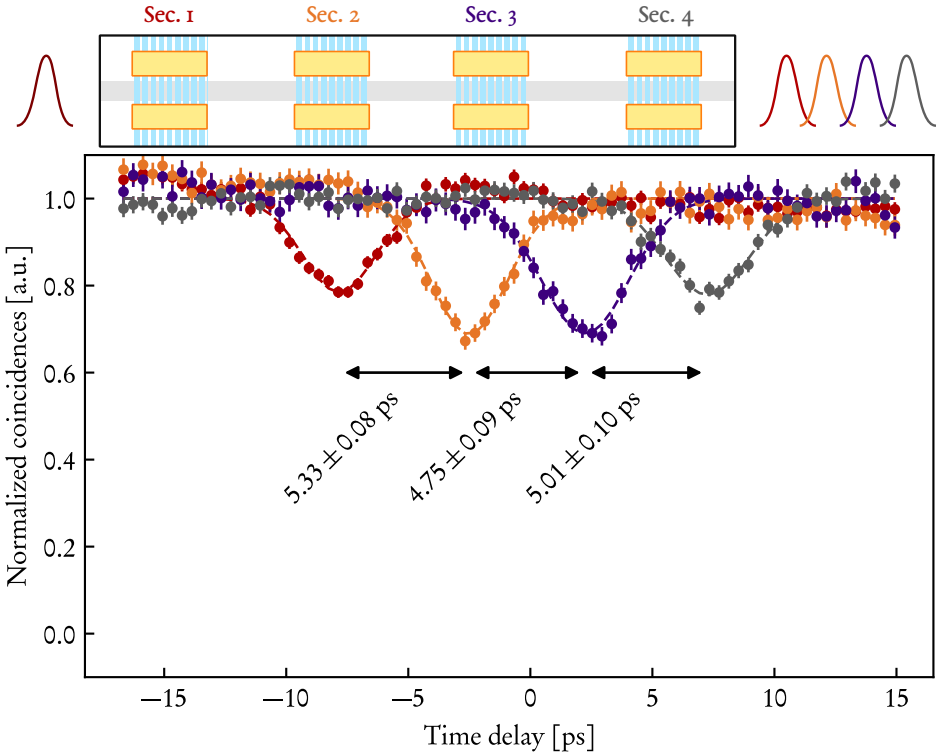

Figure 6.7.: Top: schematic representation of the delay introduced depending on the active section. By selecting and activating a given polarization controller, we can decide to shift an incoming pulse to a given output time mode. Bottom: HOM interference traces for each section, when only the respective section is active. Points are experimental data, dashed lines are Gaussian fits to said data.

7. Conclusions

The quest for the "perfect" single-photon source is far from over. Over the years more and more solutions, platforms, materials, and clever setup arrangements dot research journals and conferences, promising great performances and a bright future. Indeed, this research field is experiencing a great drive, boosted by the demand of smaller, more efficient and user-friendlier devices. Integrated single photon sources (be it in $LiNbO_3$, KTP, NV-centers, quantum dots, or others) have the potential to finally make the much touted "second quantum revolution" a practical reality.

This works has dealt with the most important aspects of deterministically generating single photons from spontaneous parametric down-conversion sources. We have described the necessary theoretical background in order to have a solid overview of the processes that we want to exploit. With this knowledge, we set out to make use of it, by demonstrating how a HSPS can be used and interfaced with other technologies effortlessly and without compromising its quantum nature. This further demonstrated how SPDC sources are mature components that can be used as proper tools or instruments. This also means that investigating the technical performances (and not just the physics) of such sources is a worthy endeavor, in order to tailor them to different experimental requirements. To this end, we took as an example the task of increasing the spectral purity of a correlated source while maintaining high heralding rates. We have demonstrated how it is possible to modify standard filtering techniques, used to increase the purity of a correlated SPDC source, in order to improve generation rates, without also compromising the single-photon character of the source.

We have realized that at a certain point we need to look elsewhere, and cannot rely on single sources anymore. We have described the concept of source multiplexing and expanded a theoretical framework for assessing the role of losses in the two most common multiplexing schemes, space and time multiplexing. We have highlighted how the two schemes compare with each other and how their performance is not only tied to the quality of the components used, but also on the detection technique used.

One of the main points that our theoretical analysis underlines is that for these multiplexing schemes to be viable, we need to have access to high quality components that allow us to reconfigure our setup on-the-fly. We resorted to the use of electro-optic devices and we have explored their fundamentals to understand why and how they can unlock the potential of multiplexed sources. Although the samples produced did not perform well enough to be used in a practical implementation, they did provide invaluable insight into the design and fabrication processes involved in their production, allowing us to improve the quality of our devices.

Finally, we have devised a novel multiplexing scheme based on tailored time-frequency correlations. This scheme aims to be a compromise between the speed of spatially multiplexed sources and the compactness of time multiplexed ones. We have shown how we are able to multiplex temporal modes in time scales orders of magnitude smaller than loop-based time

multiplexed setups. Thanks to this it is possible to take advantage of the full repetition rate of conventional pulsed laser systems, without the need of deep switching networks, which are on the other hand necessary in spatially multiplexed sources. Also, by using a pure SPDC source, we are able to use modulators with much smaller spectral bandwidth requirements, when compared to frequency multiplexed sources, which are much easier to fabricate.

Acknowledgments

Maybe the first thing I do when I read thesis from someone else in the past, is to start from a glimpse at the acknowledgments. By their nature, they provide an insight in the life of the person behind the work, be it on purpose or not, and help the reader to (maybe) emphasize with the author. If you, Reader, are like me and started from here, or simply are *still* here, please do read onwards.

I genuinely want to thanks my supervisor, Prof. Dr. Christine Silberhorn. For the obvious, that is for welcoming me in her group and giving me this great opportunity, and for the less obvious, for believing in me throughout my studies.

Next, I cannot stress how much grateful I am for having had Harald Herrmann and Kai Hong Luo around. The amount of things I have learned from both of them is staggering, both by actually working with them and by suddenly dropping by their office and asking random question. I would have not gotten here if not for them.

A special mention must go to Vahid Ansari, who helped me out a great, great deal in my last year, even when in the midst of a bureaucratic nightmare. Also, for agreeing to embark on a trip which is, up to now, probably the best I've been on.

My time here has been undeniably made easier thanks to a group of people who I am lucky enough to call both friends and coworkers: Jano Gil López, Matteo Santandrea, Michael Stefszky, and Tanya Matthew. I think it's going to be hard finding such a group wherever I'm going next.

Of course, being a Ph.D. *student*, I have learned a lot during these four and a half years, and not just from papers and books. The atmosphere in the IQO group has been great, with everyone always willing to discuss any problem, any time and help out whenever possible. I hear stories about how hard is to go along with coworkers and I am grateful I can't relate to these stories.

It's unbelievable for me that given the thousands of kilometers separating me from my homeland, some friendships withstood the test of time. The "Giampaoli Worldwide" group had a big role in keeping homesickness at bay, and I'm extremely thankful for that. I want to thank in particular Salvo, Renato, and Guglielmo, who kept me sane over the years.

Next, I would *literally* not be here if not for my family. Their support has been unmatched and they are the reason I was able to pursue this path. Thanks for the overwhelming support!

Last, I want to thank Angelina, and I probably cannot thank her enough for putting up with me, with me under stress, and with me, under stress during a global pandemic. You made the last years fly by. I look forward to more of them!

BIBLIOGRAPHY

[1] Fulvio Flamini, Nicolò Spagnolo, and Fabio Sciarrino. Photonic quantum information processing: a review. *Reports on Progress in Physics*, 82(1):016001, January 2019. ISSN 0034-4885, 1361-6633. doi: 10.1088/1361-6633/aad5b2. URL https://iopscience.iop.org/article/10.1088/1361-6633/aad5b2. vii

[2] E. Knill, R. Laflamme, and G. J. Milburn. A scheme for efficient quantum computation with linear optics. *Nature*, 409(6816):46–52, January 2001. ISSN 0028-0836, 1476-4687. doi: 10.1038/35051009. URL http://www.nature.com/articles/35051009. vii

[3] J. L. O'Brien. Optical Quantum Computing. *Science*, 318(5856):1567–1570, December 2007. ISSN 0036-8075, 1095-9203. doi: 10.1126/science.1142892. URL https://www.sciencemag.org/lookup/doi/10.1126/science.1142892. vii, 21

[4] Andrew J. Shields. Semiconductor quantum light sources. *Nature Photonics*, 1(4):215–223, April 2007. ISSN 1749-4885, 1749-4893. doi: 10.1038/nphoton.2007.46. URL http://www.nature.com/articles/nphoton.2007.46. vii, 3

[5] Stefan Strauf, Nick G. Stoltz, Matthew T. Rakher, Larry A. Coldren, Pierre M. Petroff, and Dirk Bouwmeester. High-frequency single-photon source with polarization control. *Nature Photonics*, 1(12):704–708, December 2007. ISSN 1749-4885, 1749-4893. doi: 10.1038/nphoton.2007.227. URL http://www.nature.com/articles/nphoton.2007.227.

[6] Peter Michler. A Quantum Dot Single-Photon Turnstile Device. *Science*, 290(5500):2282–2285, December 2000. ISSN 00368075, 10959203. doi: 10.1126/science.290.5500.2282. URL http://www.sciencemag.org/cgi/doi/10.1126/science.290.5500.2282. 3

[7] Raphaël S. Daveau, Krishna C. Balram, Tommaso Pregnolato, Jin Liu, Eun H. Lee, Jin D. Song, Varun Verma, Richard Mirin, Sae Woo Nam, Leonardo Midolo, Søren Stobbe, Kartik Srinivasan, and Peter Lodahl. Efficient fiber-coupled single-photon source based on quantum dots in a photonic-crystal waveguide. *Optica*, 4(2):178, February 2017. ISSN 2334-2536. doi: 10.1364/OPTICA.4.000178. URL https://www.osapublishing.org/abstract.cfm?URI=optica-4-2-178. vii

[8] E Wu, J R Rabeau, G Roger, F Treussart, H Zeng, P Grangier, S Prawer, and J-F Roch. Room temperature triggered single-photon source in the near infrared. *New Journal of Physics*, 9(12):434–434, December 2007. ISSN 1367-2630. doi: 10.1088/1367-2630/9/12/434. URL http://stacks.iop.org/1367-2630/9/i=12/a=434?key=crossref.89fa8ee5f08e8dc02c01fd555eda2d3f. vii

[9] T Gaebel, I Popa, A Gruber, M Domhan, F Jelezko, and J Wrachtrup. Stable single-photon source in the near infrared. *New Journal of Physics*, 6:98–98, July 2004. ISSN 1367-2630. doi: 10.1088/1367-2630/6/1/098. URL http://stacks.iop.org/1367-2630/6/i=1/a=098?key=crossref.c22c6711b1c99f09b470c1b95fb132c0.

[10] Julia Benedikter, Hanno Kaupp, Thomas Hümmer, Yuejiang Liang, Alexander Bommer, Christoph Becher, Anke Krueger, Jason M. Smith, Theodor W. Hänsch, and David Hunger. Cavity-Enhanced Single-Photon Source Based on the Silicon-Vacancy Center in Diamond. *Physical Review Applied*, 7(2):024031, February 2017. ISSN 2331-7019. doi: 10.1103/PhysRevApplied.7.024031. URL https://link.aps.org/doi/10.1103/PhysRevApplied.7.024031. vii

[11] David C. Burnham and Donald L. Weinberg. Observation of Simultaneity in Parametric Production of Optical Photon Pairs. *Physical Review Letters*, 25(2):84–87, July 1970. ISSN 0031-9007. doi: 10.1103/PhysRevLett.25.84. URL https://link.aps.org/doi/10.1103/PhysRevLett.25.84. vii

[12] V. Ansari, E. Roccia, M. Santandrea, M. Doostdar, C. Eigner, L. Padberg, I. Gianani, M. Sbroscia, J. M. Donohue, L. Mancino, M. Barbieri, and C. Silberhorn. Heralded generation of high-purity ultrashort single photons in programmable temporal shapes. *Optics Express*, 26(3):2764, February 2018. ISSN 1094-4087. doi: 10.1364/OE.26.002764. URL https://www.osapublishing.org/abstract.cfm?URI=oe-26-3-2764. 81, 83

[13] Nicola Montaut, Linda Sansoni, Evan Meyer-Scott, Raimund Ricken, Viktor Quiring, Harald Herrmann, and Christine Silberhorn. High-Efficiency Plug-and-Play Source of Heralded Single Photons. *Physical Review Applied*, 8(2), August 2017. ISSN 2331-7019. doi: 10.1103/PhysRevApplied.8.024021. URL https://link.aps.org/doi/10.1103/PhysRevApplied.8.024021. 18, 35, 44, 88

[14] P. G. Evans, R. S. Bennink, W. P. Grice, T. S. Humble, and J. Schaake. Bright Source of Spectrally Uncorrelated Polarization-Entangled Photons with Nearly Single-Mode Emission. *Physical Review Letters*, 105(25), December 2010. ISSN 0031-9007, 1079-7114. doi: 10.1103/PhysRevLett.105.253601. URL https://link.aps.org/doi/10.1103/PhysRevLett.105.253601.

[15] S. Tanzilli, H. De Riedmatten, W. Tittel, H. Zbinden, P. Baldi, M. De Micheli, D.B. Ostrowsky, and N. Gisin. Highly efficient photon-pair source using periodically poled lithium niobate waveguide. *Electronics Letters*, 37(1):26, 2001. ISSN 00135194. doi: 10.1049/el:20010009. URL http://digital-library.theiet.org/content/journals/10.1049/el_20010009.

[16] Fumihiro Kaneda, Karina Garay-Palmett, Alfred B. URen, and Paul G. Kwiat. Heralded single-photon source utilizing highly nondegenerate, spectrally factorable spontaneous parametric downconversion. *Optics Express*, 24(10):10733, May 2016. ISSN 1094-4087. doi: 10.1364/OE.24.010733. URL https://www.osapublishing.org/abstract.cfm?URI=oe-24-10-10733. vii

[17] Evan Meyer-Scott, Nicola Montaut, Johannes Tiedau, Linda Sansoni, Harald Herrmann, Tim J. Bartley, and Christine Silberhorn. Limits on the heralding efficiencies and spectral purities of spectrally filtered single photons from photon-pair sources. *Physical Review A*, 95(6), June 2017. ISSN 2469-9926, 2469-9934. doi: 10.1103/PhysRevA.95.061803. URL http://link.aps.org/doi/10.1103/PhysRevA.95.061803. viii

[18] A. L. Migdall, D. Branning, and S. Castelletto. Tailoring single-photon and multiphoton probabilities of a single-photon on-demand source. *Physical Review A*, 66(5), November 2002. ISSN 1050-2947, 1094-1622. doi: 10.1103/PhysRevA.66.053805. URL https://link.aps.org/doi/10.1103/PhysRevA.66.053805. viii, 55

[19] Andreas Christ and Christine Silberhorn. Limits on the deterministic creation of pure single-photon states using parametric down-conversion. *Physical Review A*, 85(2):023829, February 2012. ISSN 1050-2947, 1094-1622. doi: 10.1103/PhysRevA.85.023829. URL https://link.aps.org/doi/10.1103/PhysRevA.85.023829. viii, 55, 57

[20] Satoshi Kako, Charles Santori, Katsuyuki Hoshino, Stephan Götzinger, Yoshihisa Yamamoto, and Yasuhiko Arakawa. A gallium nitride single-photon source operating at 200 K. *Nature Materials*, 5(11):887–892, November 2006. ISSN 1476-1122, 1476-4660. doi: 10.1038/nmat1763. URL http://www.nature.com/articles/nmat1763. 3

[21] Christoph Söller, Offir Cohen, Brian J. Smith, Ian A. Walmsley, and Christine Silberhorn. High-performance single-photon generation with commercial-grade optical fiber. *Physical Review A*, 83:031806(R), March 2011. ISSN 1050-2947, 1094-1622. URL https://link.aps.org/doi/10.1103/PhysRevA.83.031806. 3

[22] Theodor Tamir, David H. Auston, Walter Engl, Takuo Sugano, and Helmut K. V. Lotsch, editors. *Guided-Wave Optoelectronics*, volume 26 of *Springer Series in Electronics and Photonics*. Springer Berlin Heidelberg, Berlin, Heidelberg, 1988. ISBN 978-3-642-97076-4 978-3-642-97074-0. doi: 10.1007/978-3-642-97074-0. URL http://link.springer.com/10.1007/978-3-642-97074-0. 3, 72, 76, 78

[23] Raffaele Resta. Macroscopic polarization in crystalline dielectrics: the geometric phase approach. *Reviews of Modern Physics*, 66(3):899–915, July 1994. ISSN 0034-6861, 1539-0756. doi: 10.1103/RevModPhys.66.899. URL https://link.aps.org/doi/10.1103/RevModPhys.66.899. 3

[24] Bahaa E. A. Saleh and Malvin Carl Teich. *Fundamentals of photonics*. Wiley series in pure and applied optics. Wiley Interscience, Hoboken, N.J, 2nd ed edition, 2007. ISBN 978-0-471-35832-9. 4, 5

[25] R. S. Weis and T. K. Gaylord. Lithium niobate: Summary of physical properties and crystal structure. *Applied Physics A Solids and Surfaces*, 37(4):191–203, August 1985. ISSN 0721-7250, 1432-0630. doi: 10.1007/BF00614817. URL http://link.springer.com/10.1007/BF00614817. 5

[26] Robert W. Boyd. *Nonlinear Optics*. Academic Press, 2008. ISBN 0-08-048596-0. 5, 7, 8, 10

[27] Masayoshi Tonouchi. Cutting-edge terahertz technology. *Nature Photonics*, 1(2):97–105, February 2007. ISSN 1749-4885, 1749-4893. doi: 10.1038/nphoton.2007.3. URL http://www.nature.com/articles/nphoton.2007.3. 6

[28] John E. Midwinter and J Warner. The effects of phase matching method and of uniaxial crystal symmetry on the polar distribution of second-order non-linear optical polarization. *British Journal of Applied Physics*, 16(8):1135–1142, August 1965. ISSN 0508-3443. doi: 10.1088/0508-3443/16/8/312. URL https://iopscience.iop.org/article/10.1088/0508-3443/16/8/312. 10

[29] Dietrich Marcuse and American Telephone and Telegraph Company. *Theory of dielectric optical waveguides*. Academic Press, Boston, 1991. ISBN 978-0-323-16177-0. URL http://site.ebrary.com/id/10665454. OCLC: 637017693. 10

[30] Toshiaki Suhara and Masatoshi Fujimura. *Waveguide Nonlinear-Optic Devices*, volume 11 of *Springer Series in Photonics*. Springer Berlin Heidelberg, Berlin, Heidelberg, 2003. ISBN 978-3-642-05685-7 978-3-662-10872-7. doi: 10.1007/978-3-662-10872-7. URL http://link.springer.com/10.1007/978-3-662-10872-7. 10

[31] Leonard Mandel and Emil Wolf. *Optical Coherence and Quantum Optics*. Cambridge University Press, 1 edition, September 1995. ISBN 978-0-521-41711-2 978-1-139-64410-5. doi: 10.1017/CBO9781139644105. URL https://www.cambridge.org/core/product/identifier/9781139644105/type/book. 13

[32] Rodney Loudon. *The quantum theory of light*. Oxford science publications. Oxford University Press, Oxford ; New York, 3rd ed edition, 2000. ISBN 978-0-19-850177-0 978-0-19-850176-3. 13, 16, 18

[33] Nicolás Quesada and J. E. Sipe. Time-ordering effects in the generation of entangled photons using nonlinear optical processes. *Phys. Rev. Lett.*, 114:093903, Mar 2015. doi: 10.1103/PhysRevLett.114.093903. URL https://link.aps.org/doi/10.1103/PhysRevLett.114.093903. 13, 16, 37

[34] Andreas Christ, Benjamin Brecht, Wolfgang Mauerer, and Christine Silberhorn. Theory of quantum frequency conversion and type-II parametric down-conversion in the high-gain regime. *New Journal of Physics*, 15(5):053038, May 2013. ISSN 1367-2630. doi: 10.1088/1367-2630/15/5/053038. URL https://iopscience.iop.org/article/10.1088/1367-2630/15/5/053038. 13

[35] Georg Harder. *Optimized down-conversion source and state-characterization tools for quantum optics*. PhD thesis, Universität Paderborn, Fakultät für Naturwissenschaften, Warburger Str. 100, 33098 Paderborn, 2016. 14

[36] Vittorio Giovannetti, Seth Lloyd, and Lorenzo Maccone. Quantum-enhanced positioning and clock synchronization. *Nature*, 412(6845):417–419, July 2001. ISSN 0028-0836, 1476-4687. doi: 10.1038/35086525. URL http://www.nature.com/articles/35086525. 14

[37] N. Treps, U. Andersen, B. Buchler, P. K. Lam, A. Maître, H.-A. Bachor, and C. Fabre. Surpassing the Standard Quantum Limit for Optical Imaging Using Nonclassical Multimode Light. *Physical Review Letters*, 88(20):203601, May 2002. ISSN 0031-9007, 1079-7114. doi: 10.1103/PhysRevLett.88.203601. URL https://link.aps.org/doi/10.1103/PhysRevLett.88.203601. 14

[38] Saleh Rahimi-Keshari, Timothy C. Ralph, and Carlton M. Caves. Sufficient Conditions for Efficient Classical Simulation of Quantum Optics. *Physical Review X*, 6(2):021039, June 2016. ISSN 2160-3308. doi: 10.1103/PhysRevX.6.021039. URL https://link.aps.org/doi/10.1103/PhysRevX.6.021039.

[39] Tian Zhong, Hongchao Zhou, Robert D Horansky, Catherine Lee, Varun B Verma, Adriana E Lita, Alessandro Restelli, Joshua C Bienfang, Richard P Mirin, Thomas Gerrits, Sae Woo Nam, Francesco Marsili, Matthew D Shaw, Zheshen Zhang, Ligong Wang, Dirk Englund, Gregory W Wornell, Jeffrey H Shapiro, and Franco N C Wong. Photon-efficient quantum key distribution using timeenergy entanglement with high-dimensional encoding. *New Journal of Physics*, 17(2):022002, February 2015. ISSN 1367-2630. doi: 10.1088/1367-2630/17/2/022002. URL https://iopscience.iop.org/article/10.1088/1367-2630/17/2/022002. 14

[40] W. P. Grice and I. A. Walmsley. Spectral information and distinguishability in type-II down-conversion with a broadband pump. *Physical Review A*, 56(2):1627–1634, August 1997. ISSN 1050-2947, 1094-1622. doi: 10.1103/PhysRevA.56.1627. URL https://link.aps.org/doi/10.1103/PhysRevA.56.1627. 14, 26

[41] C. K. Law, I. A. Walmsley, and J. H. Eberly. Continuous Frequency Entanglement: Effective Finite Hilbert Space and Entropy Control. *Physical Review Letters*, 84(23):5304–5307, June 2000. ISSN 0031-9007, 1079-7114. doi: 10.1103/PhysRevLett.84.5304. URL https://link.aps.org/doi/10.1103/PhysRevLett.84.5304. 14

[42] Alfred B. URen, Christine Silberhorn, Konrad Banaszek, and Ian A. Walmsley. Efficient Conditional Preparation of High-Fidelity Single Photon States for Fiber-Optic Quantum Networks. *Physical Review Letters*, 93(9):093601, August 2004. ISSN 0031-9007, 1079-7114. doi: 10.1103/PhysRevLett.93.093601. URL https://link.aps.org/doi/10.1103/PhysRevLett.93.093601. 18

[43] J. Fan, A. Migdall, and L. J. Wang. Efficient generation of correlated photon pairs in a microstructure fiber. *Optics Letters*, 30(24):3368, December 2005. ISSN 0146-9592, 1539-4794. doi: 10.1364/OL.30.003368. URL https://www.osapublishing.org/abstract.cfm?URI=ol-30-24-3368. 18

[44] Philip Georgi, Marcello Massaro, Kai-Hong Luo, Basudeb Sain, Nicola Montaut, Harald Herrmann, Thomas Weiss, Guixin Li, Christine Silberhorn, and Thomas Zentgraf. Metasurface interferometry toward quantum sensors. *Light: Science & Applications*, 8(1):70, December 2019. ISSN 2047-7538. doi: 10.1038/s41377-019-0182-6. URL http://www.nature.com/articles/s41377-019-0182-6. 19, 21

[45] Marcello Massaro, Evan Meyer-Scott, Nicola Montaut, Harald Herrmann, and Christine Silberhorn. Improving SPDC single-photon sources via extended heralding and feed-forward control. *New Journal of Physics*, 21(5):053038, May 2019. ISSN 1367-2630. doi: 10.1088/1367-2630/ab1ec3. URL https://iopscience.iop.org/article/10.1088/1367-2630/ab1ec3. 19, 35

[46] Mohammadreza Khorasaninejad, Wei Ting Chen, Robert C. Devlin, Jaewon Oh, Alexander Y. Zhu, and Federico Capasso. Metalenses at visible wavelengths: Diffraction-limited focusing and subwavelength resolution imaging. *Science*, 352(6290):1190–1194, June 2016. ISSN 0036-8075, 1095-9203. doi: 10.1126/science.aaf6644. URL https://www.sciencemag.org/lookup/doi/10.1126/science.aaf6644. 21

[47] Shuming Wang, Pin Chieh Wu, Vin-Cent Su, Yi-Chieh Lai, Mu-Ku Chen, Hsin Yu Kuo, Bo Han Chen, Yu Han Chen, Tzu-Ting Huang, Jung-Hsi Wang, Ray-Ming Lin, Chieh-Hsiung Kuan, Tao Li, Zhenlin Wang, Shining Zhu, and Din Ping Tsai. A broadband achromatic metalens in the visible. *Nature Nanotechnology*, 13(3):227–232, March 2018. ISSN 1748-3387, 1748-3395. doi: 10.1038/s41565-017-0052-4. URL http://www.nature.com/articles/s41565-017-0052-4. 21

[48] Fuyong Yue, Dandan Wen, Jingtao Xin, Brian D. Gerardot, Jensen Li, and Xianzhong Chen. Vector Vortex Beam Generation with a Single Plasmonic Metasurface. *ACS Photonics*, 3(9):1558–1563, September 2016. ISSN 2330-4022, 2330-4022. doi: 10.1021/acsphotonics.6b00392. URL https://pubs.acs.org/doi/10.1021/acsphotonics.6b00392. 21

[49] Mikhail I. Shalaev, Jingbo Sun, Alexander Tsukernik, Apra Pandey, Kirill Nikolskiy, and Natalia M. Litchinitser. High-Efficiency All-Dielectric Metasurfaces for Ultracompact Beam Manipulation in Transmission Mode. *Nano Letters*, 15(9):6261–6266, September 2015. ISSN 1530-6984, 1530-6992. doi: 10.1021/acs.nanolett.5b02926. URL https://pubs.acs.org/doi/10.1021/acs.nanolett.5b02926. 21

[50] Lingling Huang, Xianzhong Chen, Holger Mühlenbernd, Hao Zhang, Shumei Chen, Benfeng Bai, Qiaofeng Tan, Guofan Jin, Kok-Wai Cheah, Cheng-Wei Qiu, Jensen Li, Thomas Zentgraf, and Shuang Zhang. Three-dimensional optical holography using a plasmonic metasurface. *Nature Communications*, 4(1):2808, December 2013. ISSN 2041-1723. doi: 10.1038/ncomms3808. URL http://www.nature.com/articles/ncomms3808. 21

[51] Guixin Li, Shumei Chen, Nitipat Pholchai, Bernhard Reineke, Polis Wing Han Wong, Edwina Yue Bun Pun, Kok Wai Cheah, Thomas Zentgraf, and Shuang Zhang. Continuous control of the nonlinearity phase for harmonic generations. *Nature Materials*, 14(6):607–612, June 2015. ISSN 1476-1122, 1476-4660. doi: 10.1038/nmat4267. URL http://www.nature.com/articles/nmat4267. 21

[52] Euclides Almeida, Ora Bitton, and Yehiam Prior. Nonlinear metamaterials for holography. *Nature Communications*, 7(1):12533, November 2016. ISSN 2041-1723. doi: 10.1038/ncomms12533. URL http://www.nature.com/articles/ncomms12533. 21

[53] Nanfang Yu and Federico Capasso. Flat optics with designer metasurfaces. *Nature Materials*, 13(2):139–150, February 2014. ISSN 1476-1122, 1476-4660. doi: 10.1038/nmat3839. URL http://www.nature.com/articles/nmat3839. 21

[54] Patrice Genevet, Federico Capasso, Francesco Aieta, Mohammadreza Khorasaninejad, and Robert Devlin. Recent advances in planar optics: from plasmonic to dielectric metasurfaces. *Optica*, 4(1):139, January 2017. ISSN 2334-2536. doi: 10.1364/OPTICA.4.000139. URL https://www.osapublishing.org/abstract.cfm?URI=optica-4-1-139.

[55] D. Lin, P. Fan, E. Hasman, and M. L. Brongersma. Dielectric gradient metasurface optical elements. *Science*, 345(6194):298–302, July 2014. ISSN 0036-8075, 1095-9203. doi: 10.1126/science.1253213. URL https://www.sciencemag.org/lookup/doi/10.1126/science.1253213. 21

[56] Pankaj K. Jha, Nir Shitrit, Jeongmin Kim, Xuexin Ren, Yuan Wang, and Xiang Zhang. Metasurface-Mediated Quantum Entanglement. *ACS Photonics*, 5(3):971–976, March 2018. ISSN 2330-4022, 2330-4022. doi: 10.1021/acsphotonics.7b01241. URL https://pubs.acs.org/doi/10.1021/acsphotonics.7b01241. 21

[57] Tomer Stav, Arkady Faerman, Elhanan Maguid, Dikla Oren, Vladimir Kleiner, Erez Hasman, and Mordechai Segev. Quantum entanglement of the spin and orbital angular momentum of photons using metamaterials. *Science*, 361(6407):1101–1104, September 2018. ISSN 0036-8075, 1095-9203. doi: 10.1126/science.aat9042. URL https://www.sciencemag.org/lookup/doi/10.1126/science.aat9042. 21

[58] Kai Wang, James G. Titchener, Sergey S. Kruk, Lei Xu, Hung-Pin Chung, Matthew Parry, Ivan I. Kravchenko, Yen-Hung Chen, Alexander S. Solntsev, Yuri S. Kivshar, Dragomir N. Neshev, and Andrey A. Sukhorukov. Quantum metasurface for multiphoton interference and state reconstruction. *Science*, 361(6407):1104–1108, September 2018. ISSN 0036-8075, 1095-9203. doi: 10.1126/science.aat8196. URL https://www.sciencemag.org/lookup/doi/10.1126/science.aat8196. 21

[59] Hong-Chao Liu, Biao Yang, Qinghua Guo, Jinhui Shi, Chunying Guan, Guoxing Zheng, Holger Mühlenbernd, Guixin Li, Thomas Zentgraf, and Shuang Zhang. Single-pixel computational ghost imaging with helicity-dependent metasurface hologram. *Science Advances*, 3(9):e1701477, September 2017. ISSN 2375-2548. doi: 10.1126/sciadv.1701477. URL https://advances.sciencemag.org/lookup/doi/10.1126/sciadv.1701477. 21

[60] Mehul Malik and Robert W. Boyd. Quantum Imaging Technologies. *La Rivista del Nuovo Cimento*, 37(5):273–332, June 2014. ISSN 0393-697X. doi: 10.1393/ncr/i2014-10100-0. URL http://arxiv.org/abs/1406.1685. arXiv: 1406.1685. 21

[61] C.L. Degen, F. Reinhard, and P. Cappellaro. Quantum sensing. *Reviews of Modern Physics*, 89(3):035002, July 2017. ISSN 0034-6861, 1539-0756. doi: 10.1103/RevModPhys.89.035002. URL http://link.aps.org/doi/10.1103/RevModPhys.89.035002. 21

[62] Mehul Malik, Manuel Erhard, Marcus Huber, Mario Krenn, Robert Fickler, and Anton Zeilinger. Multi-photon entanglement in high dimensions. *Nature Photonics*, 10(4): 248–252, April 2016. ISSN 1749-4885, 1749-4893. doi: 10.1038/nphoton.2016.12. URL http://www.nature.com/articles/nphoton.2016.12. 22

[63] Jonathan P. Dowling. Quantum optical metrology the lowdown on high-N00N states. *Contemporary Physics*, 49(2):125–143, March 2008. ISSN 0010-7514, 1366-5812. doi: 10.1080/00107510802091298. URL http://www.tandfonline.com/doi/abs/10.1080/00107510802091298. 23

[64] Zeev Bomzon, Gabriel Biener, Vladimir Kleiner, and Erez Hasman. Space-variant PancharatnamBerry phase optical elements with computer-generated subwavelength gratings. *Optics Letters*, 27(13):1141, July 2002. ISSN 0146-9592, 1539-4794. doi: 10.1364/OL.27.001141. URL https://www.osapublishing.org/abstract.cfm?URI=ol-27-13-1141. 24

[65] P. G. Kwiat, A. M. Steinberg, and R. Y. Chiao. High-visibility interference in a Bell-inequality experiment for energy and time. *Physical Review A*, 47(4):R2472–R2475, April 1993. ISSN 1050-2947, 1094-1622. doi: 10.1103/PhysRevA.47.R2472. URL https://link.aps.org/doi/10.1103/PhysRevA.47.R2472. 31

[66] Jacques Carolan, Christopher Harrold, Chris Sparrow, Enrique Martín-López, Nicholas J. Russell, Joshua W. Silverstone, Peter J. Shadbolt, Nobuyuki Matsuda, Manabu Oguma, Mikitaka Itoh, Graham D. Marshall, Mark G. Thompson, Jonathan C. F. Matthews, Toshikazu Hashimoto, Jeremy L. O'Brien, and Anthony Laing. Universal linear optics. *Science*, 349(6249):711–716, 2015. doi: 10.1126/science.aab3642. URL http://www.sciencemag.org/content/349/6249/711.abstract. 35

[67] Terry Rudolph. Why i am optimistic about the silicon-photonic route to quantum computing. *APL Photonics*, 2(3):030901, 2017/10/22 2017. doi: 10.1063/1.4976737. URL http://dx.doi.org/10.1063/1.4976737.

[68] Justin B. Spring, Benjamin J. Metcalf, Peter C. Humphreys, W. Steven Kolthammer, Xian-Min Jin, Marco Barbieri, Animesh Datta, Nicholas Thomas-Peter, Nathan K. Langford, Dmytro Kundys, James C. Gates, Brian J. Smith, Peter G. R. Smith, and Ian A. Walmsley. Boson sampling on a photonic chip. *Science*, 339(6121):798–801, 2013. ISSN 0036-8075. doi: 10.1126/science.1231692. URL http://science.sciencemag.org/content/339/6121/798.

[69] Max Tillmann, Borivoje Dakic, Rene Heilmann, Stefan Nolte, Alexander Szameit, and Philip Walther. Experimental boson sampling. *Nat Photon*, 7(7):540–544, 07 2013. URL http://dx.doi.org/10.1038/nphoton.2013.102.

[70] Andrea Crespi, Roberto Osellame, Roberta Ramponi, Daniel J. Brod, Ernesto F. Galvao, Nicolo Spagnolo, Chiara Vitelli, Enrico Maiorino, Paolo Mataloni, and Fabio Sciarrino. Integrated multimode interferometers with arbitrary designs for photonic boson

sampling. *Nat Photon*, 7(7):545–549, 07 2013. URL http://dx.doi.org/10.1038/nphoton.2013.112.

[71] Koji Azuma, Kiyoshi Tamaki, and Hoi-Kwong Lo. All-photonic quantum repeaters. *Nat Commun*, 6:6787, 2015. URL http://dx.doi.org/10.1038/ncomms7787.

[72] Thomas Herbst, Thomas Scheidl, Matthias Fink, Johannes Handsteiner, Bernhard Wittmann, Rupert Ursin, and Anton Zeilinger. Teleportation of entanglement over 143 km. *Proceedings of the National Academy of Sciences*, 112(46):14202–14205, 2015. doi: 10.1073/pnas.1517007112. URL http://www.pnas.org/content/112/46/14202.abstract. 35

[73] K. D. Irwin and G. C. Hilton. Transition-Edge Sensors. In *Cryogenic Particle Detection*, pages 63–150. Springer Berlin Heidelberg, 2005. ISBN 978-3-540-20113-7. doi: 10.1007/10933596_3. URL http://link.springer.com/chapter/10.1007/10933596_3. 35

[74] A. Avella, G. Brida, I. P. Degiovanni, M. Genovese, M. Gramegna, L. Lolli, E. Monticone, C. Portesi, M. Rajteri, M. L. Rastello, E. Taralli, P. Traina, and M. White. Self consistent, absolute calibration technique for photon number resolving detectors. *Optics Express*, 19(23):23249, November 2011. ISSN 1094-4087. doi: 10.1364/OE.19.023249. URL https://www.osapublishing.org/oe/abstract.cfm?uri=oe-19-23-23249. 35, 36

[75] M. J. Fitch, B. C. Jacobs, T. B. Pittman, and J. D. Franson. Photon-number resolution using time-multiplexed single-photon detectors. *Physical Review A*, 68(4):043814, October 2003. ISSN 1050-2947, 1094-1622. doi: 10.1103/PhysRevA.68.043814. URL https://link.aps.org/doi/10.1103/PhysRevA.68.043814. 35

[76] Regina Kruse, Johannes Tiedau, Tim J. Bartley, Sonja Barkhofen, and Christine Silberhorn. Limits of the time-multiplexed photon-counting method. *Physical Review A*, 95(2):023815, February 2017. ISSN 2469-9926, 2469-9934. doi: 10.1103/PhysRevA.95.023815. URL https://link.aps.org/doi/10.1103/PhysRevA.95.023815. 35

[77] Jian-Wei Pan, Dik Bouwmeester, Harald Weinfurter, and Anton Zeilinger. Experimental entanglement swapping: Entangling photons that never interacted. *Phys. Rev. Lett.*, 80:3891–3894, May 1998. doi: 10.1103/PhysRevLett.80.3891. URL https://link.aps.org/doi/10.1103/PhysRevLett.80.3891. 36

[78] Robert J. A. Francis-Jones, Rowan A. Hoggarth, and Peter J. Mosley. All-fiber multiplexed source of high-purity single photons. *Optica*, 3(11):1270, November 2016. ISSN 2334-2536. doi: 10.1364/OPTICA.3.001270. URL https://www.osapublishing.org/abstract.cfm?URI=optica-3-11-1270. 36, 65, 69

[79] Thomas Meany, Lutfi A. Ngah, Matthew J. Collins, Alex S. Clark, Robert J. Williams, Benjamin J. Eggleton, M. J. Steel, Michael J. Withford, Olivier Alibart, and Sébastien Tanzilli. Hybrid photonic circuit for multiplexed heralded single photons: Hybrid photonic circuit for multiplexed heralded single photons. *Laser & Photonics Reviews*,

8(3):L42–L46, May 2014. ISSN 18638880. doi: 10.1002/lpor.201400027. URL http://doi.wiley.com/10.1002/lpor.201400027. 36

[80] Fumihiro Kaneda, Bradley G. Christensen, Jia Jun Wong, Hee Su Park, Kevin T. McCusker, and Paul G. Kwiat. Time-multiplexed heralded single-photon source. *Optica*, 2(12):1010, December 2015. ISSN 2334-2536. doi: 10.1364/OPTICA.2.001010. URL http://arxiv.org/abs/1507.06052https://www.osapublishing.org/abstract.cfm?URI=optica-2-12-1010. 36, 69

[81] Chaitali Joshi, Alessandro Farsi, Stéphane Clemmen, Sven Ramelow, and Alexander L. Gaeta. Frequency multiplexing for quasi-deterministic heralded single-photon sources. *Nature Communications*, 9:847, December 2018. ISSN 2041-1723. URL http://www.nature.com/articles/s41467-018-03254-4. 36

[82] M. Grimau Puigibert, G.H. Aguilar, Q. Zhou, F. Marsili, M.D. Shaw, V.B. Verma, S.W. Nam, D. Oblak, and W. Tittel. Heralded Single Photons Based on Spectral Multiplexing and Feed-Forward Control. *Physical Review Letters*, 119:083601, August 2017. ISSN 0031-9007, 1079-7114. URL https://link.aps.org/doi/10.1103/PhysRevLett.119.083601. 36, 69

[83] Lutfi Arif Ngah, Olivier Alibart, Laurent Labonté, Virginia D'Auria, and Sébastien Tanzilli. Ultra-fast heralded single photon source based on telecom technology. *Laser & Photonics Reviews*, 9(2):L1–L5, March 2015. ISSN 18638880. doi: 10.1002/lpor.201400404. URL http://doi.wiley.com/10.1002/lpor.201400404. 36

[84] Peter P. Rohde. Improving the fidelity of single photon preparation from conditional down-conversion via asymmetric multiport detection. *eprint arXiv:quant-ph/0703238*, March 2007. 36

[85] Andreas Christ and Christine Silberhorn. Limits on the deterministic creation of pure single-photon states using parametric down-conversion. *Phys. Rev. A*, 85:023829, Feb 2012. doi: 10.1103/PhysRevA.85.023829. URL http://link.aps.org/doi/10.1103/PhysRevA.85.023829. 36, 37

[86] G. Brida, I. P. Degiovanni, M. Genovese, A. Migdall, F. Piacentini, S. V. Polyakov, and I. Ruo Berchera. Experimental realization of a low-noise heralded single-photon source. *Opt. Express*, 19(2):1484–1492, Jan 2011. doi: 10.1364/OE.19.001484. URL http://www.opticsexpress.org/abstract.cfm?URI=oe-19-2-1484. 36, 47

[87] G. Brida, I. P. Degiovanni, M. Genovese, F. Piacentini, P. Traina, A. Della Frera, A. Tosi, A. Bahgat Shehata, C. Scarcella, A. Gulinatti, M. Ghioni, S. V. Polyakov, A. Migdall, and A. Giudice. An extremely low-noise heralded single-photon source: A breakthrough for quantum technologies. *Applied Physics Letters*, 101(22):221112–4, 11 2012. URL http://dx.doi.org/10.1063/1.4768288.

[88] Robert J A Francis-Jones and Peter J Mosley. Fibre-integrated noise gating of high-purity heralded single photons. *Journal of Optics*, 19(10):104005, 2017. URL http://stacks.iop.org/2040-8986/19/i=10/a=104005. 36

[89] Evan Meyer-Scott, Nicola Montaut, Johannes Tiedau, Linda Sansoni, Harald Herrmann, Tim J. Bartley, and Christine Silberhorn. Limits on the heralding efficiencies and spectral purities of spectrally filtered single photons from photon-pair sources. *Phys. Rev. A*, 95:061803(R), Jun 2017. doi: 10.1103/PhysRevA.95.061803. URL https://link.aps.org/doi/10.1103/PhysRevA.95.061803. 37

[90] Andreas Christ, Cosmo Lupo, Matthias Reichelt, Torsten Meier, and Christine Silberhorn. Theory of filtered type-II parametric down-conversion in the continuous-variable domain: Quantifying the impacts of filtering. *Phys. Rev. A*, 90:023823, Aug 2014. doi: 10.1103/PhysRevA.90.023823. URL http://link.aps.org/doi/10.1103/PhysRevA.90.023823. 37

[91] Agata M Brańczyk, T C Ralph, Wolfram Helwig, and Christine Silberhorn. Optimized generation of heralded Fock states using parametric down-conversion. *New Journal of Physics*, 12(6):063001, 2010. URL http://stacks.iop.org/1367-2630/12/i=6/a=063001. 37

[92] Andreas Christ, Kaisa Laiho, Andreas Eckstein, Katiúscia N Cassemiro, and Christine Silberhorn. Probing multimode squeezing with correlation functions. *New Journal of Physics*, 13(3):033027, 2011. URL http://stacks.iop.org/1367-2630/13/i=3/a=033027. 41, 42, 43

[93] J. R. Johansson, P. D. Nation, and Franco Nori. Qutip: An open-source python framework for the dynamics of open quantum systems. *Computer Physics Communications*, 183(8):1760–1772, 2012. doi: https://doi.org/10.1016/j.cpc.2012.02.021. URL http://www.sciencedirect.com/science/article/pii/S0010465512000835. 45

[94] Damien Bonneau, Gabriel J Mendoza, Jeremy L OBrien, and Mark G Thompson. Effect of loss on multiplexed single-photon sources. *New Journal of Physics*, 17(4):043057, April 2015. ISSN 1367-2630. doi: 10.1088/1367-2630/17/4/043057. URL http://stacks.iop.org/1367-2630/17/i=4/a=043057?key=crossref.b2029b4184296d780afa9b88be1a24d3. 58

[95] Gabriel J. Mendoza, Raffaele Santagati, Jack Munns, Elizabeth Hemsley, Mateusz Piekarek, Enrique Martín-López, Graham D. Marshall, Damien Bonneau, Mark G. Thompson, and Jeremy L. OBrien. Active temporal and spatial multiplexing of photons. *Optica*, 3(2):127, February 2016. ISSN 2334-2536. doi: 10.1364/OPTICA.3.000127. URL https://www.osapublishing.org/abstract.cfm?URI=optica-3-2-127. 65, 69

[96] Peter P. Rohde, L. G. Helt, M. J. Steel, and Alexei Gilchrist. Multiplexed single-photon-state preparation using a fiber-loop architecture. *Physical Review A*, 92(5):053829, November 2015. ISSN 1050-2947, 1094-1622. doi: 10.1103/PhysRevA.92.053829. URL https://link.aps.org/doi/10.1103/PhysRevA.92.053829. 66

[97] Amnon Yariv, Pochi Yeh, and Amnon Yariv. *Photonics: optical electronics in modern communications*. The Oxford series in electrical and computer engineering. Oxford

University Press, New York, 6th ed edition, 2007. ISBN 978-0-19-517946-0. OCLC: ocm58648003. 72, 74

[98] Syoji Yamada and Makoto Minakata. DC Drift Phenomena in $LiNbO_3$ Optical Waveguide Devices. *Japanese Journal of Applied Physics*, 20(4):733–737, April 1981. ISSN 0021-4922, 1347-4065. doi: 10.1143/JJAP.20.733. URL https://iopscience.iop.org/article/10.1143/JJAP.20.733. 76

[99] John W. Evans. Solc Birefringent Filter. *Journal of the Optical Society of America*, 48 (3):142, March 1958. ISSN 0030-3941. doi: 10.1364/JOSA.48.000142. URL https://www.osapublishing.org/abstract.cfm?URI=josa-48-3-142. 78

[100] Kai-Hong Luo, Sebastian Brauner, Christof Eigner, Polina R. Sharapova, Raimund Ricken, Torsten Meier, Harald Herrmann, and Christine Silberhorn. Nonlinear integrated quantum electro-optic circuits. *Science Advances*, 5(1):eaat1451, January 2019. ISSN 2375-2548. doi: 10.1126/sciadv.aat1451. URL http://advances.sciencemag.org/lookup/doi/10.1126/sciadv.aat1451. 81, 86

[101] Malte Avenhaus, Andreas Eckstein, Peter J. Mosley, and Christine Silberhorn. Fiber-assisted single-photon spectrograph. *Optics Letters*, 34(18):2873, September 2009. ISSN 0146-9592, 1539-4794. doi: 10.1364/OL.34.002873. URL https://www.osapublishing.org/abstract.cfm?URI=ol-34-18-2873. 85

[102] C. K. Hong, Z. Y. Ou, and L. Mandel. Measurement of subpicosecond time intervals between two photons by interference. *Physical Review Letters*, 59(18):2044–2046, November 1987. ISSN 0031-9007. doi: 10.1103/PhysRevLett.59.2044. 85

[103] Katiúscia N Cassemiro, Kaisa Laiho, and Christine Silberhorn. Accessing the purity of a single photon by the width of the HongOuMandel interference. *New Journal of Physics*, 12(11):113052, November 2010. ISSN 1367-2630. doi: 10.1088/1367-2630/12/11/113052. URL https://iopscience.iop.org/article/10.1088/1367-2630/12/11/113052. 85

[104] C. Y. Huang, C. H. Lin, Y. H. Chen, and Y. C. Huang. Electro-optic Ti:PPLN waveguide as efficient optical wavelength filter and polarization mode converter. *Optics Express*, 15(5):2548, 2007. ISSN 1094-4087. doi: 10.1364/OE.15.002548. URL https://www.osapublishing.org/oe/abstract.cfm?uri=oe-15-5-2548. 86

[105] Dieter H. Jundt. Temperature-dependent Sellmeier equation for the index of refraction, n_e, in congruent lithium niobate. *Optics Letters*, 22(20):1553, October 1997. ISSN 0146-9592, 1539-4794. doi: 10.1364/OL.22.001553. URL https://www.osapublishing.org/abstract.cfm?URI=ol-22-20-1553. 87

[106] G. J. Edwards and M. Lawrence. A temperature-dependent dispersion equation for congruently grown lithium niobate. *Optical and Quantum Electronics*, 16(4):373–375, July 1984. ISSN 0306-8919, 1572-817X. doi: 10.1007/BF00620081. URL http://link.springer.com/10.1007/BF00620081. 87

[107] Boris Korzh, Qing-Yuan Zhao, Jason P. Allmaras, Simone Frasca, Travis M. Autry, Eric A. Bersin, Andrew D. Beyer, Ryan M. Briggs, Bruce Bumble, Marco Colangelo, Garrison M. Crouch, Andrew E. Dane, Thomas Gerrits, Adriana E. Lita, Francesco Marsili, Galan Moody, Cristián Peña, Edward Ramirez, Jake D. Rezac, Neil Sinclair, Martin J. Stevens, Angel E. Velasco, Varun B. Verma, Emma E. Wollman, Si Xie, Di Zhu, Paul D. Hale, Maria Spiropulu, Kevin L. Silverman, Richard P. Mirin, Sae Woo Nam, Alexander G. Kozorezov, Matthew D. Shaw, and Karl K. Berggren. Demonstration of sub-3 ps temporal resolution with a superconducting nanowire single-photon detector. *Nature Photonics*, 14(4):250–255, April 2020. ISSN 1749-4885, 1749-4893. doi: 10.1038/s41566-020-0589-x. URL http://www.nature.com/articles/s41566-020-0589-x. 87

[108] Andreas Eckstein, Benjamin Brecht, and Christine Silberhorn. A quantum pulse gate based on spectrally engineered sum frequency generation. *Optics Express*, 19 (15):13770, July 2011. ISSN 1094-4087. doi: 10.1364/OE.19.013770. URL https://www.osapublishing.org/oe/abstract.cfm?uri=oe-19-15-13770. 87